PFC/RR-88-6

DOE/ET-51013-250
UC20, a, b, d, f, g

Hot Electron Plasma Equilibrium and Stability in the Constance B Mirror Experiment

Xing Chen

April, 1988

Plasma Fusion Center

Massachusetts Institute of Technology

Cambridge, MA 02139 USA

Supported by United States Department of Energy Contract DE-AC02-78ET51013.

Hot Electron Plasma Equilibrium and Stability in the Constance B Mirror Experiment

by

Xing Chen

B.S. Wuhan University, 1981

Submitted to the Department of Physics
in partial fulfillment of the requirements for
the Degree of

Doctor of Philosophy

at the
Massachusetts Institute of Technology
April 21, 1988

Signature of Author _____

Department of Physics
April 21, 1988

Certified by _____

Richard S. Post
Thesis Supervisor

Accepted by _____

George F. Koster
Chairman, Ph.D. Committee

Hot Electron Plasma Equilibrium and Stability in the Constance B Mirror Experiment

by

Xing Chen

Submitted to the Department of Physics on April 21, 1987
in partial fulfillment of the requirements for the degree of
Doctor of Philosophy

Abstract

An experimental study of the equilibrium and macroscopic stability property of an electron cyclotron resonance heating (ECRH) generated plasma in a minimum-B mirror is presented. The Constance B mirror is a single cell quadrupole magnetic mirror in which high beta ($\beta \leq 0.3$) hot electron plasmas ($T_e \simeq 400$ keV) are created with up to 4 kW of ECRH power. The plasma equilibrium profile is hollow and resembles the baseball seam geometry of the magnet which provides the confining magnetic field. This configuration coincides with the drift orbit of deeply trapped particles. The on-axis hollowness of the hot electron density profile is $50 \pm 10\%$, and the pressure profile is at least as hollow as, if not more than, the hot electron density profile.

The hollow plasma equilibrium is macroscopically stable and generated in all the experimental conditions in which the machine has been operated. The hollowness of the plasma pressure profile is not limited by the marginal stability condition. Small macroscopic plasma fluctuations in the range of the hot electron curvature drift frequency sometimes occur but their growth rate is small ($\omega_i/\omega_r \leq 10^{-2}$) and saturate at very low level ($\delta B/\bar{B} \leq 10^{-3}$). Particle drift reversal is predicted to occur for the model pressure profile which best fits the experimental data under the typical operating conditions. No strong instability is observed when the plasma is near the drift reversal parameter regime, despite a theoretical prediction of instability under such conditions. The experiment shows that the cold electron population has no stabilizing effect to the hot electrons, which disagrees with current hot electron stability theories and results of previous maximum-B experiments. A theoretical analysis using MHD theory shows that the compressibility can stabilize a plasma with a hollowness of 20 – 30 percent in the Constance B mirror well. Although the Constance plasma is not typically in a regime in which MHD theory is valid, the stabilizing effect of compressibility suggests that the geometric effects which relate to the field line curvature play a significant role. The observed plasma stability cannot be fully explained by the theories based on the effects such as line-tying, finite electron or ion Larmor radius, and compressibility.

Thesis Supervisor: Dr. Richard S. Post

Acknowledgements

I would to thank my thesis supervisor, Dr. Richard S. Post, for overseeing the work performed for this thesis. He first brought up the topic of this dissertation to me when I arrived at M.I.T. five years ago. His invaluable guidance and support have extended throughout the course of the work. Thanks also to Dr.'s Barton Lane and Donna Smatlak, my immediate research advisors, for their constant guidance and overseeing every step of this study. Donna is the leader of the Constance group and is responsible for its excellent operation. Her intuition and knowledge of experimental physics is greatly appreciated. Barton is an excellent theoretical plasma physicist whom I have fortunately met. His deep understanding of plasma physics has greatly improved this thesis.

I am also grateful to the other present and former graduate students in the Constance group: Rich Garner, Gerald Gibson, Dan Goodman, Sam Hokin, Craig Petty, Ling Wang, and Tom Farish, for their support and assistance in conducting this research. They are good colleagues and good friends and have made my graduate study enjoyable. I would also like to thank the technician, Ken Retman, for keeping the machine running smoothly.

I would like to thank the scientists in the Tara research group, especially Dr.'s Jay Kesner, Mike Gerver, Bill Guss, Jim Irby, Evelio Sevillano and Don Smith, for their support. Thanks also to S. Hiroe of Oak Ridge National Laboratory for his interest in this work and his suggestion for looking for compressibility effects.

I would like to thank Ruijue Peng for her interest and support for this study.

Finally, I would like to express my appreciation to Professors Ron Davidson and Miklos Porkolab for serving in the thesis committee.

Contents

List of Figures

Table of Symbols

The formula in this dissertation are given in SI unit. Unless otherwise specified, the following symbols are defined as:

(1)	$\vec{B}$	=	Equilibrium magnetic field
(2)	$\tilde{B}$	=	Equilibrium diamagnetic field
(3)	B	=	$\mid \vec{B} \mid$
(4)	B_0	=	Vacuum magnetic field strength at the mirror well
(5)	$\vec{b}$	=	$\vec{B}/B$
(6)	$\vec{\kappa}$	=	Field line curvature ($\equiv (\vec{b} \cdot \nabla)\vec{b}$)
(7)	$P_{\perp,\parallel}$	=	Perpendicular and parallel plasma pressure
(8)	$\vec{J}$	=	Plasma current density
(9)	$m_{i,e}$	=	Ion and electron masses
(10)	$T_{i,e}$	=	Ion and electron temperatures
(11)	$n_{i,e}$	=	Ion and electron densities
(12)	n_0	=	Neutral background gas density
(13)	ϵ	=	Particle energy
(14)	μ	=	Particle magnetic moment
(15)	$\omega_{ci,e}$	=	Ion and electron cyclotron frequencies ($\equiv eB/m_{i,e}$)
(16)	$\omega_{pi,e}$	=	Ion and electron plasma frequencies ($\equiv (n_{i,e}e^2/\epsilon_0 m_{i,e})^{1/2}$)
(17)	$\vec{v_d}$	=	Particle guiding center drift velocity
(18)	β_{peak}	=	$2\mu_0(P_\parallel + P_\perp)_{peak}/B_0^2$
(19)	σ	=	$1 + \mu_0(P_\perp - P_\parallel)/B^2$
(20)	τ	=	$1 + \frac{\mu_0}{B}\frac{\partial P_\perp}{\partial B}$
(21)	R	=	Magnetic mirror ratio ($\equiv B_{max}/B_0$)
(22)	R_c	=	Radius of field line curvature ($\equiv \mid \vec{\kappa} \mid^{-1}$)
(23)	R_p	=	$\mid \frac{d\ lnP}{dr} \mid^{-1}$
(24)	$\nabla_\perp$	=	$\nabla - \vec{b}(\vec{b} \cdot \nabla)$
(25)	ω	=	Instability mode frequency ($\equiv i\omega_i + \omega_r$)

Chapter 1

Introduction

This thesis presents an experimental study of the hot electron plasma equilibrium and macroscopic stability in the Constance B mirror experiment. The focus of the investigation is to (1) quantitatively determine the three dimensional plasma equilibrium in a minimum-B mirror configuration, something which has not been thoroughly determined in any of the previous minimum-B experiments; and (2) characterize the stability properties of the non-ideal magnetohydrodynamic (MHD) hot electron plasma and make detailed comparisons between the experiment and current MHD and hot electron stability theories.

The Constance B mirror is a single cell quadrupole minimum-B magnetic mirror in which the plasma is generated and heated by microwaves at the fundamental electron cyclotron resonance frequency [Post, 1984; Smatlak, 1986]. In the typical operating conditions the hot electron temperature is on the order of 400 keV, resulting in an electron curvature drift frequency which is higher than both the ion cyclotron frequency and the characteristic MHD growth rate. Several entirely unexpected results are found in this study. The plasma in the Constance B mirror is hollow and concentrated along a baseball seam curve similar to the shape of the confining magnet. This is the first time such an equilibrium configuration has been experimentally observed. The on-axis hollowness of the plasma pressure profile is more than 50 percent, which

is theoretically MHD unstable even with the compressibility being taken into account. Such a disagreement between the predictions of MHD theory and the experimental observations is not that surprising in view of the non-MHD parameter range in which Constance usually operates. However, the hollow baseball seam plasma equilibrium is macroscopically stable in a wide parameter regime. It is observed in all the experimental conditions the experiment has been operated, including regimes in which MHD theory is applicable. The experimental data shows that stability of the hot electron plasma is independent of the cold electron fraction, which disagrees with results of the ELMO [Dandl, 1964] and EBT [Dandl, 1971; Hiroe, 1983] experiments as well as current hot electron stability theories. Analysis of the model equilibrium which most closely matches the experimental observations shows that the magnetic field gradient is reversed under typical machine operating conditions. No particularly strong instability is observed when the plasma pressure reaches the gradient reversal parameter regime.

The current understanding of the plasma equilibrium has been developed largely based on the magnetohydrodynamic theories. According to the guiding-center-fluid model, the hydromagnetic equilibrium of a magnetically confined plasma is determined by

$$\vec{J} \times \vec{B} = \nabla \cdot \mathbf{P} \tag{1.1}$$

$$\nabla \times \vec{B} = \mu_0 \vec{J} \tag{1.2}$$

$$\nabla \cdot \vec{B} = 0. \tag{1.3}$$

Here $\vec{B}$ is the magnetic field, $\vec{J}$ the plasma electric current, and $\mathbf{P} = P_\perp \mathbf{I} + (P_\parallel - P_\perp)\vec{b}\vec{b}$ is the anisotropic pressure tensor. The solution to the equations can be obtained when the plasma pressure and appropriate boundary conditions are given. The major focus of theoretical equilibrium studies has been on determining the self-consistent relations between the magnetic field and given plasma pressure profiles in various magnetic

geometries using these equations.

There are other conditions which determine a plasma equilibrium in addition to the above equations. Ideally one might wish to derive from first principles the plasma pressure which enters into the equilibrium force balance equation. In practice this requires a model incorporating particle sources, sinks and velocity space and real space flows due to RF and collisional processes. Theoretical modelling of these processes is extremely difficult and has been limited mainly to the one-dimensional geometry. Even in this case the results are still not always reliable. Therefore an experimental determination of the three dimensional plasma pressure profiles illuminates the underlying fundamental physical processes of source function, transport and loss mechanisms.

A plasma equilibrium also has to satisfy various stability criteria. Unlike microinstabilities which are related to the details of particle distribution functions, macroscopic instabilities occur when unfavorable spatial gradients become too large. These macroinstabilities can either destroy the plasma or change its spatial profile, thus effectively limiting the equilibrium. One example of such instabilities is the interchange instability which occurs when the plasma pressure gradient is in the same direction as the gradient of the magnetic field [Rosenbluth and Longmire, 1957]. When a plasma becomes unstable the instability can destroy the equilibrium on an MHD time scale, which is typically on the order of a microsecond.

The MHD stability theory is valid only in a limited parameter regime where the frequency of instabilities is small compared with the ion cyclotron frequency, and the particle Larmor radius is small compared with the scale length of the plasma. However, in a plasma with a hot electron population, the MHD assumptions break down when the hot electron drift frequency is similar to or larger than the ion cyclotron frequency or the characteristic MHD growth rate. In this situation the hot electrons

are no longer been fixed on a field line on the time scale of the instability and therefore have to be treated kinetically. Plasmas containing such a hot electron component will be referred to as hot electron plasmas in contrast to the usual MHD plasmas.

Many experiments have been conducted to study the plasma equilibrium properties and to test the MHD theories. Early experiments were concentrated on trapping plasmas in axisymmetric mirror geometries [Post, 1960; Ioffe, 1960; Bodin, 1961; Rostoker, 1961; Coensgen, 1962; Little, 1962; Perkins and Post, 1963]. It was soon realized that instabilities play a serious role in degrading plasma confinement. In a simple mirror the magnetic field is peaked on the axis. The confined plasma is therefore always unstable to MHD interchange modes. The observations confirmed that the interchange instability did occur in these devices and it was the limiting factor to the plasma confinement. However, the experiments also showed that in most cases the growth rate of the instabilities was one to two orders of magnitude lower than the predicted MHD growth rate, and the stability could be improved by using streaming warm plasmas or by increasing the background gas density to raise the cold plasma density. The observed stabilization of the interchange instability was explained in term of two mechanisms. The first was the line-tying mechanism in which charge separation due to the instability was suppressed by cold plasma outside the confinement region and by conducting end plates [Post, 1960; Lehnert, 1966; Kunkel and Guillory, 1965; Scott, 1965]. The other was the finite Larmor radius effect (FLR) in which the phase coherence between the ions and the electrons in an interchange motion is destroyed by the finite gyro-orbits of the hot particles, thereby reducing the subsequent plasma distortion [Rosenbluth, 1962].

An important development in improving plasma stability properties was the introduction of the minimum-B magnetic configuration. By superimposing higher order multipole fields on a simple mirror, Ioffe *et al.* transformed an MHD unstable mir-

ror geometry to an intrinsically stable configuration [Gott, 1961]. The experiment successfully demonstrated the improvement of plasma confinement by orders of magnitude, and it showed that an MHD stable plasma can be obtained when the $\int dl/B$ interchange stability criterion is satisfied.

Plasma equilibrium and stability has also been studied in the parameter region where the MHD assumptions do not apply. ELMO and EBT experiments were experimental tests where MHD theory failed. The plasma equilibrium in ELMO was characterized by a high beta hot electron annulus. The experiment stimulated interest in the physics of hot electron plasmas because of the prospect that hot electrons might be used to modify the otherwise unstable magnetic configurations. Experimentally the stability of this hot electron ring against interchange instabilities requires enough background gas to provide sufficient cold plasma density. Kinetic treatment of the cold electron stabilization to hot electron curvature driven modes showed that the stabilization occurs because the cold and hot electrons respond differently to a given perturbation. When the two populations are comparable, the perturbed field will be dissipated by one or the other, resulting in a stable plasma. The EBT experiment in which a toroidal plasma was generated in each of the 24 mirror cells again confirmed this cold electron stabilization effect.

Despite these successes, many physics issues are still unclear. Some of the mostly encountered questions are:

- Can magnetic gradient reversal be achieved ?
- Is the $\int dl/B$ MHD interchange stability condition sufficient for macroscopic stability ?
- Is the cold electron stabilization the only important effect for the hot electron interchange mode ?

Answering these questions requires more detailed theoretical modelling and experiments than has been previously done. Theoretical equilibrium and stability analysis has been limited mostly in simplified geometries and in the low beta limit, which in many cases are not satisfied in the experiments. On the other hand, quantitative comparison between the theories and experiments has also been limited by the accuracy of the experimental equilibrium determination. For instance, the three dimensional plasma equilibrium of minimum-B mirrors has not been thoroughly determined in any device even though several experiments have been conducted [Gott, 1961; Biguest, 1964; Damm, 1964; Francis, 1965; Barr and Perkins, 1965; Colchin, 1970; Haste and Lazar, 1973; Turner, 1979]. Further experiments are needed also because the theories have been tested only in a limited parameter regime. Cold electron stabilization of the hot electron curvature driven modes has been confirmed in maximum-B devices. But it is not clear whether it is still important in other magnetic configurations, or whether there are other stabilization mechanisms which have not shown up in a maximum-B geometry. Another important issue concerns the possibility of achieving curvature drift reversal. Magnetic gradient reversal was reported to be achieved in the SM-1 experiment [Quan, 1986; Hedrick, 1987]. But according to the theoretical analysis of Berk and Zhang (1987) the gradient reversal will be limited by instabilities which occur before the onset of the reversal. Either the measurement is not accurate or the theory does not apply, or there exist some other mechanisms which limit the instability from growing. The goal of this thesis is to try to answer some of these questions by making detailed comparisons between a hot electron plasma experiment and the MHD and hot electron stability theories.

The organization of this thesis is as follows. Chapter 2 describes the hardware of the experiment, which includes the basic experiment setup (Section 2.1) and the diagnostics used in this study (Section 2.2). Chapter 3 presents the general properties

of the Constance B mirror plasma. The first section describes the determination of the basic plasma parameters such as the plasma densities, electron and and ion temperatures, and summarizes the results of two previous dissertations concerning the hot electron velocity space diffusion and the microinstabilities in Constance. The remaining sections are then devoted to presenting experimental evidence and theoretical analysis to show the baseball seam characteristic of the Constance B plasma equilibrium. The equilibrium is determined by several competing processes: the plasma heating and source function which occur off-axis, and the curvature driven instabilities which are expected to drive the plasma towards the axis. Theoretical analysis of the single particle motion and fluid equilibrium equations shows that the baseball seam equilibrium represents a radially hollow plasma profile in the quadrupole mirror configuration. Based on these observations a plasma pressure model is developed.

Chapter 4 presents a quantitative determination of the plasma equilibrium using the experimental data from four complementary measurements, x-ray imaging, visible light imaging, magnetic measurements, and the skimmer probe and thermocouple probe measurement. The equilibrium determination is based on comparison between the experimental observations and the predictions of the pressure model. A key parameter to be determined is the hollowness of the plasma radial profile, which is crucial for the stability analysis. The results show that the hollowness of the hot electron density profile is 50 ± 10 percent, and the plasma pressure profile is at least as hollow as, if not more hollow than, the hot electron density profile.

Chapter 5 and 6 present the experimental observation and analysis of the plasma stability properties. Overall, the hollow baseball seam plasma equilibrium is macroscopically stable, as demonstrated by the fact that the equilibrium exists on a time scale 5 – 6 orders of magnitude longer than the characteristic MHD growth time. However, there remain questions such as whether the hollowness of the plasma pres-

sure profile is determined by the marginal stability condition, or it is just because of the given plasma heating profile and transport. If the profile is marginally stable, the plasma will respond to microinstabilities with enhanced fluctuations when the equilibrium is changed by the axial loss of hot electrons. We conclude that the plasma profile is not limited by the stability conditions because the enhanced fluctuations do not exist and a more hollow pressure profile can be produced when a skimmer probe is inserted along the axis. The measurement identified a macroscopic azimuthally propagating mode with coherent oscillation frequencies from 10 to 27 MHz which propagates along the particle drift surfaces. The frequency of the mode increases with vacuum magnetic field but decreases as a function of time as the instability develops. The growth rate of this mode is small ($\omega_i/\omega_r \leq 10^{-2}$) and it saturates at a very low level ($\delta B/\bar{B} \simeq 10^{-3}$). After presenting these observations in chapter 5, the next chapter analyzes the measured plasma stability properties and compares the observation with the current stability theories. The hollow equilibrium profile is generated under all machine operating conditions, independent of the plasma beta, ECRH power, background pressure, and the vacuum magnetic field strength. Comparison between the experiment and the hot electron stability theories shows that none of the existing theories can explain the observed plasma stability over such a wide parameter regime. The largest stabilizing effect found so far is the effect of compressibility in MHD which can stabilize a plasma with 20 – 30 percent hollowness in the Constance B mirror well. Although MHD theory is not applicable in the typical Constance parameter range, this suggests that the geometric effects which relate to the radius of field line curvature play a significant role. In chapter 7, the results of the study are summarized and their implications are discussed.

Chapter 2

The Constance B Experiment

This chapter describes the experimental setup of the Constance B mirror experiment. The Constance B mirror experiment began operation in October, 1983. It is a continuation of the Constance I and Constance II magnetic mirror programs at MIT. The primary objective of the experiment is to study the basic physics issues of the ECRH plasma in a minimum-B magnetic configuration. The experimental group currently includes one full time research scientist and four graduate students. Several research scientists in the Tara research group also provide support to the Constance program. The main areas of research which have been investigated are: hot electron plasma equilibrium, hot electron microinstability, ECRH-induced electron velocity-space diffusion, ion cyclotron resonance heating (ICRH), electron and ion radial transport, and high charge state impurity confinement. The selection of these topics is driven by the role of Constance as a support machine for the tandem mirror fusion program, as well as understanding the basic physics issues of hot electron plasmas.

2.1 Basic Systems

2.1.1 Magnetic Field

The Constance B magnetic field is generated by a water cooled copper conductor magnet shaped like the seam of a baseball. The magnet current is supplied by a

current rectifier from the 13.8 kV power line and it consumes about 1.5 MW of electric power.

Figure 2.1(a) shows some field lines and mod-B contours at the horizontal symmetry plane. The field possesses quadrupole symmetry and the magnetic flux surfaces are fanned as indicated in Fig. 2.1(b). The magnetic mirror ratio is 1.89 on the axis and varies from field line to field line. The distance between the two mirror peaks is 80 cm. The mod-B surfaces near the center of the machine are egg-shaped with a ratio between the major and minor radii of about 1.6:1 (major radius on the z axis). The experiment is normally operated at magnetic fields between 2.6 and 3.7 kG in the center of the mirror well.

The magnetic field geometry is of critical importance to the equilibrium study. An analytical expression for the vacuum field has been derived based on the field contours produced by the EFFI code [Sackett, 1978] for use in the equilibrium calculation. The expression contains the dipole and quadrupole field components and includes terms up to r^4. It is accurate to within 5 percent in the entire magnetic well (mirror ratio 1.8:1). The details of the expression and its derivation are given in Appendix A.

2.1.2 ECRH Heating System

Fundamental electron cyclotron resonance heating is used to break down the gas and heat the plasma. The ECRH microwave power is produced by a Gunn diode and amplified by a CW klystron (Varian model VA-911). The system delivers up to 4 kW of microwave power at 10.5 GHz with a bandwidth of 1 MHz. The RF wave is launched by a 17 dB horn perpendicular to the magnetic axis at approximately 40 cm above the axis and 10 cm off the midplane. The ECRH power is measured by a thermistor connected at the output of the klystron with a 40 dB directional coupler. The vacuum chamber forms a microwave cavity and strong cavity mode effects have been observed. The single pass absorption of the microwave power is

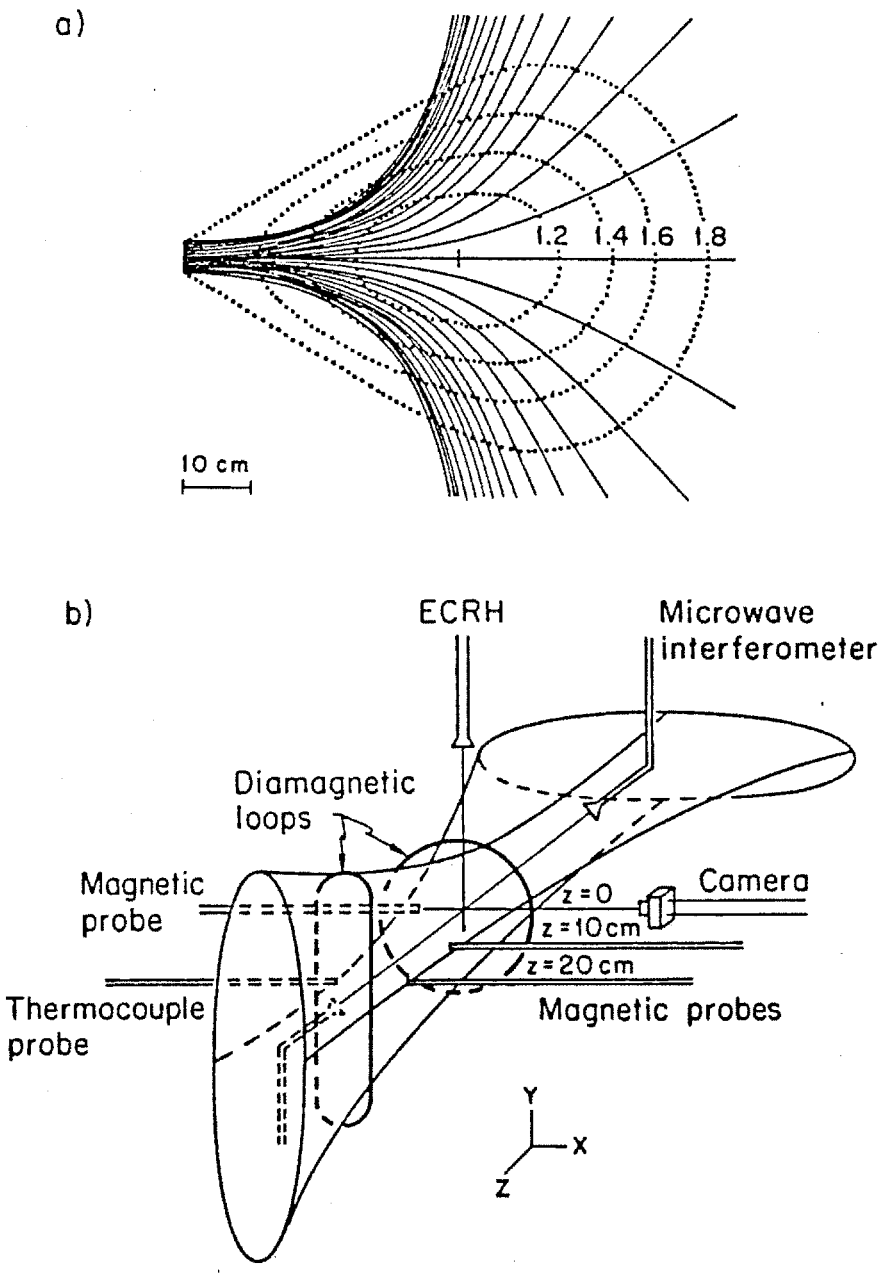

Figure 2.1: (a) The Constance B magnetic field geometry. The solid lines are field lines and the dotted lines are surfaces of constant magnetic field. The values on the magnetic field contours are the mirror ratios with respect to the field at the center of the magnetic well. (b) Experimental setup for the equilibrium study. The magnetic flux surface are shown in the background. The origin of the (x, y, z) coordinate system is at the center of the midplane.

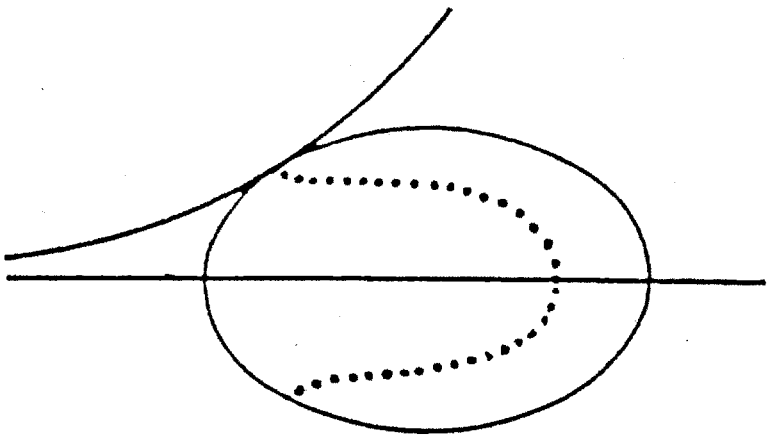

Figure 2.2: Strong ECRH heating is expected to occur at locations where magnetic field lines are tangent to the resonant mod-B surface. The dotted line indicates these "tangent" points which form a baseball seam on the resonant surface.

less than 60 percent as compared to the 90 percent absorption of the total microwave power injected into the cavity [Hokin,1987].

The non-relativistic ECRH resonance occurs on the mod-B surface with a magnetic field of 3.75 kG. The ECRH heating rate is expected to be linearly proportional to the time the electrons stay in resonance with the RF field. Strong heating is expected for plasmas on the field lines tangent to the resonance surface [Grawe, 1969]. Figure 2.2 is a plot of these 'tangent' points on the resonance surface. It is a baseball seam curve and is almost an image of the magnet.

2.1.3 Vacuum System

The vacuum system consists of the vacuum chamber, pumping system and the gas control and monitoring system. The 1/2 inch thick vacuum chamber consists of three sections (see Fig. 2.5). The center chamber is welded from two pieces to fit within the baseball magnet and it contains the entire mirror well. Two large fan tanks, about 1.5 meters in diameter and 2 meters in length, are located at the ends of machine

and are oriented at 90 degrees with respect to each other to fit the fanning of the quadrupole magnetic field. They are designed to reduce the interaction between the confined plasma in the center chamber and the end walls so that the effects such as line tying can be reduced.

The vacuum system is maintained by a turbomolecular pump, four titanium getters, and a cryogenic pump. The turbomolecular pump (Airco model 514) has a pumping speed of 500 litres/second and is operated at pressures below 60 mTorr. A 1500 litre/second mechanical pump (NRC model 100-S) is used as the roughing pump for the initial pump down. The getters are normally set at an emission rate of 0.01 gram/hour during the experiment.

The vacuum system is monitored with two ionization gauges located at the center chamber and the south fan tank. The base pressure is normally maintained at $1 - 4 \times 10^{-8}$ torr. In the experiment, the working gas (usually hydrogen) is puffed into the machine through a piezo-electric gas valve located at the bottom of the center chamber about 1 sec before the ECRH pulse. Plasmas can be generated at background gas pressures above 2×10^{-7} torr. The plasma equilibrium is typically measured at gas pressures between 5×10^{-7} and 5×10^{-6} torr.

2.1.4 Experiment Control

A micro-computer based process controller (Gould model 484) is used to control the timing sequences of the experiment and the vacuum magnetic field strength. The controller sends trigger pulses to various locations at the pre-set times, with a controllable time step of 0.1 sec and an accuracy of 1 ms. Various safety interlocks are also connected to the process controller.

The Constance magnetic field geometry is fixed by the baseball magnet. Three conditions can be varied in an experiment: the magnetic field strength, the ECRH power, and the neutral gas pressure. The standard operating condition for the equi-

librium measurements is $B_0 = 3$ kG, ECRH power = 2 kW, and a hydrogen gas pressure of 5×10^{-7} Torr.

The time sequence of the experiment is typically set as follows. When a shot trigger pulse is sent to the controller, the magnet current is turned on and raised to the preset value. Half a second later the gas puff valve is opened to raise the background pressure to about 5×10^{-7} torr. Another second later when the magnetic field is stabilized, a trigger is sent to the CAMAC data aquisition system. This time is marked as $t = 0$ for all the experimental data. The ECRH is turned on at $t = 0.2$ sec to break down the gas, which can be seen from Fig. 2.3. The plasma density reaches its full value of about 4×10^{11} cm^{-3} for the above conditions within a few milliseconds after the break-down. The total stored energy, which is mainly contributed by the hot electrons, takes about 0.2 – 0.3 sec to reach steady state. The ECRH power is turned off at $t = 1.5$ sec to observe the plasma decay. The shot ends at $t = 2$ sec when the magnet is turned off. All the stored data is then processed with a VAX 11/750 and a VAX 8300 computer. The experiment cycle is normally 5 – 6 minutes between shots, which is primarily limited by the cooling speed of the magnet.

2.1.5 Data Acquisition

A CAMAC-based data acquisition system is used in the Constance experiment in conjunction with a VAX 11/750 computer. It uses a VAX/VMS data acquisition software package MDS [Fredian and Stillerman, 1985] to set up and control the data system and to process the signals.

A large variety of waveform digitizers are used. These digitizers can be catalogued into three groups according to their sampling rates. The slow ones (LeCroy 8212) are used at a sampling rate of 2 kHz to store equilibrium signals throughout the shot. The medium speed ones (LeCroy 2264), with up to a 4 MHz sampling rate, are used for measuring the plasma fluctuation levels at different times during a shot.

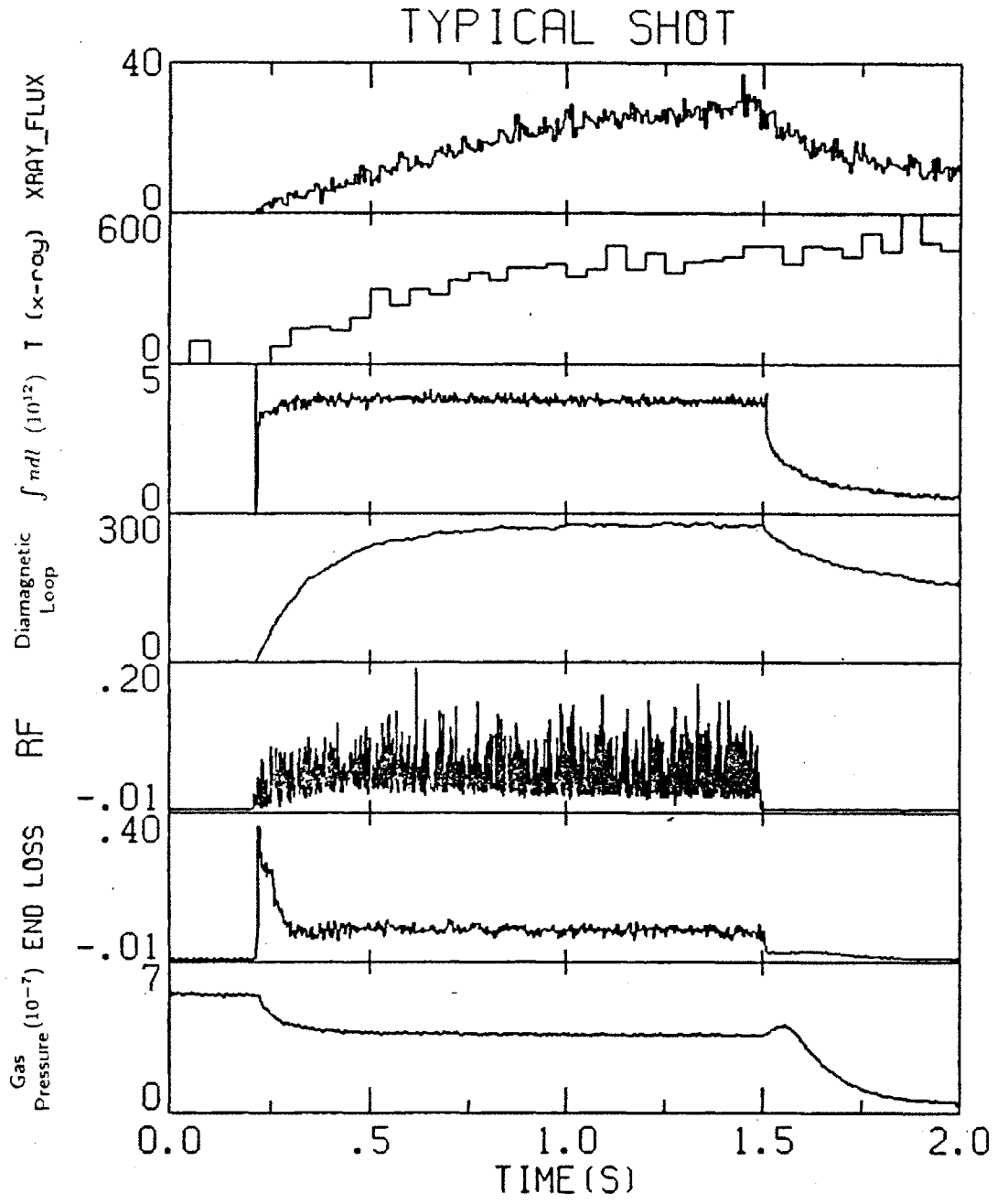

Figure 2.3: A typical shot taken for the standard machine operating conditions.

The fast ones (LeCroy 2256 at 20 MHz and Transiac 2001 at 100 MHz) are used to investigate individual instability bursts which last for only a few microseconds. There is also a phase digitizer (Jorway 1808) for the microwave interferometer, and PHA modules (LeCroy 3512/3587/3588) for the time-resolved x-ray pulse height spectra. The digitizers are mostly triggered by a CAMAC timer (Jorway 221/222) which can be set with time divisions of a microsecond. For the instability study, the fast digitizers are triggered by the plasma instability signal through a Hewlett-Packard 8801A pulse generator in order to catch the bursts.

2.2 Diagnostics

A large variety of diagnostics have been developed and used in the experiment. For the equilibrium study, the primary diagnostics include diamagnetic loops, magnetic probes, charge-coupled device (CCD) visible light TV camera systems, x-ray pinhole camera systems, scintillator probes, skimmer probes and thermocouple probes. To investigate the stability properties of the plasma, fast B-dot probes, microwave detectors, and end loss detectors are mostly used. Here I will only describe the diagnostics which contributed to this thesis. Detailed description of some others can be found in the theses of Rich Garner [1986] and Sam Hokin [1987].

2.2.1 Diamagnetic Loops

Four diamagnetic loops with different geometries (circular, elliptical and baseball seam shaped) have been used in the experiment to measure the change in magnetic field due to plasma current. Figure 2.4 shows the electric circuit of the system. The 20 turn pickup loop is wound inside 1/2 inch diameter stainless steel tubing (0.01 inch wall thickness) and installed inside the vacuum chamber. The center point of the winding is grounded in order to reduce the common mode noise. The loop signal

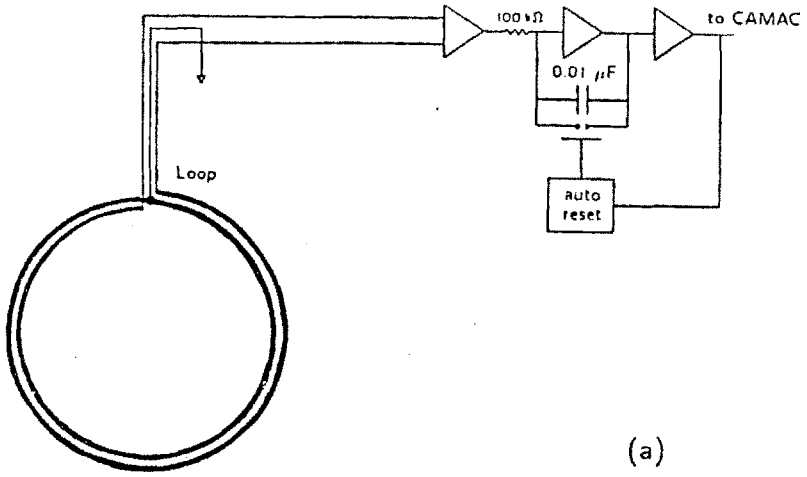

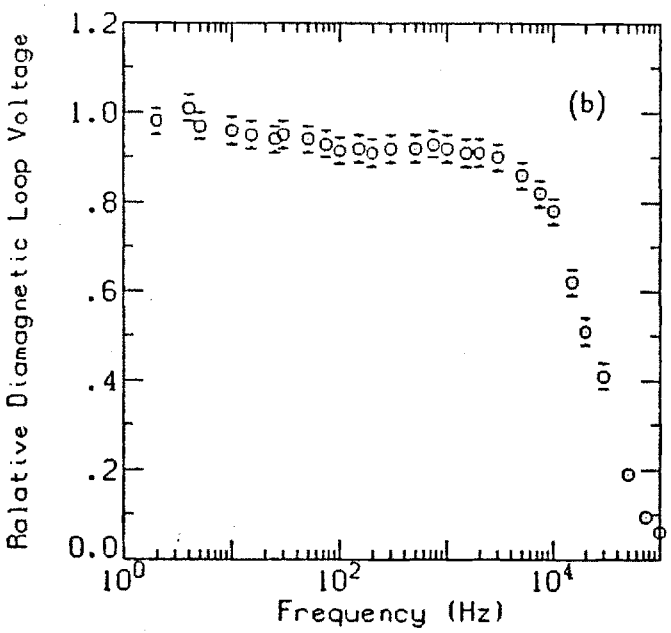

Figure 2.4: Diamagnetic loop system. (a) Functional Block diagram. (b) Frequency response of the circular loop at the magnetic midplane. The measured loop signals are normalized to numerical simulations which use vacuum boundary conditions.

is integrated by an active electronic integrator and then digitized.

The voltage induced across a diamagnetic loop is related to the rate of magnetic flux change by

$$\epsilon = -n\frac{d\phi}{dt}.$$

Where n is the number of the windings and ϕ the magnetic flux threading the loop. The obtained magnetic flux is related to the plasma current through

$$\begin{aligned}\phi &= \int \vec{B}\cdot d\vec{S} \\ &= \oint \vec{A}\cdot d\vec{l} \\ &= \oint d\vec{l}\cdot[\frac{\mu_0}{4\pi}\int \frac{\vec{J}(\vec{r'})}{\vec{r'}-\vec{r}}d^3r'].\end{aligned}$$

If a fluid-like equilibrium is assumed, the plasma current is determined by

$$\vec{J}_\perp = \frac{1}{B}\vec{b}\times\nabla\cdot\mathbf{P},$$

where P is the plasma pressure tensor. Because the magnetic flux is proportional to the current density $\vec{J}$, and hence proportional to P/B, the plasma pressure and the total stored energy can be obtained from the diamagnetic loop measurement when the plasma profile is known.

An Evans 4031 gated electronics integrator is modified for use in our system. The integrator works such that

$$V_{out} = \frac{1}{RC}\int_{t_1}^{t_2} V_{in}dt$$

The modification is focused on reducing the integrator noise level because this is the limiting factor for the measurement accuracy. A detailed description of the integrator circuit and the modifications is given in Appendix B.

Diamagnetic loops are calibrated with externally driven current coils both inside and outside the vacuum chamber to test the electrical circuits and the system frequency response in the aluminum vacuum chamber. The calibration shows that the

loop response is affected by the vacuum chamber at frequencies above 10 Hz (see Fig. 2.4b.), which agrees well with the calculated 0.09 sec penetration time of the 1 cm thick wall. At frequencies above 100 Hz, the diamagnetic loop signal is reduced by about 6 - 10 percent due to the conducting wall. The loop response drops sharply near 10 kHz because of the cutoff due to the 0.01 inch stainless steel tubing. At a frequency of 2 Hz, the effect of the wall is not observable within the calibration accuracy of 3 to 5 percent. This is the estimated accuracy for using oscilloscopes for the frequency and voltage measurement.

A drift subtraction technique is used in the experiment to compensate the cumulative integrator drift. After the vacuum magnetic field is stabilized in a shot, the integrator drift level is digitized for a 0.2 sec time interval before the plasma generation. The drift is later fit to a linear function during the data processing and subtracted.

2.2.2 Magnetic Probes

Two types of magnetic probes are used in the experiment to measure the local equilibrium diamagnetic fields: B-dot probes and Hall probes. Details of the electronic circuits for these probes are described in Appendix B (also see [Chen, 1987]).

The B-dot probe system consists of a pickup coil and a low drift electronic integrator, similar to the electrical circuits of the diamagnetic loops except for the differences in the loop sizes. The probes are constructed on small fiberglass supports with No. 40 magnet wire and installed in half inch diameter stainless steel tubing. The same drift subtraction technique used for diamagnetic loop signal processing is used for B-dot probes. The probe sensitivity is about 0.1 gauss.

The Hall probe system consists of a Hall effect sensor and a digital sample-and-hold electronic circuit for vacuum field subtraction. A commercially made Hall effect integrated circuit (Sprague model UGN-3501M) is used as the sensor. With the

sample-and-hold amplifier, a probe sensitivity of about 0.1 to 0.2 Gauss in a background field of 5 kG is obtained.

The calibration of the magnetic probes is done in a 3 inch diameter Helmholtz coil. The calibration accuracy is determined by the use of the oscilloscope, which is about 3 – 5 %.

2.2.3 CCD TV Camera[1]

Two dimensional plasma visible light images are measured with a solid-state TV camera system, which uses a Pulnix TM-34K charge-coupled device (CCD) TV camera to image the plasma and a video cassette recorder to store the data. The resolution of the camera is 384×491 pixels and it has a time resolution of 30 ms/frame. The camera is sensitive in the spectral range 4000 – 10000 Å and its energy sensitivity is 0.3 erg/sec at 6000 Å. It can be used in the several kilogauss magnetic field environment without extra magnetic shielding.

The plasma image measured with the camera is a projection of the 3-D plasma profile. Because the plasma cross section is non-circular, the radial plasma profile cannot be inverted with the usual Abel inversion. We integrate model plasma profiles along the line-of-sight of the camera and compare the numerically line integrated profiles with the plasma image to determine the radial plasma profile.

2.2.4 X-ray Pinhole Camera

The x-ray pinhole camera setup is shown in Fig. 2.5. It consists of a cone shaped lead pinhole for x-ray imaging and a recording system to store the data. The 1 mm aperture lead pinhole uses a 0.001 inch thick beryllium foil as both the x-ray and the vacuum window and is designed to mount on a KF-40 gate valve so that it can be installed without breaking the vacuum. It is normally located at the magnetic

[1]The CCD TV camera system was set up by Donna Smatlak.

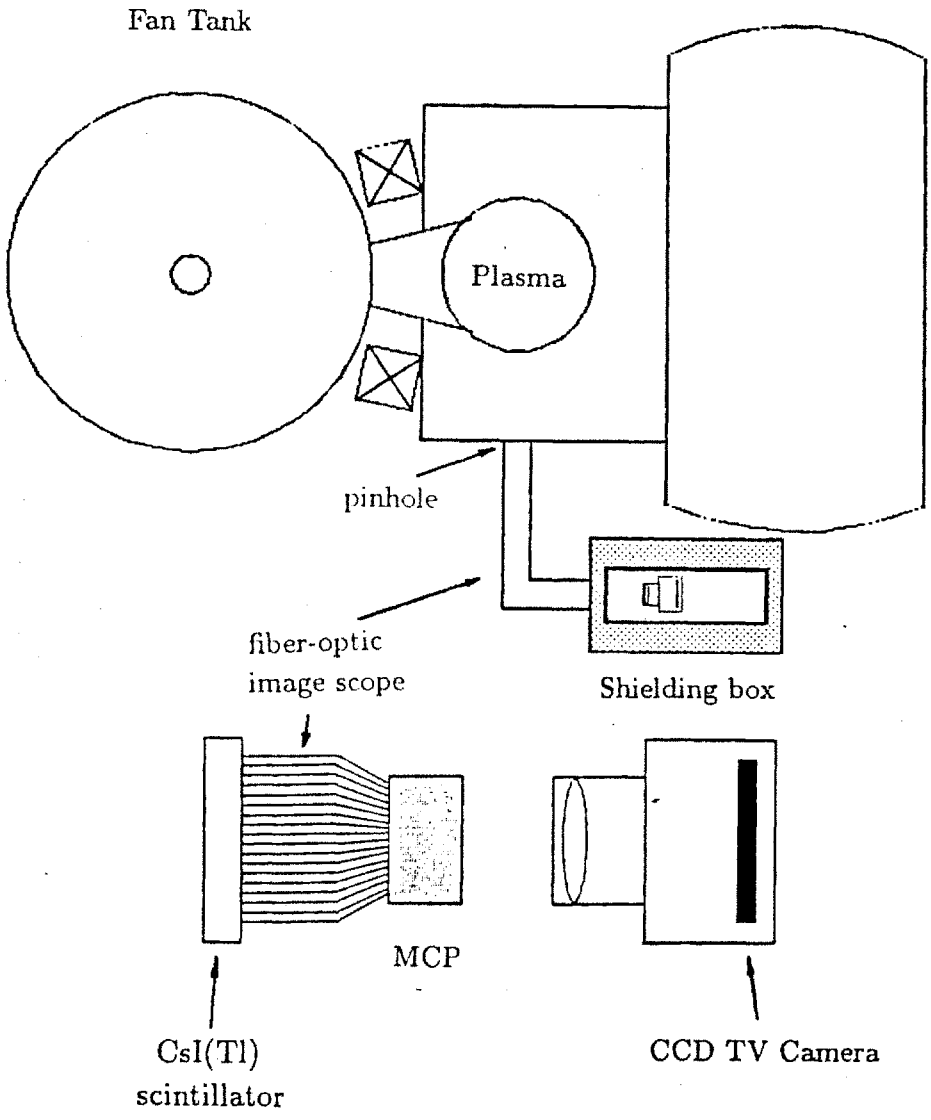

Figure 2.5: Experimental setup of the x-ray pinhole camera system. (a) System assembly on the machine. (b) Scintillation TV camera setup. The shielding box for the multichannel plate (MCP) image intensifier and the TV camera is rotated for easier magnetic and x-ray shielding.

midplane at a distance of 68 cm from the magnetic axis. The pinhole assembly gives a camera spatial resolution of about 1 cm in the center of the machine.

Time integrated images are measured by direct exposure of x-ray films. The film is mounted behind the lead pinhole and exposed for a few shots. A medium speed, fine grain x-ray film (Kodak BB5) is used. The film is calibrated using the plasma as an x-ray source. Figure 2.6(a) shows the calibration of the relative film density as a function of the exposure time. The calibration covers a much larger range than the film is normally exposed and shows that the film response is essentially linear. Fluorescent intensifying screens (Kodak X-OMATIC Regular Screen) are sometimes used with the x-ray film. The required exposure time can be reduced by a factor of 2 – 3 with the use of the intensifying screen. These screens select an energy window of 50 – 200 keV x-ray photons, which is desirable because the x-ray flux in this range is insensitive to the variation in the plasma temperature. However, the spatial resolution is degraded by a factor of 2 with the use of these screens.

Time resolved x-ray images are measured with a scintillation TV camera system. A 2 mm thick CsI(Tl) crystal scintillator is placed behind the pinhole to convert the x-ray image to visible light. The visible light image is then transmitted through a 2.5 cm × 2.5 cm coherent fiber-optic image scope to a multichannel plate (MCP) image intensifier and amplified by a factor of 40,000. The amplified image is subsequently recorded with a CCD TV camera. The time resolution of the system is determined by the speed of the CCD TV camera, which is 30 ms/frame. The choice of CsI(Tl) crystal scintillator is based on its light emission spectrum. The energy conversion efficiency of CsI(Tl) scintillator is about half that of NaI scintillator. However, the peak of the emission spectrum for CsI(Tl) is at about 5800 Å compared with 4200 Å for NaI(Tl). In a system which uses a fiber-optic image scope and MCP intensifiers, response at longer wavelengths is more desirable. Figure 2.6(b) shows the transmission

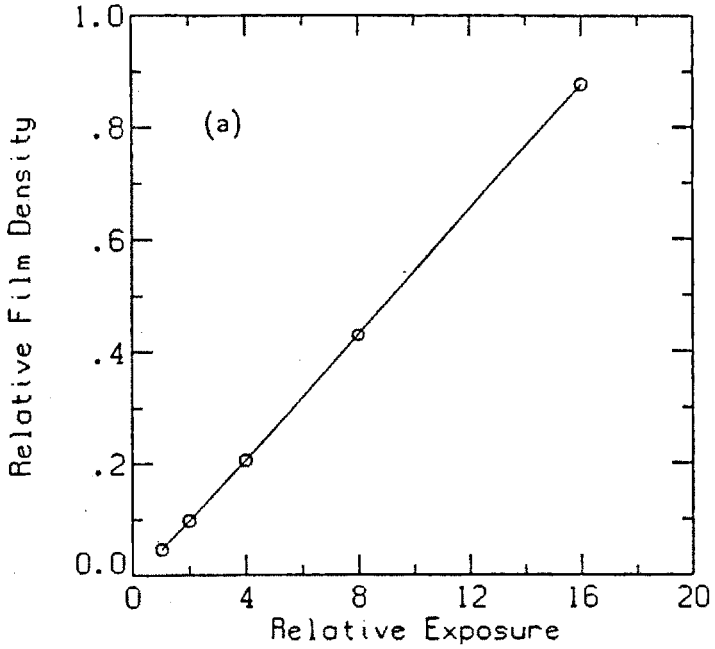

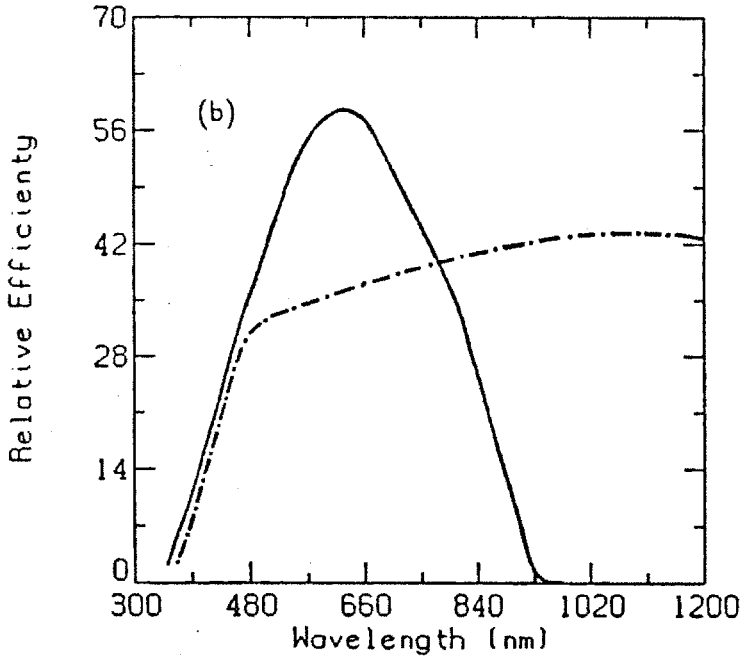

Figure 2.6: (a) Calibration of the x-ray film (Kodak BB5) shows that the film response to x-ray flux is linear in the range in which the film is used. (b) Spectral response of the fiberoptic image scope (dash-dot line) and the MCP image intensifier (solid line) have a sharp cut-off below 4500 Å. (Data from Galileo Electro-Optics Corp. and Hamamatsu Corp.)

efficiency of the fiber-optic image scope and the gain of the MCP image intensifier versus wavelength. Both of them drop sharply below 4500 Å. The use of CsI(Tl) instead of NaI(Tl) therefore increases the system sensitivity by a factor of more than 3.

2.2.5 Microwave Interferometer[2]

A single channel 24 GHz microwave interferometer is used to measure the line integrated plasma density. The interferometer is located at the midplane and oriented at 45 degrees with respect to the symmetry plane. The microwaves are launched perpendicular to the magnetic axis with electric field polarized along the z-axis. The index of refraction for these O-mode waves is approximately

$$\epsilon = 1 - \frac{\omega_p^2}{\omega^2} < \frac{1}{\gamma} >,$$

where $< \frac{1}{\gamma} >$ is an approximate relativistic correction to the cold plasma dielectric caused by the relativistic mass shift [Mauel, 1985]. The unfolding of the line integrated plasma density is dependent on the radial plasma profile. This profile information is obtained from the visible light and x-ray imaging which have good spatial resolution.

2.2.6 X-ray Spectroscopy[3]

X-ray spectroscopy is used to measure the hot electron temperature. Three x-ray detectors have been used in the experiment, covering an x-ray photon energy range from 1 keV to 1.5 MeV. The detectors include a NaI(Tl) detector for energies from 30 keV – 1.5 MeV, a high-purity germanium detector for 2 – 150 keV, and a Si(Li) detector for 1 – 12 keV. The NaI(Tl) detector is the standard diagnostic and is normally used to monitor the plasma temperature.

[2]The interferometer hardware was set up by Donna Smatlak and the software was written by Evelio Sevillano.

[3]The x-ray spectroscopic measurement was conducted by Sam Hokin.

The scintillator detectors use a scintillator to convert the x-rays to visible light photons. These photons are subsequently amplified by a photomultiplier tube and recorded with a pulse height analyzer which counts the x-ray photons at a given energy.

With the measured x-ray count spectrum $dN/d\omega$, the plasma temperature is then determined by fitting the measured spectrum to the theoretical curves calculated using a Maxwellian distribution with different temperatures. However, the measurement gives only the line integrated temperature. In order to invert the chord averaged spectra to obtain the radial temperature profile, one has to first unfold the spectra for each energy channel, which results in spectra versus radius, and then determine the temperature as a function of radius from each of the inverted spectra. Because of the complicated magnetic geometry involved, no attempt is made to make such an unfolding.

2.2.7 Skimmer Probes and Thermocouple Probes

Skimmer probes are used in the experiment as limiters to determine the radial and axial extent of the hot electrons. These probes are simply 1/4 inch aluminum rods which can eliminate the plasma at the probe location. Much higher sensitivity is obtained by installing a thermocouple on the tip of a skimmer probe so that the plasma boundaries can be determined from the measurement of the probe temperature. Chromel-Alumel thermocouples, which can be used to 1400 C°, are used with the skimmer probes. The construction of the thermocouple probe is shown in Fig. 2.7. The thermocouple joint is soldered inside a 3 mm diameter stainless steel shell and it is supported only by the two wires to minimize thermal conduction. The reference joint is at the connector end of the probe. Thus room temperature is used as the reference point.

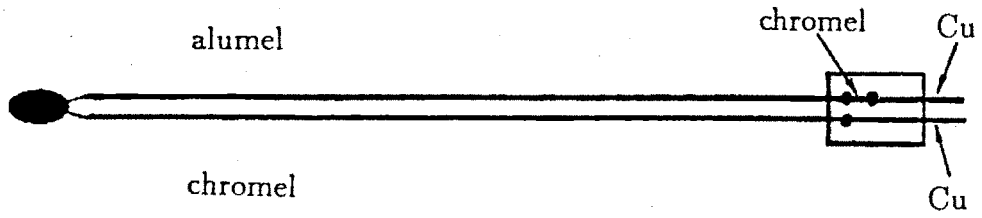

Figure 2.7: Construction of the thermocouple probe.

2.2.8 End Loss Detectors[4]

Plasma end loss is monitored by a set of end loss detectors. Three types of the detectors are used, including electron end loss analyzers (ELA), Faraday cups, and segmented net current detectors. Arrays of five electron end loss analyzers, five Faraday cups and ten net current detectors are installed at each end of the machine. Figure 2.8 shows the spatial positions of these detectors and their corresponding positions at the magnetic midplane as mapped along field lines.

The ELA's consist of three biasing grids and a current collector. The first grid is normally biased at +1000 Volts to repel the incoming ions. The second grid is swept from 0 to −5 kV to discriminate electrons in this energy range. The third grid is biased at −30 to −50 Volts to force back the secondary electrons emitted from the current collector. Thus the electron end loss spectrum below 5 kilovolts can be measured.

A Faraday cup consists of one repelling grid and a cup shaped current collector. The repelling grid is biased either at positive voltage to repel ions or at negative voltage to repel electrons. The cup shaped current collector is designed to reduce

[4]The end loss diagnostics were set up by Rich Garner and Dan Goodman.

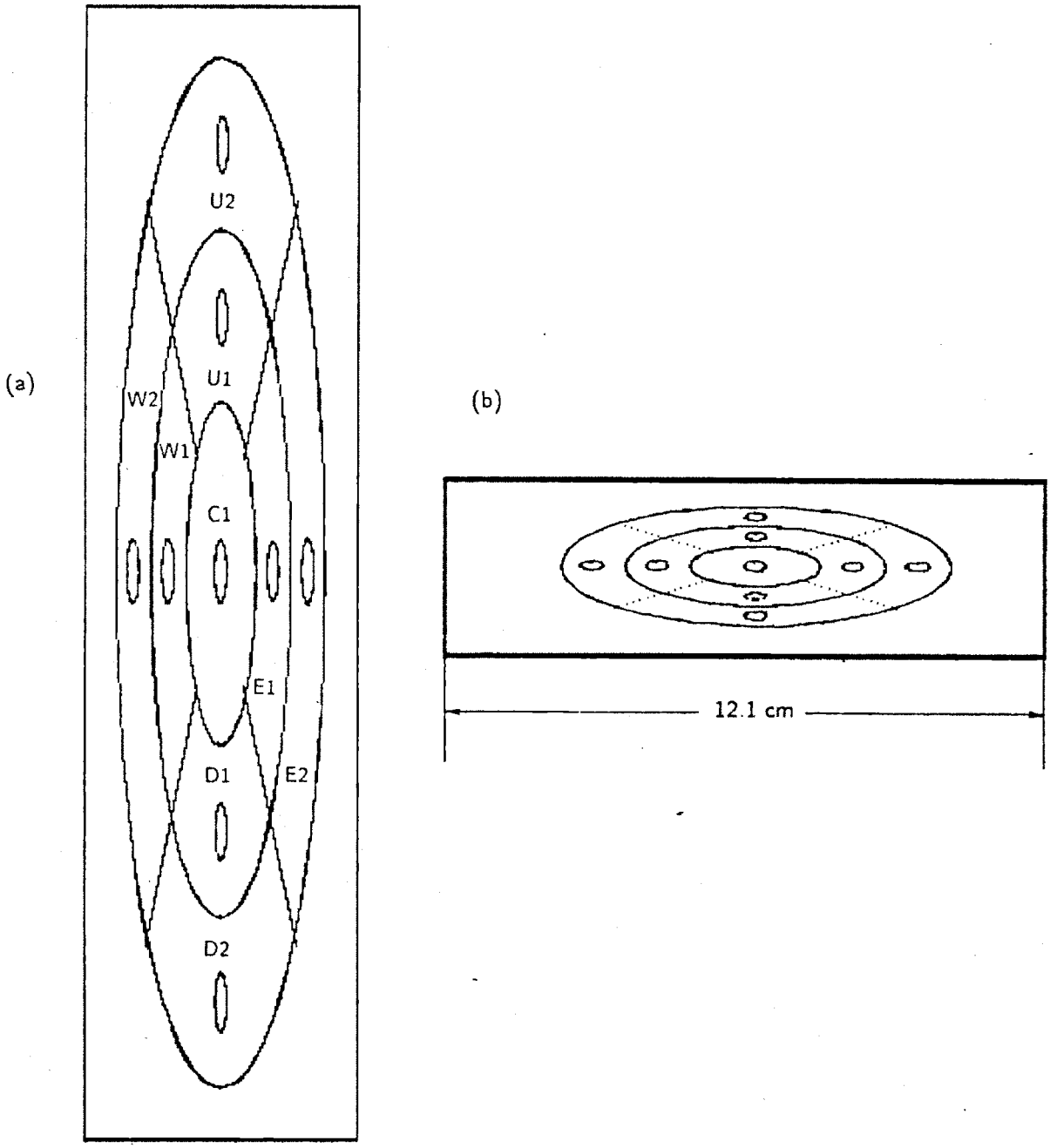

Figure 2.8: Geometry of the end wall diagnostic plate. (a) End wall plate. (b) Detector positions mapped to the midplane.

losses due to secondary electron emission.

The net current detector consists of only a current collector plate and has no biasing grids. It collects all the electron and ion end loss current. Because of the large area of these end loss plates and their symmetric location on the end wall, these net current detectors are very sensitive to the end loss bursts and provide detailed information about the radial structure of the plasma fluctuations.

2.2.9 Microwave Emission Detection[5]

An open ended rectangular waveguide (lower cutoff at 5.4 GHz) is installed on the top of the central chamber as the receiver to measure microwave emission from the plasma. The received RF emission is transmitted through an elliptical wave guide to the diagnostic rack and then split into three paths by two directional couplers. The split signals are analyzed to obtain the total RF power, RF power with the 10.5 GHz ECRH frequency subtracted (in a 1 MHz wide band), and the RF emission spectrum. The RF emission spectrum measurement has been a primary diagnostic for the microinstability study. For the MHD instability measurement, the power of the RF emission is used to monitor the strength of the microinstability activities.

2.2.10 Fast B-dot Probes

Fast B-dot probes are used to measured plasma magnetic fluctuations in the frequency range between 100 kHz and 30 MHz. The probe is made of a 5 turn pickup coil 0.8 cm in diameter and is covered by a ceramic tip to protect the coil from the plasma electric field and allow the fluctuations of the magnetic field to penetrate. In the experiment the probe is electrically isolated from the vacuum chamber to reduce noise, and is matched to 50 ohms to avoid reflections of the transmission line. The magnetic signal is amplified by Mini-Circuits model ZHL-32A RF amplifiers and then digitized with

[5]The microwave emission detector was set up by Rich Garner.

fast waveform digitizers.

2.2.11 Scintillator Probes[6]

An array of scintillator probes is used to measure the hot electron end loss distribution. These probes consist of small cylindrical plastic scintillator (4 mm diameter, 8 mm length) optically coupled to photo-multiplier tubes through fiber-optic guide. The openings to the scintillators have entrance windows made of foils of various thickness for electron energy discrimination. The NE102 plastic scintillator has a fairly constant energy conversion efficiency of about 3 % at electron energy above 125 keV. They produce a signal proportional to the end loss power density and are used for both the equilibrium and stability measurement. The probes are absolutely calibrated on a test-stand with 30 keV electron beam. The detailed analysis of probe response has been given by Hokin [1987].

2.2.12 Surface Barrier Detectors

Silicon surface barrier detectors (SBD) are used to monitor the x-ray emission from the plasma. A surface barrier detector is a reversely biased planar diode with metal coating on both sides of the wafer. The reverse-bias voltage creates a depleted region in the wafer. X-ray photons striking on the detector knock out bound electrons. The free charge carriers subsequently drift across the junction and are collected as detector current.

A four-detector SBD array has been built in order to measure both the spatially and temporally resolved x-ray emission profile. The detectors were relatively calibrated using the plasma as the x-ray source. 1 mm thick stainless steel tubing is used as the collimator. The spectral response of the detectors is limited to photons with energies less than 20 keV. This response is mainly determined by the thickness of the

[6]The scintillator probe was built by Sam Hokin.

wafer [Wenzel and Petrasso, 1988], which is 150 nm for the detectors used (EG&G Ortec B-016-025-150). However, expected spatial resolution was not obtained with this detector array. It is likely that high energy x-rays penetrating the collimator generate low energy x-ray photons which can be seen by the SBD. However, no further effort was made to improve the detector collimation.

Chapter 3

The Constance B Plasma and Equilibrium Modelling

This chapter presents the general properties of the plasma in the Constance B mirror, especially its equilibrium structure, and develops a theoretical plasma pressure model. The model is then used to make quantitative determination of the equilibrium by comparing the predictions of the model with the measurements. The detailed experimental comparisons are presented in the next chapter.

3.1 Description of the Plasma

3.1.1 Plasma Components

The use of electron cyclotron resonant heating for plasma generation results in an average electron energy substantially higher than the ion energies in Constance. There exist two major electron components in the plasma: an electrostatically confined cold electron population with a temperature on the order of 50 – 100 eV, and a magnetically confined hot electron population with an average energy on the order of 400 keV. The densities of these two electron populations are both on the order of a few times 10^{11} cm^{-3}. A small population of intermediate temperature warm electrons (1 – 3 keV, 3 $\times 10^{10}$ cm^{-3}) also exists in the plasma, and it has been determined to be the driving force for the microinstabilities [Garner, 1986]. Typical plasma parameters

Midplane magnetic field	3.0	kG
Gas pressure	5×10^{-7}	torr
ECRH power	2	kW
Peak plasma beta	0.3	
Cold electron density	2×10^{11}	cm^{-3}
Warm electron density	3×10^{10}	cm^{-3}
Hot electron density	$3 - 4 \times 10^{11}$	cm^{-3}
Cold electron temperature	50 – 100	eV
Warm electron temperature	1 – 2	keV
Hot electron temperature	400 – 450	keV
Ion temperature	15 – 30	eV
Total stored energy	80	J
Total plasma volume	8	litres

Table 3.1: Constance B plasma parameters.

are shown in Table 3.1.

The Constance B plasma is dominated by the energetic electrons. The hot electron temperature is measured with the hard x-ray detectors. Figure 3.1 shows an x-ray intensity spectrum versus photon energy measured with the NaI(Tl) scintillator detector together with theoretical spectra for a Maxwellian distribution with $T_{eh} = 377$ keV. The lower curve is a modified theoretical spectrum with the detector response taken into account. The hot electron heating rate (dW/dt) is observed to be essentially a linear function of the ECRH power (P_{rf}), with a relation $(dW/dt) \cdot P_{rf}^{-1} = 550$ keV/(sec $\cdot$ kW) until the hot electron temperature saturates at about 450 keV. This saturation temperature is only weakly dependent of the ECRH power, background gas density, or the magnetic field strength. The density of the hot electron component is measured from the interferometer signal during the plasma decay. Figure 2.3 showed the plasma density, diamagnetism, and the x-ray temperature as functions of time during a shot. After the ECRH is turned off, the cold electrons are scattered into the loss cone within a hundred microseconds while the hot electron confinement time is on the order of 2 seconds, because the collision rate is proportional to $T^{-3/2}$. The sharp drop of the plasma line density immediately after

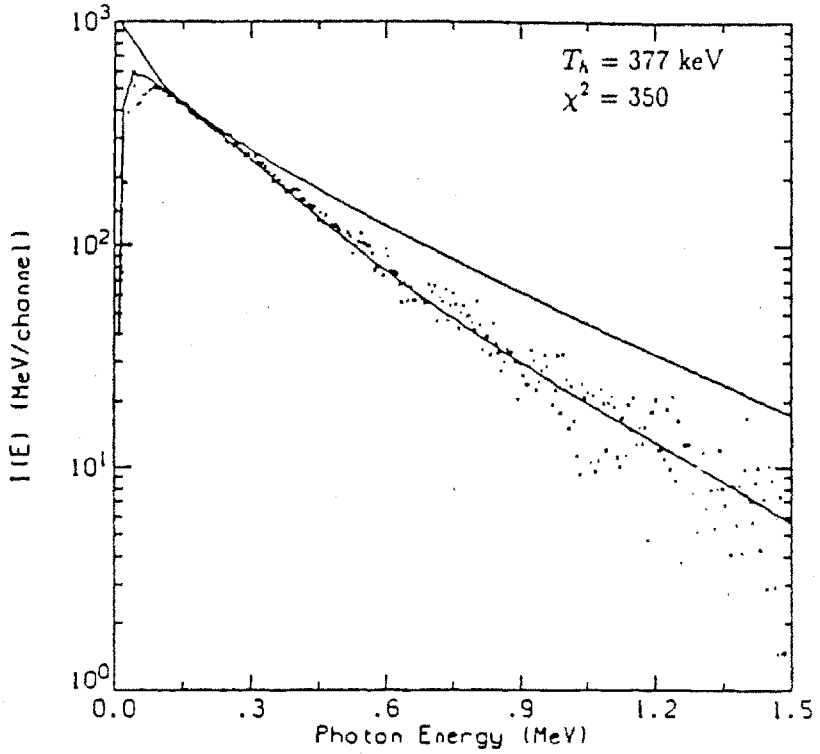

Figure 3.1: An experimental x-ray intensity spectrum and theoretical spectra for a Maxwellian electron distribution with T_e = 377 keV. The upper solid curve is the pure theoretical spectrum and the lower curve is modified with the detector response taken into account.

the ECRH turn-off indicates that about half of the electrons are hot.

The cold electron temperature is found using two methods. The first method involves measurement of the electron end loss rate and the plasma potential, and then uses the Pastukhov confinement relation to estimate the electron temperature. When the particle collisional time scale is long compared with the bounce time, the electron confinement time in a mirror field with an electrostatic potential ϕ is given by [Pastukhov, 1974; Cohen, 1978]

$$\tau_{ec} = \tau_{ee}\frac{\sqrt{\pi}}{4}g(R)\frac{1}{I(e\phi/T_{ec})}\left(\frac{e\phi}{T_{ec}}\right)\exp(e\phi/T_{ec}),$$

with

$$g(R) = \binom{R+1}{R}^{1/2}\ln\left[2R+1+2\sqrt{R(R+1)}\right],$$

$$I(\frac{e\phi}{T_{ec}}) = 1 + \frac{\sqrt{\pi}}{2}\left(\frac{e\phi}{T_{ec}}\right)^{-1/2} \exp\left(\frac{e\phi}{T_{ec}}\right)\left[1 + erf\left(\sqrt{\frac{e\phi}{T_{ec}}}\right)\right],$$

$$\tau_{ee} = 3.41 \times 10^5 \frac{[T_{ec}(eV)]^{3/2}}{n_e \ln\Lambda}.$$

Where R is the mirror ratio. The cold electron temperature can be numerically calculated if the plasma potential, the confinement time, and the electron density are known. The plasma potential measured with emissive probes at the plasma edge is about 100 - 150 V. For $n_e = 2 \times 10^{11}$ cm^{-3}, $\tau_{ec} = 1$ ms, $\ln\Lambda = 15$, and $R = 1.89$, the resulted electron temperature is 40 - 80 eV.

The second method of electron temperature measurement involves measurement of plasma line radiation spectra [Podgornyi, 1971]. This measurement is conducted by Goodman [1988] in helium plasmas. The radiation intensities of two particular transitions, $4^1D \rightarrow 2^1P$ (4922 Å) and $4^3S \rightarrow 2^3P$ (4713 Å), are measured to estimate the relative cross sections of the two transitions. The theoretical transition rates for these two lines are averaged over a Maxwellian electron distribution and the ratio between the two transition rates can be expressed as

$$R(u_0) \equiv \frac{< \sigma v >_t}{< \sigma v >_s} = 2.53 \frac{E_2(1/u_0) - E_4(1/u_0)}{E_0(1/u_0) - E_1(1/u_0)},$$

with $u_0 = 24.0$ eV$/T_e$ and $E_n(x)$ is the exponential integral of order n. By measuring the line ratio with an absolutely calibrated digital storage CCD TV camera, the two-dimensional line averaged electron temperature profile is measured. The average electron temperature measured using this method is 40 - 100 eV. The accuracy of the measurement is estimated to be about 30 - 40 %.

The ion temperature is measured with a time-of-flight analyzer and the line radiation spectra in a helium plasma [Petty, 1988]. The helium ion end loss temperature measured from the spreading of the ion current in the time-of-flight analyzer is about 7 eV when the ECRH power is 1 kW. It increases linearly with the ECRH power

between 1 – 4 kW at a rate 7 eV/kW. From the Doppler broadening of the IIe II line ($\lambda = 4685.7\mathring{A}$), the ion temperature is determined to be about 7 eV and relatively insensitive to the RF power. This difference can be explained by the increased microinstability activities with the RF power increase. The electromagnetic fluctuations "kick" the ions into loss cone and increase their energy spread, resulting in an increased effective end loss temperature. The error bars for these measurements are estimated to be about 10 – 20 %.

3.1.2 Plasma Confinement

The primary loss of plasma in Constance is through the loss cone. The hot electron population is magnetically confined. The loss of these electrons is caused by Coulomb collisions between particles, microinstabilities and the ECRH induced RF diffusion. The latter two loss channels are the primary loss mechanisms when the ECRH is on. The effect of microinstabilities and ECRH induced RF diffusion on hot electron confinement was studied by Hokin [1987] in his thesis research. The hot electron confinement measurement is best illustrated in the shot shown in Fig. 3.2. In this shot, the ECRH is turned on twice, from $t = 0.2$ to 1.2 sec and from $t = 1.7$ to 1.9 sec. From plasma breakdown until $t = 1.2$ sec, all three end loss mechanisms are contributing to the plasma end loss. After the ECRH is turned off at $t = 1.2$ sec together with the gas puff, the microinstabilities go away. The plasma subsequently decays solely due to collisions while the background gas is being pumped away. At $t = 1.7$ sec, the ECRH is turned on again. Because there is no gas puff, the plasma is stable to microinstabilities and decays primarily due to ECRH induced diffusion and collisions. From the plasma energy loss rate measured with the scintillator probe outside the mirror throat, the relative effect of the three loss mechanisms can be evaluated. The data shows that the hot electron confinement is predominantly limited by the RF and the microinstability induced diffusion. Quantitatively, the hot electron end loss

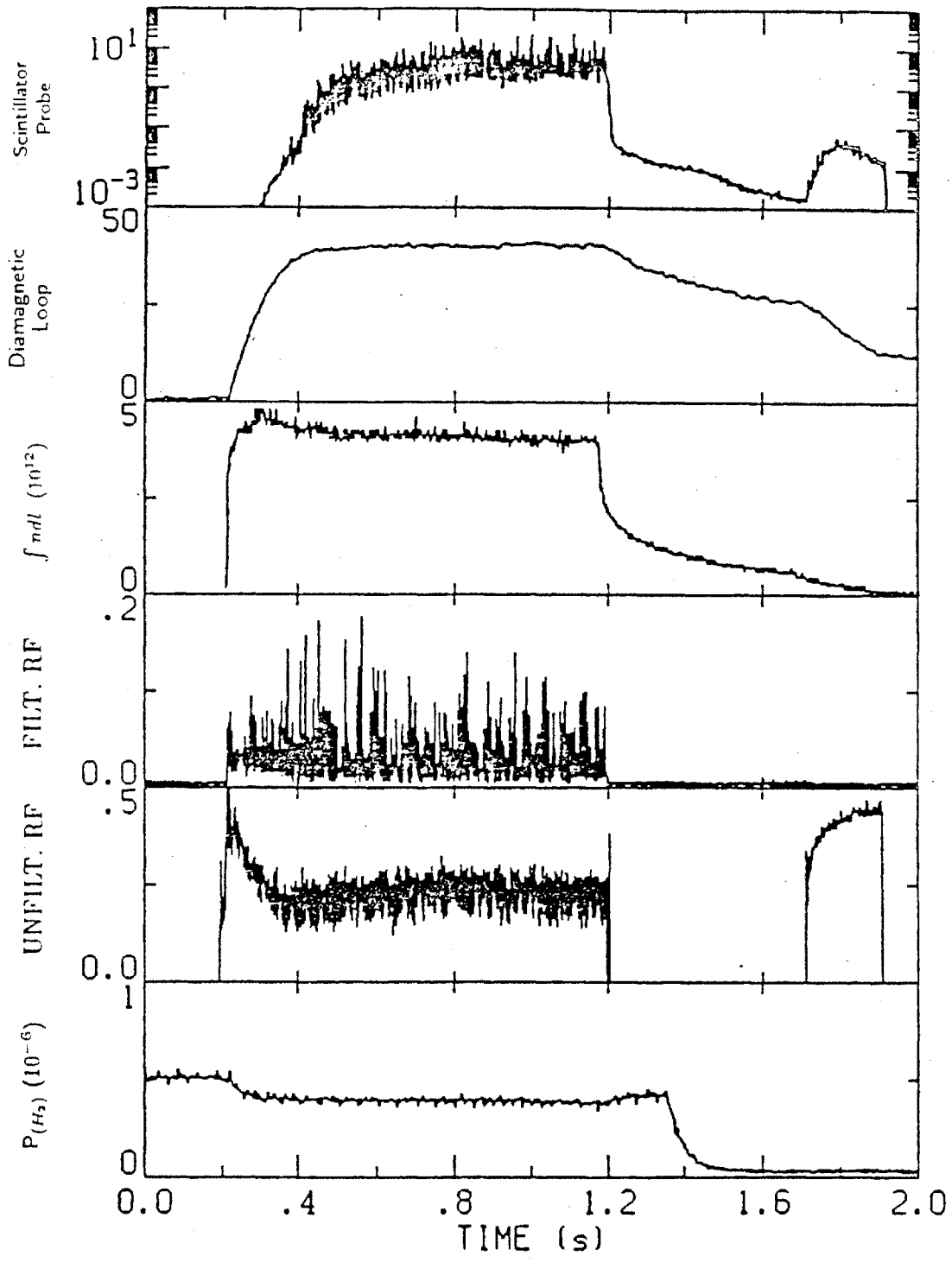

Figure 3.2: A shot with a second ECRH pulse after the gas-feed is off for measuring the RF induced diffusion.

rates due to the RF induced diffusion and the microinstabilities are on the order of 100 and 25 times higher than the losses due to Coulomb collisions, respectively.

The cold electron confinement is strongly affected by the plasma potential and the neutral gas pressure. The confinement time of these electrons is deduced from the measurements of the cold electron end loss rate and the line integrated density, using

$$\frac{1}{\tau_{ec}} = \frac{2}{< n_{ec} l >} \frac{J_{ec}}{e}.$$

Where J_{ec} is the electron end loss current density at one end of the machine, and $< n_{ec} l >$ is the cold electron line density along a field line. The measured cold electron end loss current density on the magnetic axis is about 3×10^{-4} amps/cm^2 when normalized by the midplane cross-section. The line integrated plasma density on the magnetic axis is about $< n_{ec} l > \approx 4 \times 10^{12}$cm^{-2}. We obtain a cold electron confinement time of about 0.8 ms, which agrees with the 1 ms calculated Pastukhov confinement time when $T_{ec} = 80$ eV is used.

The total stored energy is measured from the plasma diamagnetism. It is about 80 J in a typical shot. The corresponding average plasma beta is about 15 percent. Because the measurement is dependent on the plasma pressure profile, the total stored energy is calculated after the equilibrium pressure profile is determined. The calculation will be discussed in the next Chapter.

3.1.3 Microinstabilities

A plasma confined in a single mirror is intrinsically microunstable because the plasma distribution function is non-Maxwellian. A set of experiments was conducted by Rich Garner [1986] to study the whistler electron microinstability in the Constance B mirror. The diagnostics primarily included RF emission detectors and end loss analyzers. Two types of instabilities were observed. At low neutral pressures where the molec-

ular hydrogen gas density was in the range of $1 - 2 \times 10^{10}$ cm^{-3}, the instabilities occurred in bursts and the RF emission and the end loss were well correlated. The RF emission frequency was observed in the range of 6.7 – 8.7 GHz. At higher neutral pressures, the RF emission became continuous and it was associated with enhanced continuous end loss. The RF emission frequency increased to 8. – 10.5 GHz.

The instabilities were identified as whistler instabilities by comparing the observed mode frequencies with the theoretical analysis using an ECRH distribution function for the warm electron distribution. The calculation showed that the frequencies of the whistler instabilities which had the maximum growth rate were in the range below the electron cyclotron frequency, as has been observed in the experiment. It also predicted the bursting behavior of the instabilities. It was concluded that warm electrons in the energy range of 1 to 3 keV were responsible for the observed microinstabilities, based on the experimental observation that the microinstability occurred only when the warm electrons were present, and that the theory suggested that the relativistic hot electrons were stabilizing.

3.2 Characteristics of the Plasma Equilibrium

The plasma equilibrium is experimentally measured by a set of diagnostics, including x-ray imaging, visible light imaging, magnetic measurements, skimmer probe and end loss measurements.

The Constance B plasma equilibrium is characterized by a baseball seam structure of the plasma pressure and density. Figure 3.3 shows a set of visible light photographs of the plasma looking perpendicular to the magnetic axis during a shot. Immediately after plasma breakdown, the plasma image is slightly "C" shaped with a plasma stream on the magnetic axis. The on-axis plasma quickly decays as the plasma heats up. When the plasma reaches steady state, the image becomes a shallow "C" with

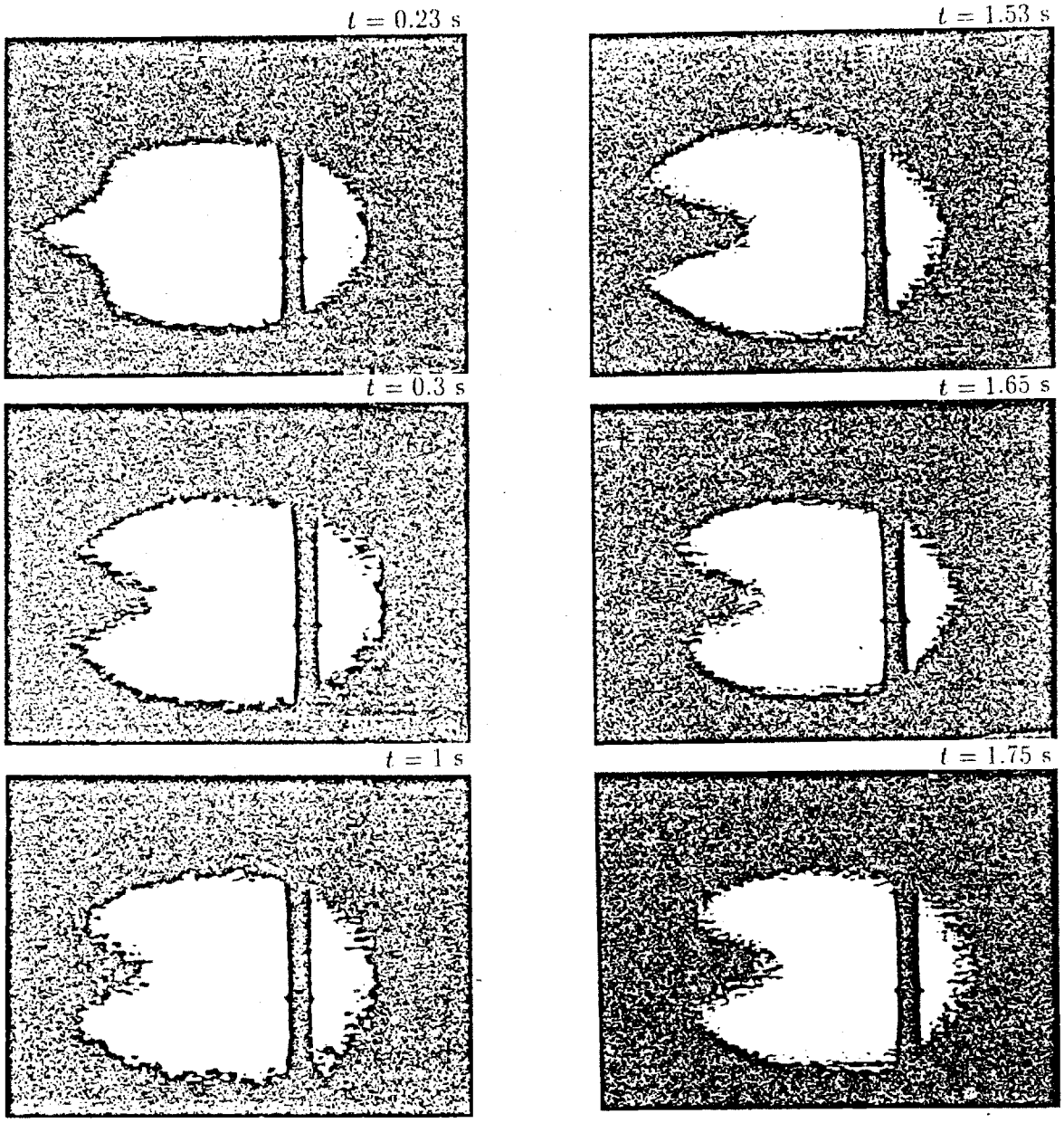

Figure 3.3: Visible light images of the plasma measured from the side view. The plasma breaks down at 0.23 sec and the RF is turned off at 1.5 sec. The vertical dark lines are the shadow of a diamagnetic loop.

the plasma size defined by the non-relativistic ECRH resonant surface. The opening of the "C" corresponds to the position where there is longest line-of-sight due to the magnetic flux fanning. From the photographs taken at $t = 1$ and 1.53 sec, we see that the "C" shaped image is more hollow right after the ECRH turn-off in comparison with the images measured during the steady state ECRH phase. The change of the hollowness corresponds to the loss of cold electrons, indicating that the hot electron profile is more hollow than the cold electron profile. The plasma diamagnetism experiences a quiescent decay in the afterglow with a decay time of about 2 seconds, and the image can be observed with the TV camera for up to half a second. In the shots where the gas pressure is lowered, the plasma image is observed to be "C" shaped from the beginning of the plasma breakdown.

Figure 3.4 shows a set of visible light pictures looking along the magnetic axis. There are four bright balls on the diagonal chords and a dimmer region near the axis, indicating that the plasma is radially hollow.

X-ray images measured with the x-ray pinhole camera are qualitatively similar to the visible light photographs, and show that the hot electrons are indeed contained in the "C" shaped region. Figure 3.5 shows a set of x-ray pictures obtained with the time resolved x-ray camera system during a shot. Since the camera is not synchronized with the shot, the time is not marked on the pictures. However, the x-ray images are hollow from the first frame in which the image can be observed, and keep the shape until the plasma decays. The x-ray images measured at different energy ranges and magnetic field strength are all similar, as shown in Fig. 3.6.

Because of the quadrupole symmetry of the vacuum magnetic field, the plasma image taken from the top of the machine is the same as those taken from the side except that the opening of the "C" is rotated by 180 degrees. These visible and x-ray photographs show that the hot electron plasma is primarily confined within the non-

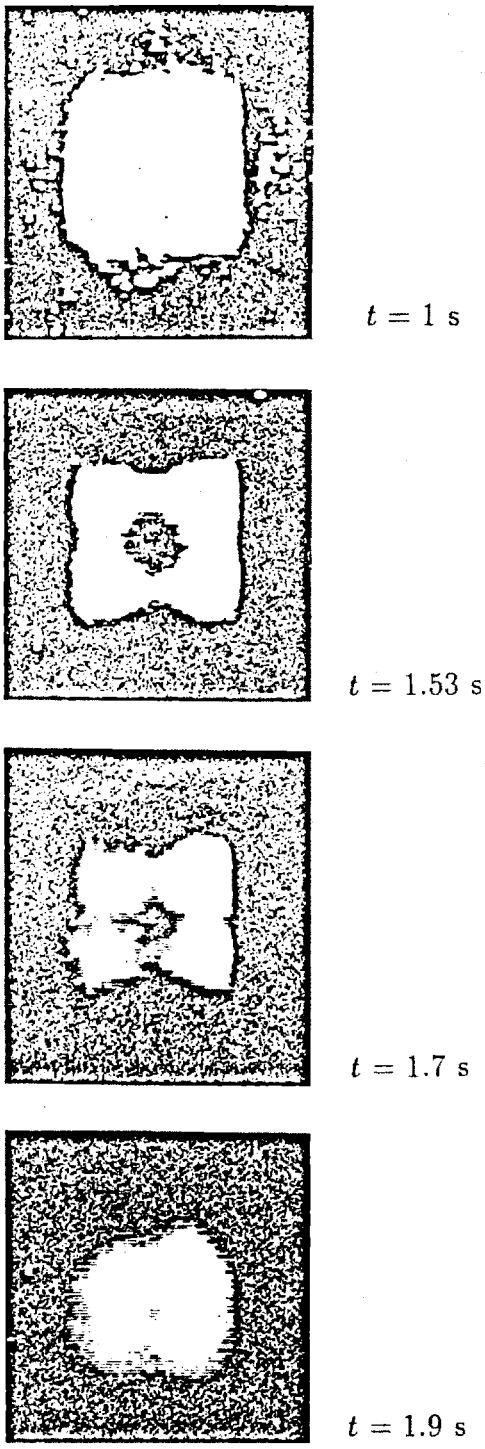

Figure 3.4: Visible light images measured from the end of the machine.

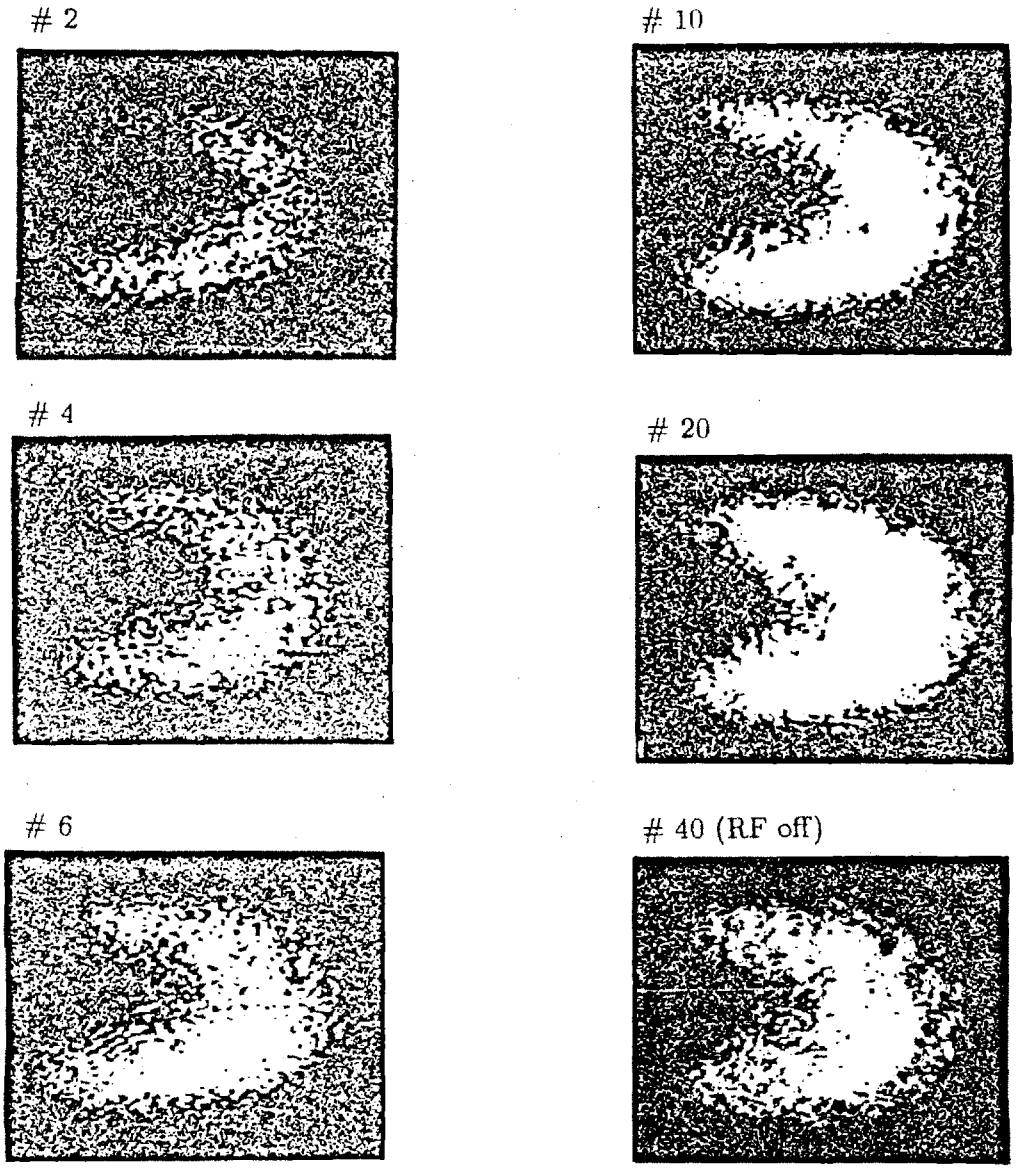

Figure 3.5: X-ray images of the plasma measured with the time resolved pinhole camera system. The signals are labeled by frame number. The time interval between two adjacent frames is 30 ms. The frame counting starts when the image first appears.

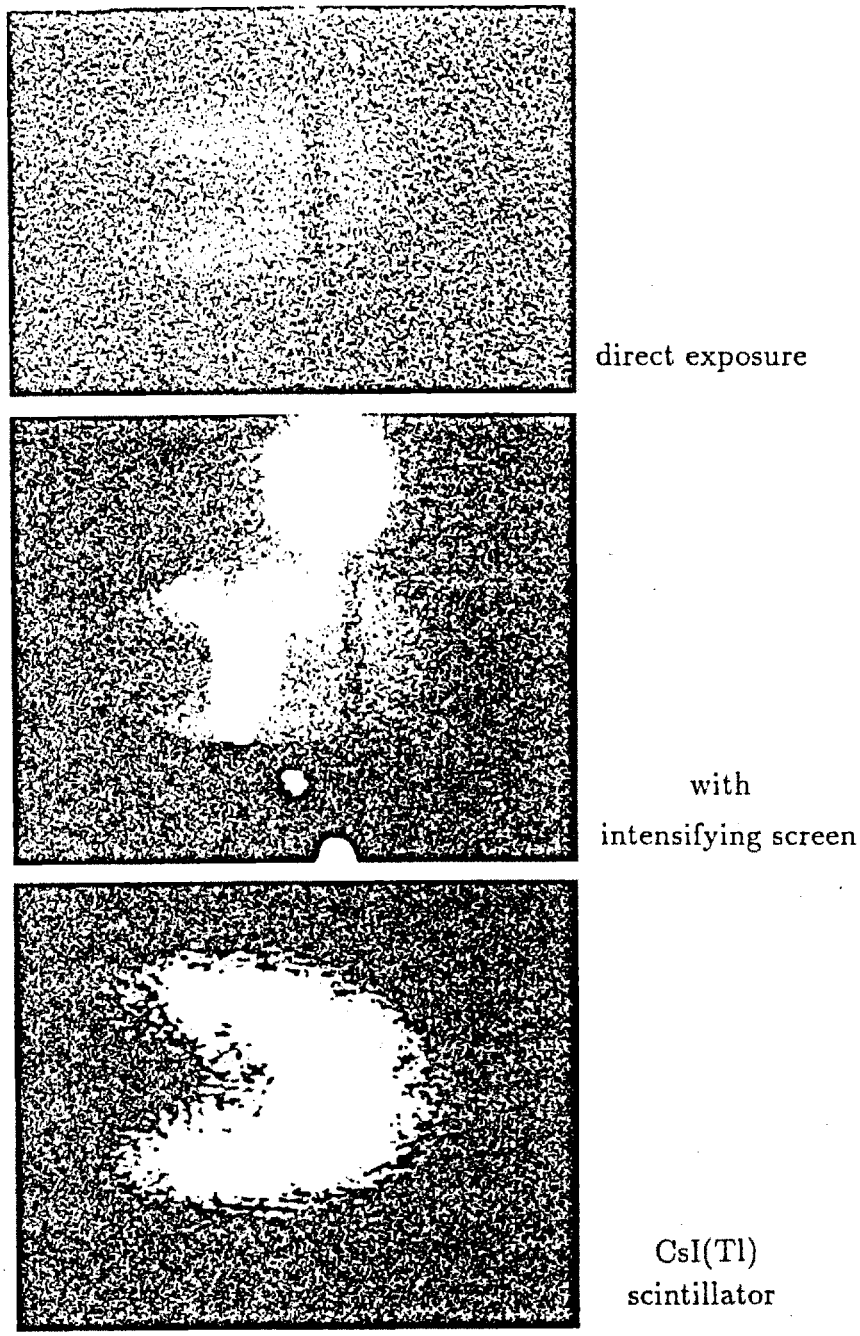

Figure 3.6: X-ray images of the plasma measured in three energy ranges. (a) 3 – 20 keV (direct exposure). (b) 50 – 200 keV (with intensifying screen). (c) 3 – 150 keV (CsI(Tl) scintillator). The vertical dark lines are the shadows of a diamagnetic loop in (a) and the ICRH antenna in (b). The bright spots are due to the target x-rays which are generated when the electrons hit the loop and the antenna.

relativistic ECRH resonant surface and there is a hollow region in its center. A hollow plasma in the shape of a baseball seam will produce these images. To confirm this interpretation, simulation of chord integrated model plasma profiles are compared with the camera pictures. Figure 3.7 shows the line integrations of two model plasma profiles in the Constance magnetic field. With the model profile which peaks on the axis (Fig. 3.7a), the image is always peaked since the line-of-sight is longest on the axis. If the plasma is sufficiently hollow (Fig. 3.7b), the image will be "C" shaped from the side view and four balls from the end view, as has been observed in the experiment. We will show in the next section that a deeply trapped, hollow plasma profile will naturally form a baseball seam in the Constance magnetic field.

The baseball seam plasma profile is also confirmed by skimmer probe measurements. Skimmer probes are inserted into the opening of the "C" to test for hot electrons. Figure 3.8 is a plot of the diamagnetic loop signal versus the skimmer probe radial position at $z = -10$ cm. It shows that the total plasma diamagnetism is barely perturbed even though the probe is well inside the ECRH resonance surface, which is nearly 9 cm at this axial location. However, during this scan, the probe is carefully kept on the horizontal symmetry plane. If the probe is 1 cm off the symmetry plane, no hot electrons can be generated.

Figure 3.9 shows the end loss power measured with a scintillator probe outside the mirror peak. During a steady state shot, the end loss power is equal to the RF power absorption since the end loss is much larger than the radial energy transport. The data shows that the ECRH power is absorbed mostly by the plasma off the magnetic axis. The radial positions of the end loss peaks correspond to a midplane radius of 10 cm, which is where the hot electron baseball seam is located. The on-axis dip of the end loss power profile is about 50 percent.

Combining these experimental observations, it is clear that the plasma is con-

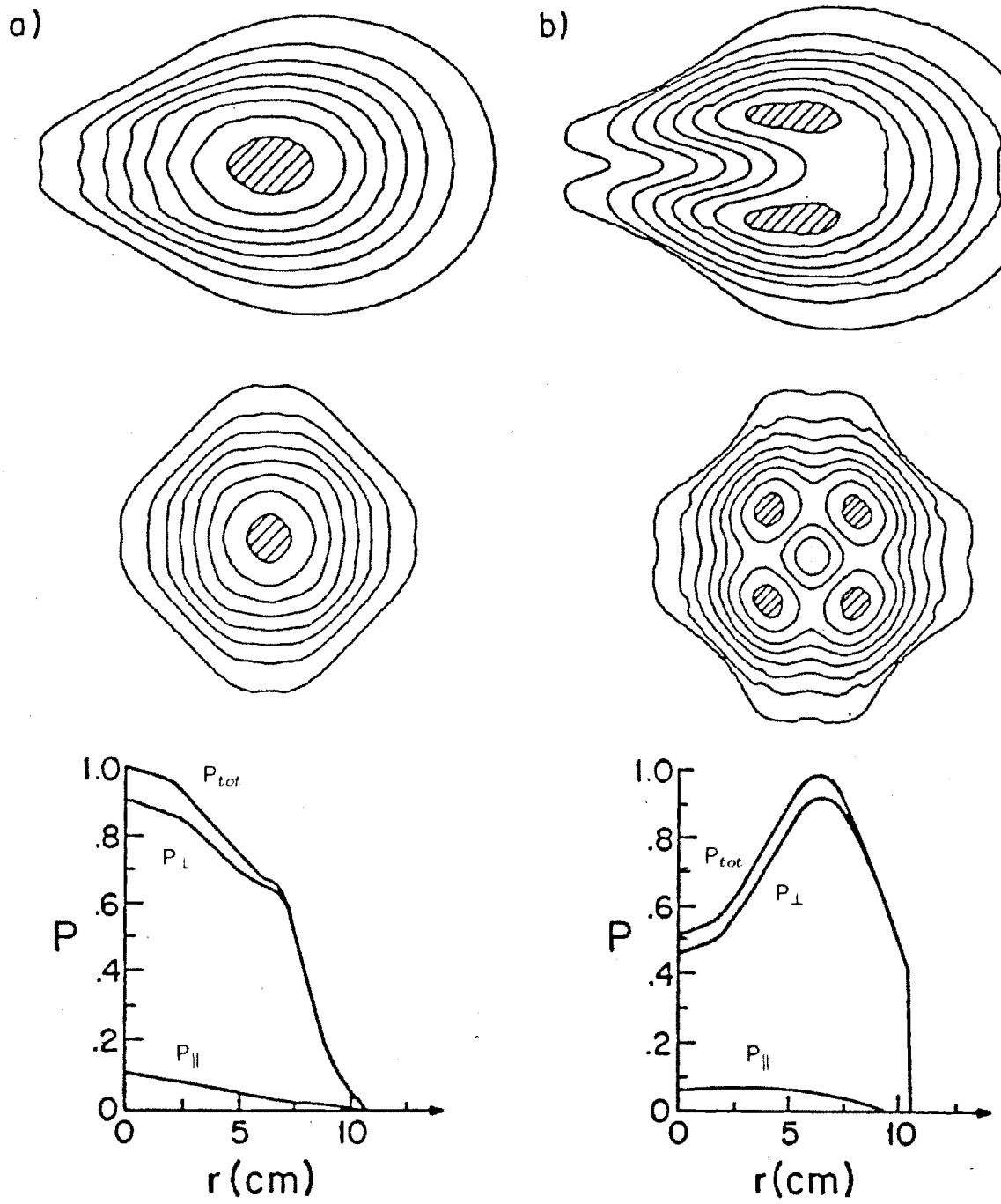

Figure 3.7: Line integrated model plasma pressure profiles. (a) A radially peaked profile. (b) A 50 percent hollow profile. The highest contours are shaded. The radial pressure profiles $P_\parallel$ (lower curve), $P_\perp$, and P_{tot} (higher curve) are plotted as function of radius along the 45° line at the midplane.

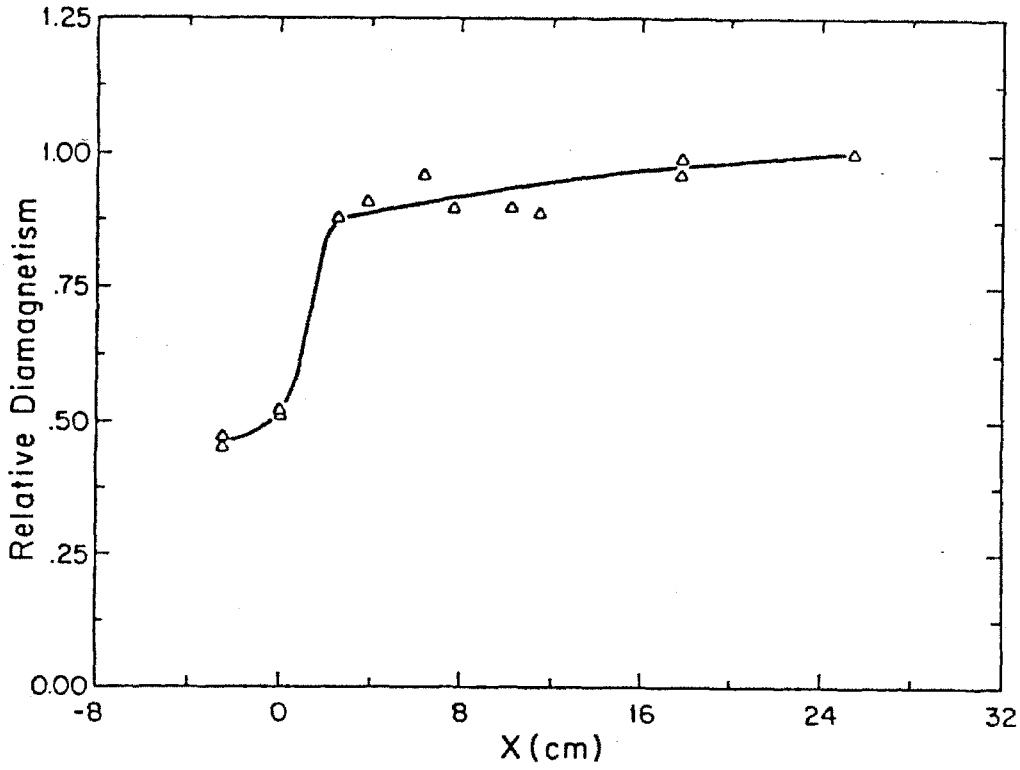

Figure 3.8: Relative diamagnetic signal measured during a skimmer probe radial scan in the horizontal symmetry plane at $z = -10$ cm. The solid line is a visual fit of the data points.

fined along a baseball seam curve. In order to quantitatively determine the plasma equilibrium pressure profile, a good pressure model is needed. We will analyze the equilibrium properties of quadrupole minimum-B mirrors to understand the equilibrium and to establish the plasma model.

3.3 Equilibrium in Quadrupole Mirrors

Plasma equilibrium is determined by the magnetic field geometry, the plasma heating profile and the source function, and by stability criteria. In the Constance B experiment, the equilibrium pressure profile is observed to be hollow and peaked along a baseball seam curve. In this section we will try to understand this equilibrium struc-

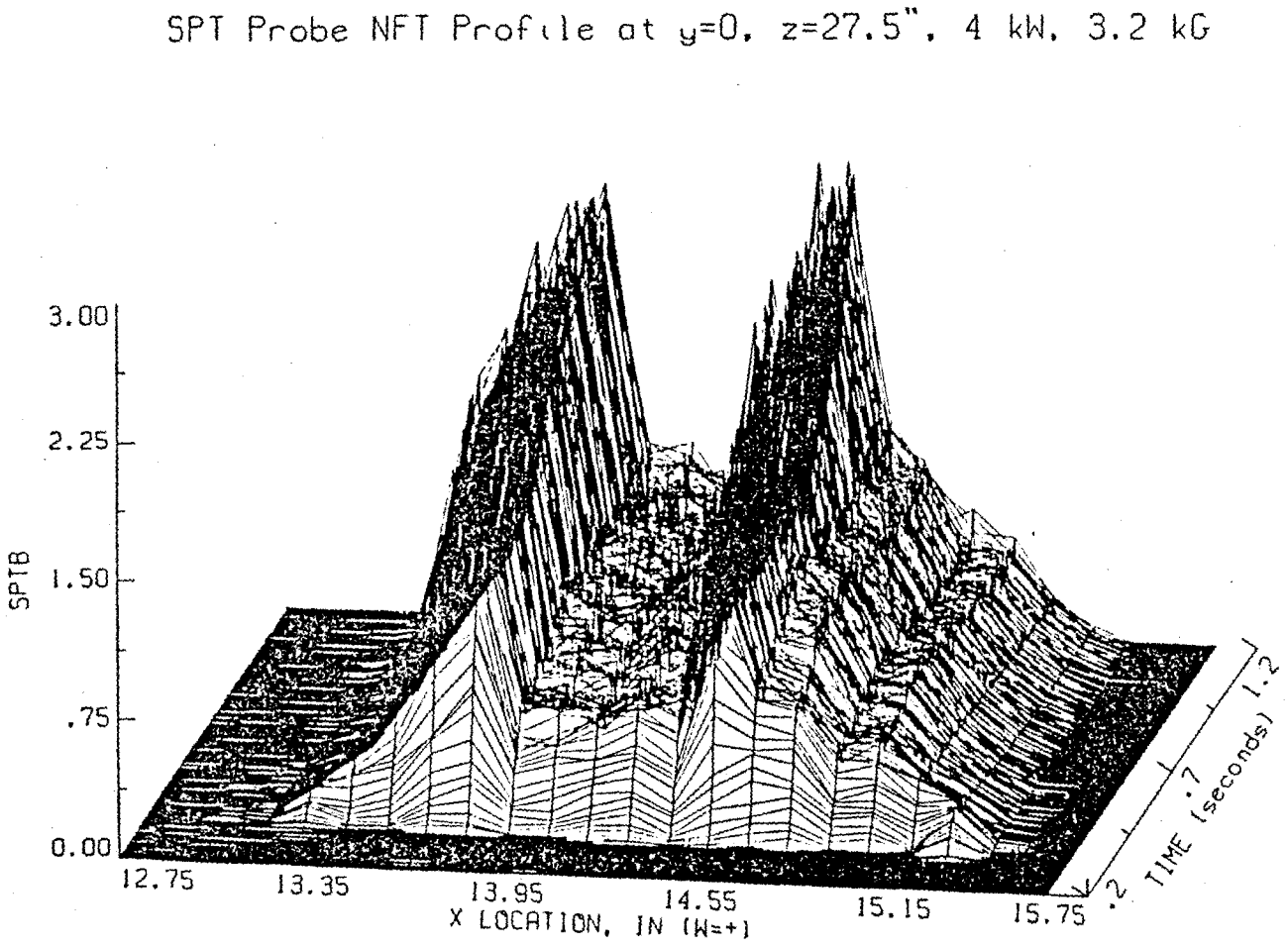

Figure 3.9: Radial end loss power profile measured in a scintillator probe scan outside the mirror peak ($z = -90$ cm). [1]

ture using both the single particle and fluid theory. A plasma pressure model based on this analysis will be developed in the next section for a quantitative determination of the equilibrium.

3.3.1 Single Particle Motion

Particle drift motion plays an important role in mirror confined plasma equilibria where the plasma confinement time is long compared with the particle drift time. It is well known that in the limit that the particle Larmor radius is small compared with characteristic magnetic scale lengths, the drift motion of a mirror confined particle is characterized by three adiabatic invariants, the total energy ϵ, the magnetic moment μ, and the longitudinal invariant J. Here

$$J = \oint v_{\parallel} dl.$$

In general, J is a function of magnetic flux lines and is dependent on the particle's energy and magnetic moment.

The effect of these adiabatic invariants is best illustrated from the particle orbit motion. The trajectory of a relativistic charged particle in a steady electromagnetic field is determined by

$$\frac{d\vec{p}}{dt} = q\,(\vec{E} + \vec{v} \times \vec{B}) \tag{3.1}$$

$$\frac{d\epsilon}{dt} = q\,\vec{v} \cdot \vec{E} \tag{3.2}$$

with $\vec{p} = \gamma m \vec{v}$, $\epsilon = \gamma m c^2$, and $\gamma = \frac{1}{\sqrt{1-(v/c)^2}}$ is the relativistic factor. A difference equation can be obtained using the approximations

$$\vec{v} = \frac{d\vec{x}}{dt} = \frac{\vec{x}_{n+1} - \vec{x}_{n-1}}{2\Delta t},$$

$$\frac{d\vec{v}}{dt} = \frac{\vec{x}_{n+1} - 2\vec{x}_n + \vec{x}_{n-1}}{(\Delta t)^2},$$

$$v_i v_j = \frac{1}{2}\left[\left(\frac{x_{i_{n+1}} - x_{i_n}}{\Delta t}\right)\left(\frac{x_{j_n} - x_{j_{n-1}}}{\Delta t}\right) + \left(\frac{x_{j_{n+1}} - x_{j_n}}{\Delta t}\right)\left(\frac{x_{i_n} - x_{i_{n-1}}}{\Delta t}\right)\right].$$

The equations of motion Eq. 3.1–3.2 can then be written as difference equations and traced numerically with computer. The final form of the difference equations is

$$\begin{pmatrix} 1 + \frac{1}{2c^2}(\vec{A}_n d\vec{x}_n + A_x dx_n) & \frac{1}{2c^2}A_y dx_n - \frac{1}{2}\omega_z \Delta t & \frac{1}{2c^2}A_z dx_n - \frac{1}{2}\omega_y \Delta t \\ \frac{1}{2c^2}A_x dy_n - \frac{1}{2}\omega_z \Delta t & 1 + \frac{1}{2c^2}(\vec{A}_n d\vec{x}_n + A_y dy_n) & \frac{1}{2c^2}A_z dy_n - \frac{1}{2}\omega_x \Delta t \\ \frac{1}{2c^2}A_x dz_n - \frac{1}{2}\omega_y \Delta t & \frac{1}{2c^2}A_y dz_n - \frac{1}{2}\omega_x \Delta t & 1 + \frac{1}{2c^2}(\vec{A}_n d\vec{x}_n + A_z dz_n) \end{pmatrix}$$

$$\cdot \begin{pmatrix} dx_{n+1} \\ dy_{n+1} \\ dz_{n+1} \end{pmatrix} = \begin{pmatrix} dx_n + A_x(\Delta t)^2 + \frac{1}{2}\omega_z \Delta t dy_n - \frac{1}{2}\omega_y \Delta t dz_n \\ dy_n + A_y(\Delta t)^2 + \frac{1}{2}\omega_x \Delta t dz_n - \frac{1}{2}\omega_z \Delta t dx_n \\ dz_n + A_z(\Delta t)^2 + \frac{1}{2}\omega_y \Delta t dx_n - \frac{1}{2}\omega_x \Delta t dy_n \end{pmatrix} \tag{3.3}$$

where

$$\vec{A} \equiv \frac{q}{m\gamma}\vec{E},$$

$$\vec{\omega} \equiv \frac{q}{m\gamma}\vec{B},$$

$$d\vec{x}_n \equiv \vec{x}_n - \vec{x}_{n-1}.$$

Figure 3.10(a) shows the trajectory of a 360 keV deeply trapped electron in the Constance B magnetic field calculated with Eq. 3.3. The electron orbit drifts across magnetic field lines along a baseball seam curve while bouncing back and forth in the axial direction. The drift frequency is about 5 MHz. The vacuum magnetic field is used in the calculation and only the guiding center positions are plotted. The time step for this calculation is 1 ps, which is about one hundredth of the time scale of the electron gyromotion. Note that this drift orbit is very similar to the plasma profile observed in the experiment. It is clear that as long as the plasma radial profile is hollow, a baseball seam plasma equilibrium will be produced.

On a time scale long compared with the bounce time, the particle is observed drifting on a nearly closed magnetic flux surface. Figure 3.10(b) is a puncture plot which shows the intersection of these flux lines with the midplane. It is a diamond shaped curve and shows the shape of constant J surfaces in a quadrupole magnetic field. The numerical calculations also show that these drift surfaces are only weakly

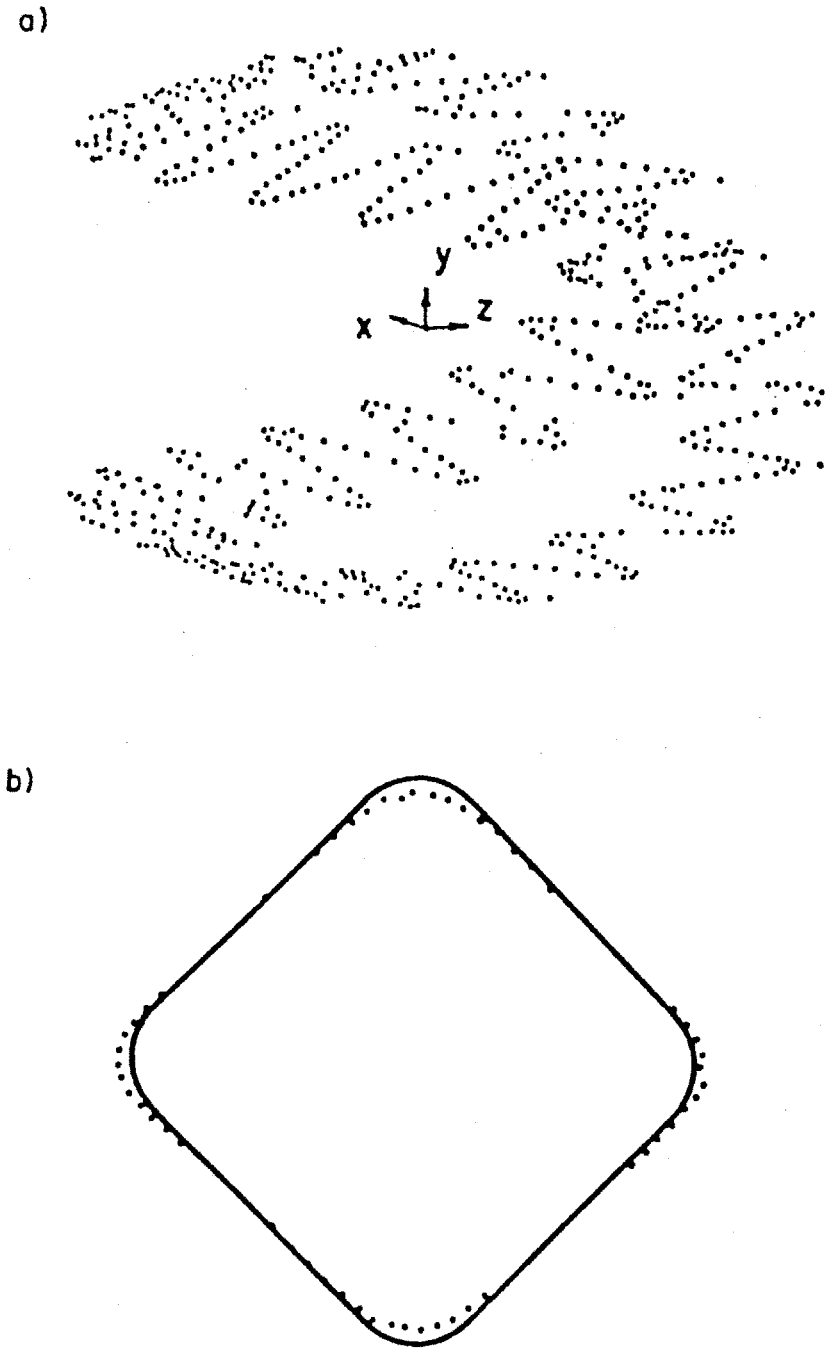

Figure 3.10: Calculated drift orbit of a 360 keV electron in the vacuum magnetic field. (a) Guiding center trajectory. (b) Drift surface. The drift surface is obtained by mapping the guiding center positions along flux lines back to the midplane.

dependent on the particle energy, pitch angle and mass. Thus we can label drift surfaces by a single constant J surface. Since particles with different energies drift at different azimuthal velocities, the plasmas on each drift surface have the same velocity distribution function for observations on a time scale long compared with the characteristic drift time. This has an important effect for the microinstabilities. When the plasma goes unstable, the instability will occur on a whole drift surface rather than a single field line.

In non-axisymmetric mirror fields, particles also drift in and out of a constant J surface due to the non-zero geodesic curvature. Figure 3.11 shows the drift surface of a shallowly trapped electron with a bounce length of 30 cm in Constance. It shows that the electron drifts in and out radially while bouncing along field lines. But the average radial drift is cancelled due to the bounce motion. Two consequences of this geodesic curvature drift should be noticed. First, if the device length is much longer than the radial scale length, a particle may drift a considerable azimuthal distance within one bounce motion. When the particle bounces back and forth on different field lines, the radial drift may not be completely cancelled and thus cause enhanced radial transport. The second effect of the geodesic curvature drift is to radially average the particle response to a perturbation in a way similar to the finite Larmor radius effect. This may lead to stabilization of curvature driven modes and will be discussed in Chapter 6.

3.3.2 ECRH Heating Profile

The plasma equilibrium profile is strongly dependent on the plasma source function and heating. For the ECRH plasma in Constance, plasma heating occurs on a resonant mod-B surface on which the electron cyclotron frequency is equal to the RF frequency. The ECRH heating rate is proportional to the applied RF electric field

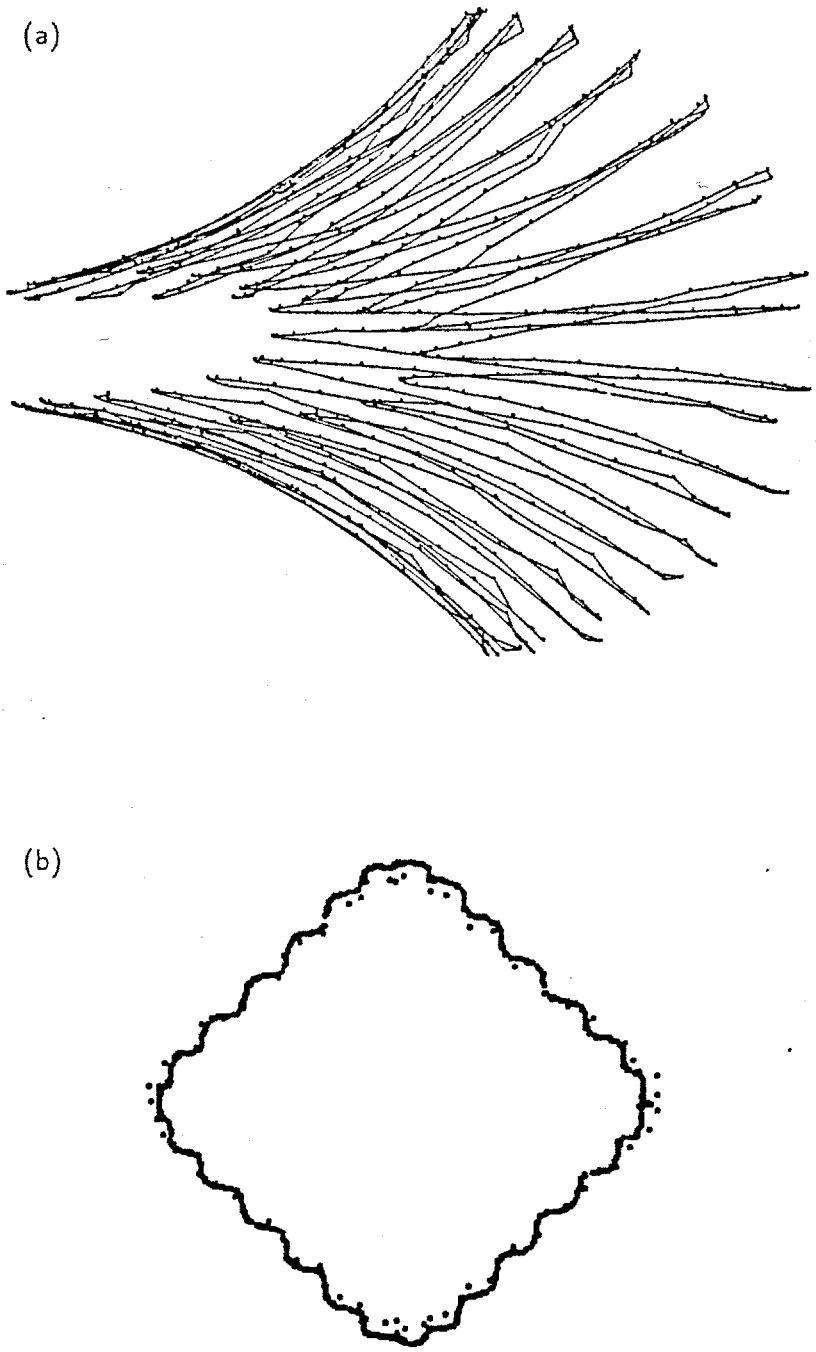

Figure 3.11: Guiding center trajectory and the drift surface of a shallowly trapped 360 keV electron. The bounce length for this electron is about 17 cm from the midplane.

and the time length that the electrons stay in resonance,

$$\frac{dT_e}{dt} \propto \frac{E^2}{\vec{b} \cdot \nabla B}.$$

Where E is the electric field strength of the RF wave and T_e is the electron energy. Given the magnetic field geometry, the strongest ECRH heating is expected to occur on the field lines which are tangent to the resonant surface. Figure 2.2 is a drawing indicating these tangent points in a quadrupole mirror field. It shows that the tangent points form a baseball seam curve on the resonant mod-B surface, which is similar to the drift orbit of the deeply trapped electrons. This results in a situation that an electron born at the drift surface will stay there for many drifts and keep getting heated. A hot electron layer will be formed as the particles accumulate unless it is prohibited by MHD or microinstabilities, or by some strong radial transport processes.

3.3.3 Fluid Description

The MHD equilibrium of a magnetically confined plasma is maintained by balancing the plasma pressure with the forces resulting from the interaction of the plasma current and the applied magnetic field. In a magnetic mirror, the equilibrium relation is described by the guiding center fluid equations.

$$\vec{J} \times \vec{B} = \nabla \cdot \mathbf{P} \tag{3.4}$$

$$\nabla \times \vec{B} = \mu_0 \vec{J} \tag{3.5}$$

$$\nabla \cdot \vec{B} = 0. \tag{3.6}$$

Here $\mathbf{P} = P_\perp \mathbf{I} + (P_\parallel - P_\perp)\vec{b}\vec{b}$ is the anisotropic plasma pressure tensor. From these equations, the self-consistent magnetic field $\vec{B}$ can be determined when the plasma pressure and the boundary conditions are known. The plasma pressure tensor itself, however, is a free function in the equations. It will be determined from the experimental measurements.

The force along a magnetic field line is balanced within the plasma pressure tensor itself. It requires

$$P_\perp = P_\parallel - B\frac{\partial P_\parallel}{\partial B}, \tag{3.7}$$

where the derivative of $P_\parallel$ is taken along a magnetic field line. With this relation, there is only one pressure function left to be determined from experiment.

Perpendicular to the magnetic field lines, the force balance can be written as

$$\nabla_\perp(\frac{B^2}{2\mu_0} + P_\perp) = (\frac{B^2}{\mu_0} + P_\perp - P_\parallel)\vec{\kappa}, \tag{3.8}$$

where $\vec{\kappa} = (\vec{b}\cdot\nabla)\vec{b}$ is the magnetic field line curvature. Considering the equation in the $\vec{b}$, $\vec{\kappa}$ and $\vec{b}\times\vec{\kappa}$ directions, we see that $(\frac{B^2}{2\mu_0} + P_\perp)$ is constant in the $\vec{b}\times\vec{\kappa}$ direction. When the vector $\vec{b}\times\vec{\kappa}$ forms a closed flux surface, the plasma pressure profile will be a function of the magnetic field magnitude B and a single flux surface parameter. We need to evaluate the magnetic field geometry to determine this flux surface parameter.

In the low beta limit, the $\vec{b}\times\vec{\kappa}$ direction evaluated at the minimum of B corresponds to the drift orbit of particles deeply trapped near the magnetic minimum on each field line. This follows from the relation

$$\vec{\kappa} = (\nabla_\perp B + \mu_0\vec{J}\times\vec{b})/B.$$

When the plasma current density is small due to low beta, $\vec{\kappa}$ is parallel to $\nabla_\perp B$. Thus, a surface constructed by connecting all the flux lines which have the same minimum magnetic field value will correspond to the drift surface for a deeply trapped particle. We label such a surface as a constant J_* surface. The value of J_* is defined to be equal to the radius of the flux surface at 45 degrees at the midplane. The minimum B points on a constant J_* surface will form a baseball seam curve on a mod-B surface. It is easy to see that a deeply trapped plasma profile will peak along the magnetic field lines at these minimum B points. Therefore, as long as its radial profile is hollow, a baseball seam plasma will be formed.

In a finite beta plasma equilibrium, the magnetic field will be modified by the plasma current. The $\vec{b} \times \vec{\kappa}$ direction is then dependent on the plasma pressure profile and beta. However, it can still be shown that there exists a closed flux surface which is connected by the $\vec{b} \times \vec{\kappa}$ vector near the magnetic minimum on those field lines. Also, it has been observed in numerical equilibrium calculations that the change of $\vec{\kappa}$ and $\vec{b}$ is usually small compared with the change of ∇B [Anderson, 1985].

Based on this understanding, we assume that the plasma pressure has a functional structure $P_{\|,\perp} = P_{\|,\perp}(B, J_*)$, with J_* a constant on a vacuum field constant J surface. The use of $\vec{b} \times \vec{\kappa}$ near the magnetic minimum to determine the flux surface is justified by the fact that the plasma pressure profile has been experimentally observed to be very anisotropic and deeply trapped. We will now develop an equilibrium pressure model so that the experimental measurements can be quantitatively analyzed.

3.4 Equilibrium Model

Based on the equilibrium properties discussed above, the plasma pressure profile in Constance B can be assumed to be of the form P=P(B, J_*). To reduce the parameter space for equilibrium modelling, we further assume that the pressure can be expressed as separable functions, $P_\perp(B, J_*) = P_1(B) \cdot P_2(J_*)$.

The function P_1 is taken to be

$$P_1(B) = \frac{nB^2(B_{max} - B)^{n-1}}{1 + e^{k(B-B_h)}}.$$

Where n and k are the numerical parameters which can be varied to obtain different profiles. This expression modifies Taylor's expression [Taylor, 1963] with a Fermi distribution function so that the pressure cutoff at the ECRH resonant mod-B surface can be modeled. In the expression, B_h is the one half cutoff point in the Fermi distribution function and is expected to be close to the ECRH resonant magnetic field. B_{max} is still the maximum magnetic field at the mirror peak. The parallel

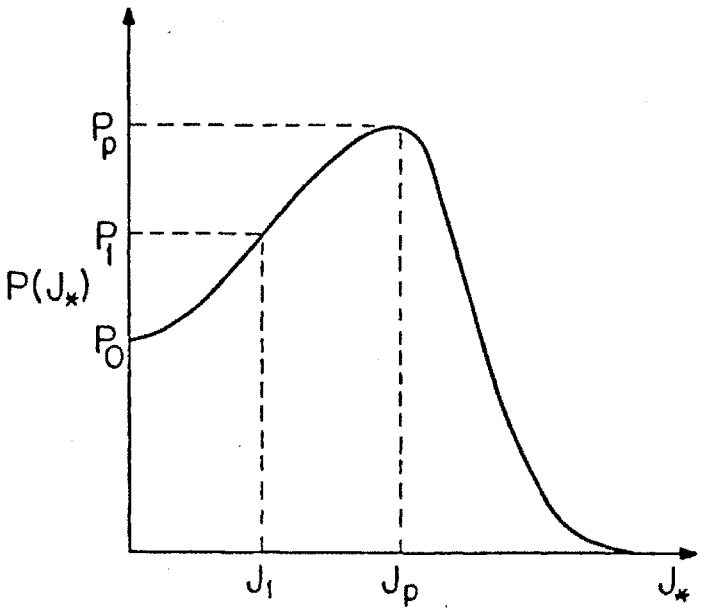

Figure 3.12: Radial pressure profile model.

component of the pressure tensor, $P_{||}$, is calculated from $P_{\perp}$ through the parallel force balance equation (Eq. 3.7).

For P_2 we take

$$P_2(J_*) = \frac{1}{P_1[B_0(J_*)]} \times \begin{cases} p_0 + \sum_{n=2}^{4} a_n J_*^n & \text{if } J_* \leq J_p \\ \\ p_p e^{-c_1(J_* - J_p)^2} & \text{if } J_* > J_p \end{cases}$$

Here $B_0(J_*)$ is the minimum magnetic field on the drift surface J_*. The radial profile is determined by the functions apart from $\frac{1}{P_1[B_0(J_*)]}$, which is used to cancel the radial variation of $P_1(B)$. Inside the peak pressure point J_p (see Fig. 3.12), the profile is chosen so that $P_2(J_*) = p_0$, p_1, p_p at $J_* = 0$, J_1, J_p, respectively. Outside J_p, a Gaussian function is used. We define the "hollowness" of the plasma to be $(p_p - p_0)/p_p$. The quantities p_0, p_1, p_p and J_1, J_p, c_1 are input parameters and the coefficients a_2 to a_4 are obtained with a linear equation solver which fits all the points and forces the slope at J_p to be zero. When the model is used to simulate the hot electron density profile in analyzing the plasma visible light and x-ray images, we cut off the plasma

beyond the constant J_* surface on which $B_0(J_*)$ equals the resonant magnetic field so that the sharp plasma edge there can be modelled.

With the pressure profile model, the plasma equilibrium can be quantitatively analyzed by comparing the predictions from the model with the measurements. The simulated plasma images shown in Fig. 3.7 are generated by integrating the model plasma profile along the line-of-sight of the camera. The profile parameters for the two models are

$n = 5, k = 10., B_h = 1.15; p_0 = 1.4, p_1 = 1.2, p_p = 1., j_1 = 0.037, j_p = 0.064, c_1 = 2000,$

and

$n = 5, k = 10., B_h = 1.2; p_0 = 0.5, p_1 = 0.75, p_p = 1., j_1 = 0.037, j_p = 0.064, c_1 = 500,$

respectively.

3.4.1 Properties of the Model

Several limitations of the plasma pressure model should be noticed.

(1) The assumption that the plasma pressure can be expressed as a separable function $P_\perp(B, J_*) = P_1(B) \cdot P_2(J_*)$ corresponds to the situation where the particle distribution function, apart from an overall weighting function, is the same on all field lines. We know that the distribution functions are the same only on a drift surface. At different radii they are not necessarily the same. The reason for using separable functions is to simplify the analysis, and its usage is justified by the fact that the experimental observations can be closely modelled with this plasma pressure function.

(2) The functional form of the pressure model $P = P(B, J_*)$ can be applied to both the plasma pressure and the density profile because the equilibrium plasma distribution function is the same on a drift surface. However, the density can be very different from the pressure profile because the plasma temperature and the temperature anisotropy may vary with radius.

(3) There are eight profile parameters in the pressure model. Because the parameters are involved with complicated functions, it is difficult to perform a regression to determine the parameters individually. Instead we look at the plasma profile as a whole and determine the best fit model by comparing the residues between one model and another. The resulted 10 percent accuracy of the plasma profile determination is sufficient compared with the uncertainties in the equilibrium measurement and the theoretical analysis.

Even through this plasma model may seem very restrictive, because it contains both the physics feature of the plasma equilibrium and the confining magnetic geometry, a large variety of plasma pressure profiles needed for the equilibrium analysis can be modelled.

Chapter 4

Experimental Equilibrium Determination

In the last chapter, the plasma equilibrium structure has been qualitatively presented and analyzed. An equilibrium pressure model was developed through which the experimental data will be interpreted. This chapter presents and analyzes the experimental data from four independent measurements: visible light imaging, x-ray imaging, magnetic measurements and skimmer-thermocouple probe measurements. We will first determine the plasma equilibrium in the standard experimental condition (B_0 = 3 kG, ECRH power = 2 kW, hydrogen gas pressure = 5×10^{-7} torr), and then analyze the equilibria under different experimental conditions.

4.1 Visible Light Images

4.1.1 Visible Light Emission from a Plasma

In a plasma, visible light radiation is emitted when an electron makes a transition in the field of an atom or ion. The three main transition processes are electron excitation, recombination, and bremsstrahlung radiation (free-free transitions). In a low density plasma, electron excitation is the predominant light source.

The line emission intensity of an optically thin plasma for a particular transition

is given by

$$I(p,q) = \frac{1}{4\pi}\int n_z(p)A(p,q)h\nu dl, \tag{4.1}$$

where $A(p,q)$ is the transition probability between bound states p and q, Z denotes the charge state of the ion, and the integration is taken over the line of sight of the detector. We can use the corona model to describe the Constance plasma whose density is on the order of a few times 10^{11} cm^{-3}. Assuming the excited atomic population is determined by electron excitation and spontaneous radiative decay, we have the relations for a hydrogen plasma

$$n_e n_0(g)X(T_e,g,p) = n_0(p)\sum_q A(p,q) \qquad (q<p), \tag{4.2}$$

where $X(T_e,g,p) \equiv$ electron excitation coefficient from ground state g to state p. The use of ground state in Eq. (4.2) is justified by the fact that the plasma collisional time scale (10^{-6} sec) is two orders of magnitude longer than the time scale of atomic transitions. The total line radiation intensity from the hydrogen plasma is then

$$I = \sum I(p,q) = \frac{1}{4\pi}\int n_e n_0(g)\sum X(T_e,g,p)\frac{A(p,q)}{\sum_{r<p}A(p,r)}h\nu(p,q)dl. \tag{4.3}$$

Besides the hydrogen lines there are some impurity lines in the plasma. The strongest impurity line is the Carbon III line (4650 Å). However, the intensity of this line is less than 5 % of the H_α line (6562 Å).

The continuous radiation is produced through the free-bound and free-free transitions. For a non-relativistic Maxwellian electron distribution, the radiation intensities of the two processes are given by [Podgornyi, 1971]

$$I_{fb}d\nu = \frac{1}{4\pi}\int dl A_{fb}n_e n_i\left(\frac{E_H}{T_e}\right)^{3/2}\left(\frac{E_n}{E_H}\right)^2\frac{g_{fb}}{n}\xi_n\exp(\frac{E_n-h\nu}{T_e})d\nu, \tag{4.4}$$

$$I_{ff}d\nu = \frac{1}{4\pi}\int dl A_{ff}Z^2 n_e n_i\left(\frac{E_H}{T_e}\right)^{1/2}\exp(\frac{-h\nu}{T_e})g_{ff}d\nu, \tag{4.5}$$

where $E_H = 13.6$ eV, E_n is the ionization energy for the shell for which the principal quantum number is n, ξ_n is the number of vacant sites in the n shell, and g_{fb} and g_{ff}

are the Gaunt coefficients. The numerical factors A_{fb} and A_{ff} are both 7×10^{-40} erg ·cm^3. Notice that the radiation intensities of the two continuous radiation processes are proportional to $(n_e n_i)$. However, the intensity of the continuum in the visible range is observed to be on the order of a few percent of the line radiations.

The visible light image of the plasma is measured with a CCD TV camera system which is sensitive to the spectral range from 4000 to 10,000 Å. During the ECRH pulse, both the cold and the hot electron plasma densities are on the same order of magnitude and the visible light emission is dominated by the cold electrons. After the RF is turned off, the plasma becomes an almost completely hot electron plasma within a few hundred microseconds. The cold electrons are scattered into the loss cone on a time scale of 50 μs, while the hot electron confinement time is about 2 seconds. The population of the cold electrons generated by hot electron ionization of the background gas is on the order of $n_{ec}/n_{eh} \sim 10^{-3}$.

The absolute values of the transition coefficients are given by atomic physics but their accuracy is normally only about 50 %. However, a better job can be done when we just want to determine the relative spatial intensity. Figure 4.1 shows the electron ionization rate as a function of electron temperature in a hydrogen gas. In the temperature range we are interested in, 100 – 500 keV, the ionization rate is flat to within 5 percent. The electron excitation rate should have the same energy dependence as the ionization rate when $T_e \gg E_H$, because both processes are through Coulomb interactions and the quantum effect becomes less important when the electron energy is much larger than E_H. The ionization rate of the 400 keV electrons is 10 times lower than that of the 100 eV electrons, but the ratio of the hot to cold densities is about 10^3 in the afterglow. Therefore visible light radiation is proportional to $n_{eh} n_0(g)$. The neutral target density $n_0(g)$ in the afterglow is spatially uniform. The mean free path of the neutrals in the afterglow plasma is about 50 cm, which is five times the

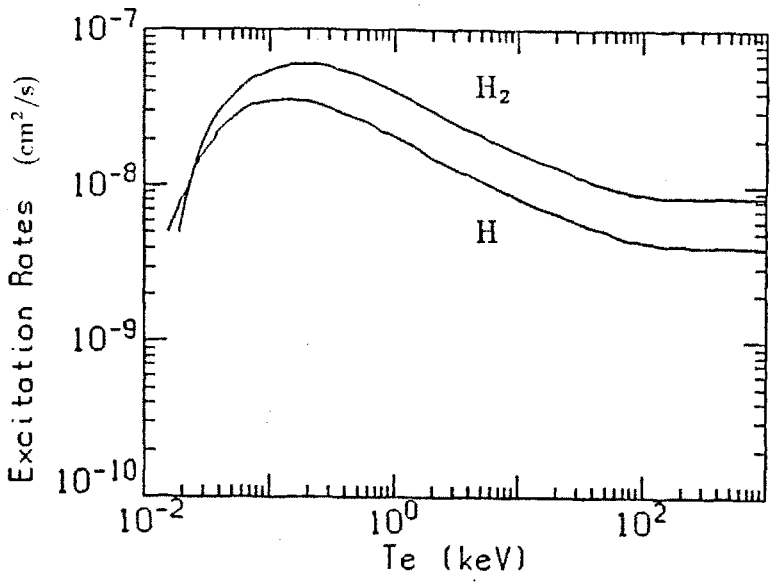

Figure 4.1: Theoretical electron ionization rates of atomic and molecular hydrogen. (Data from [Barnett, 1977])

plasma radius. Thus the images after the ECRH is turned off are used for the hot electron density profile analysis.

4.1.2 Hot Electron Density Profile

The hot electron density profile is obtained by analyzing the plasma visible light images immediately after the ECRH power is turned off. A plasma visible light image taken at 60 ms after the ECRH turn-off is shown in Fig. 4.2. Since the plasma cross section is not circular, the model equilibrium profiles are integrated numerically along the line-of-sight of the camera for comparison with the measured plasma images. A quantitative comparison is done by taking film density traces from the photographs. Figure 4.2(b) and (c) show the film density traces measured from the photograph. The simulated line integrations of the 50 % hollow hot electron density profile (Fig. 3.7) are plotted in dashed lines. Because the plasma hollowness is a parameter which is important for the stability analysis, we vary the hollowness to see the sensitivity of this comparison. The dotted lines plotted with the film density traces are the line

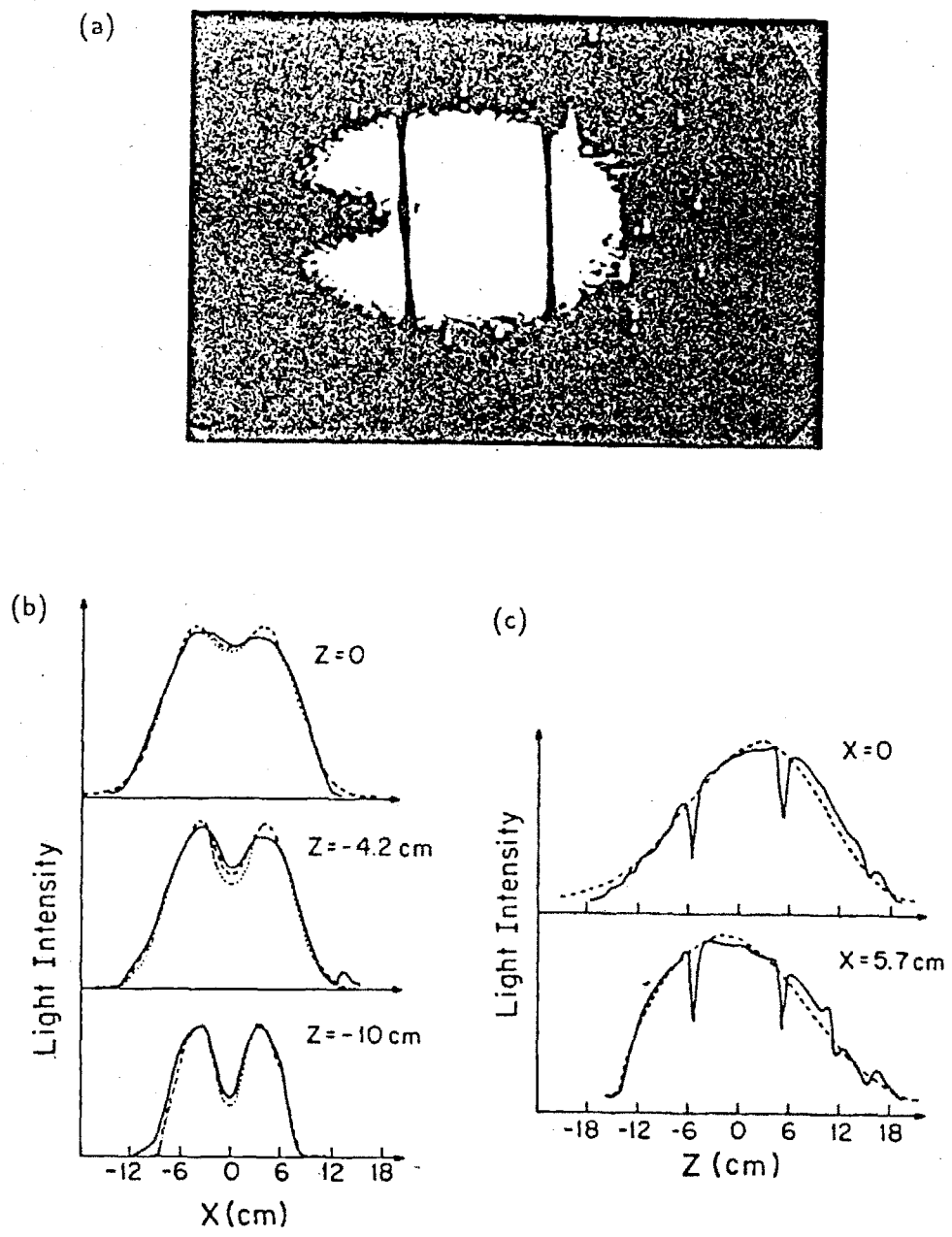

Figure 4.2: Comparison between the measured and the simulated visible light intensity traces. (a) A visible light photograph taken 60 ms after the ECRH turn-off. (b) Radial light intensity traces at three axial locations. (c) Intensity traces parallel to the axis. The solid lines are the light intensity traces measured from the photograph. The dashed lines are the simulations using a 50 percent hollow plasma density profile. The dotted lines are the simulations from a 60 percent hollow profile to show the sensitivity of the analysis to the hollowness parameter.

integrations from a 60 % hollow profile. The difference between the two modelled profiles is that p_0 is changed from 0.5 to 0.4 and p_1 from 0.75 to 0.7 (see Fig. 3.12). The plasma profile outside the peak density location is exactly the same. Note that this 10 percent difference in the hollowness can be distinguished. The midplane radial density profile of the 50 % hollow plasma model is shown in Fig. 4.10(a). It shows that the plasma density boundary has a sharp cut-off at the magnetic flux surface which has a midplane radius of 10.5 cm at 45 degrees. This radius corresponds to the magnetic flux surface on which the non-relativistic ECRH resonance just occurs.

The axial plasma profiles are analyzed by taking density traces parallel to the magnetic axis. Figure 4.2(c) shows the density traces of the plasma image at two radial locations (x=0, 5.7 cm). The dashed lines are from the line integral of the 50 % hollow model. The corresponding axial density profile is shown in Fig. 4.10(b).

From the visible light image measurement, we conclude that the best fit hot electron density profile is the one whose on-axis dip is 50 %, with an error bar of $\pm 10\%$. The plasma boundary is determined by the non-relativistic ECRH resonance. The errors involved in this analysis mainly come from the hot electron temperature non-uniformity and the camera viewing angle. The line-of-sight from the plasma edge to the camera is 12 degrees with respect to the x-axis. The error induced is within 3 percent. The error due to the temperature non-uniformity is within 5 percent in the hot electron temperature range, which is between 100 – 500 keV. The impurity lines and the continuous radiation have similar spatial profiles as the hydrogen lines and the induced error is estimated to be within a few percent.

4.2 X-ray Imaging

4.2.1 X-ray Emission from a Plasma

The two main processes of x-ray production in a plasma are:

(1) bremsstrahlung produced by the interaction of an electron with an ion, an atom, or another electron;

(2) recombination radiation produced by radiative capture of an electron by an ion.

The radiation intensities for bremsstrahlung and recombination processes in the non-relativistic limit were given in Eq.'s (4.4) and (4.5). Since the x-ray emission due to bremsstrahlung radiation exceeds the recombination processes at about $T_e \geq 3Z^2 E_H$, bremsstrahlung radiation is the dominant x-ray source in a hot electron plasma.

The spatial x-ray radiation profile is proportional to the hot electron density times the target density, with a profile factor determined by the plasma temperature profile. The target density is contributed by all the electrons, ions, and atoms. For a low Z, high temperature plasma both the electron-ion and the electron-electron bremsstrahlung must be considered. The electron-electron process becomes increasingly important with the increase of electron temperature and the x-ray photon energies. The ratio of the bremsstrahlung loss rates for electron-electron and electron-ion emission reaches about one at $T_e \simeq 200$ keV in a hydrogen plasma, and it becomes two at the extreme relativistic limit [Haug, 1975]. When the energy of an electron is sufficiently large, the ionization state of target ions is no longer important. The radiation from electron-atom collisions is identical to that from electron-ion collisions for x-rays with energy well above the atomic ionization potential. The densities of impurity targets in Constance were determined from their characteristic K lines measured by a Germanium detector in the energy range 2 – 10 keV. It was found that the dominant impurity targets were argon and titanium, and that the impurities contributed about 20-30 % of the total x-ray flux. Because the neutral gas density is

usually 20 times lower than the plasma density, the remaining 70 % of the x-rays is mostly from the hydrogen ion and electron targets. The impurity target profile also have a baseball seam profile similar to the hot electrons.

The radial and axial hot electron temperature profiles were measured by Hokin in a NaI(Tl) detector scan with ECRH power at 1 kW. The line integrated hot electron perpendicular temperature is observed to vary both radially and axially, as shown in Fig. 4.3. From the axial temperature variation, it is estimated that the temperature anisotropy at the magnetic midplane is on the order of $T_{e,\perp} : T_{e,\parallel} = 5 : 1$. In the radial direction, the x-ray temperature varies from 350 keV near the magnetic axis to 60 keV at the plasma edge. Unfortunately, the radial scan is conducted at $z = -3.2$ cm which is at the flat region of the "C" shaped plasma. Combined with the difficulties related to unfolding a spectrum in a non-axisymmetric geometry and the limited data points, detailed radial temperature data has not been obtained. But we expect the hot electron temperature profile has a baseball seam structure similar to the hot electron density profile because of the ECRH heating and the magnetic geometry.

4.2.2 Experimental Results

X-ray pinhole photographs are measured in three energy ranges because of the use of different exposure methods. The photographs obtained with the direct exposure method are sensitive mainly to photons with energy below 20 – 30 keV. Even though the x-ray film responds to photons up to several MeV, the measurements in which the film was covered with foils of various thickness show that the exposure is mostly done by the low energy x-rays, which is expected because of the few μm thickness of the film. The images of hard x-rays are measured by using intensifying screens, which are sensitive in the energy range 50 – 200 keV. For the time resolved x-ray imaging, the sensitive energy range is 3 – 150 keV, where the lower limit is determined by the beryllium x-ray window and the higher limit is determined by the absorption

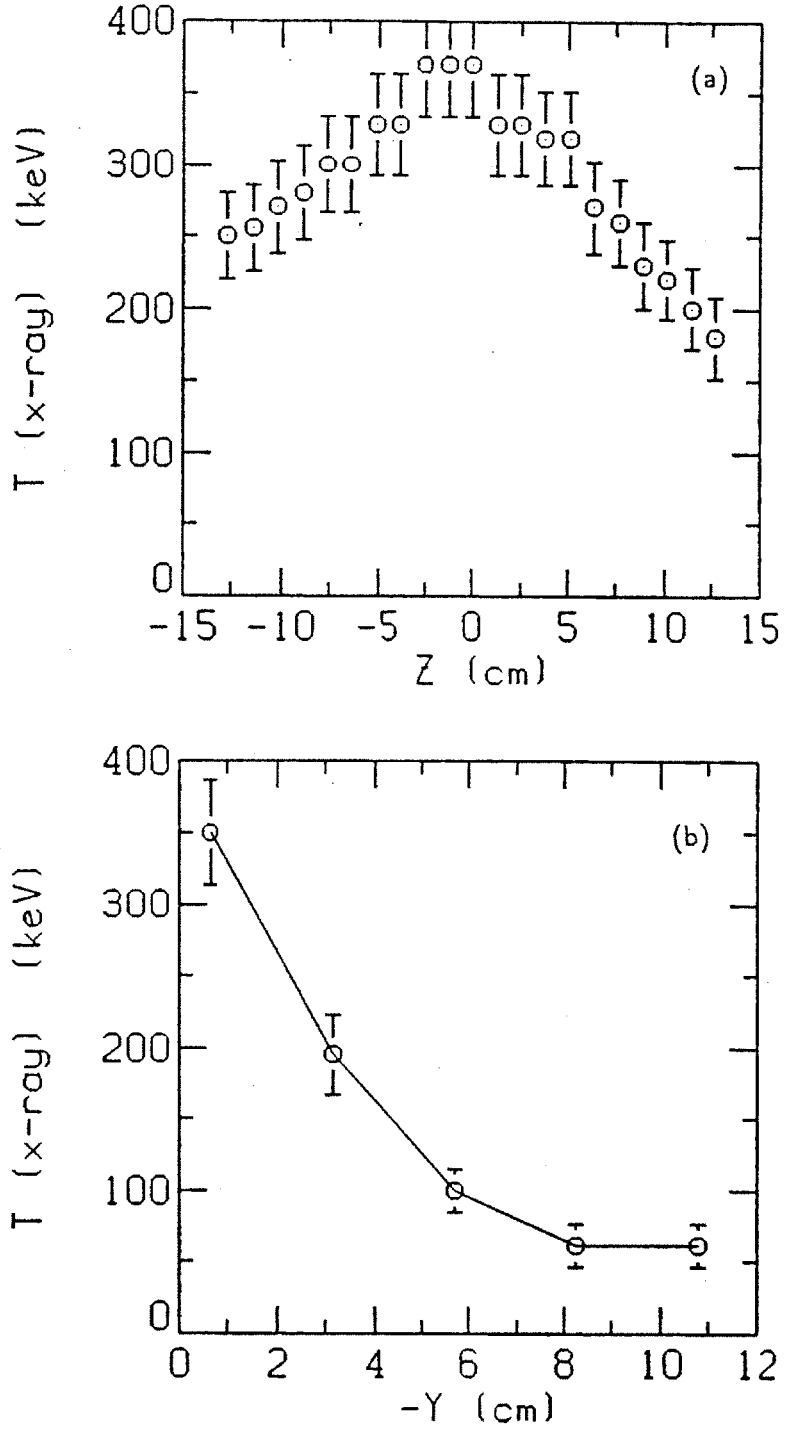

Figure 4.3: Line averaged radial and axial x-ray temperature profile measured by a NaI(Tl) detector. (Data taken by Sam Hokin.)

efficiency of the 2 mm thick CsI(Tl) crystal scintillator. However, the x-ray images measured at different energy ranges are similar, as were shown in Fig. 3.6.

The x-ray images are normally measured during the ECRH pulse. The measured x-ray intensities are approximately proportional to the hot electron density times the total plasma density, with a profile factor determined by the hot electron temperature profile. Because the cold electron density is less hollow than the hot electron's during this time, the total density profile is somewhere between the cold and hot electron profile. To make a quantitative analysis we assume the x-ray radiation intensity is proportional to n_{eh}^{δ}, with a δ value between 1.5 and 2. Here, $\delta = 2$ corresponds to the situation that the hot electron and the cold electron profiles are the same, and $\delta = 1.5$ corresponds to a nearly flat cold electron density profile. Since the x-ray images are only weakly dependent on measured energy ranges, no further temperature dependence is assumed.

Figure 4.4(a) is an x-ray pinhole picture obtained with the direct exposure method. The film density traces are shown in Fig. 4.4(b), together with two simulated density traces using the two radiation profile models. With $\delta = 1.5$, the best fit plasma profile is a 60 percent hollow profile with parameters
$n = 7, k = 10., B_h = 1.18; p_0 = 0.4, p_1 = 0.7, p_p = 1., j_1 = 0.035, j_p = 0.064, c_1 = 900.$
With $\delta = 2$, the best fit profile is the one whose on axis dip is 50 percent with
$n = 6.2, k = 10., B_h = 1.19; p_0 = 0.5, p_1 = 0.75, p_p = 1., j_1 = 0.035, j_p = 0.064, c_1 = 600.$

The radial distributions of these two plasma profiles at 45 degrees at the magnetic midplane are plotted in Fig. 4.10(a), together with the hot electron density profile determined from the visible light photographs. Both the x-ray and the visible light images show that the hot electron density is peaked at $J_* = 6.4$ cm, and the hollowness of the profile is about 50 percent. The difference between these three curves is less

(a)

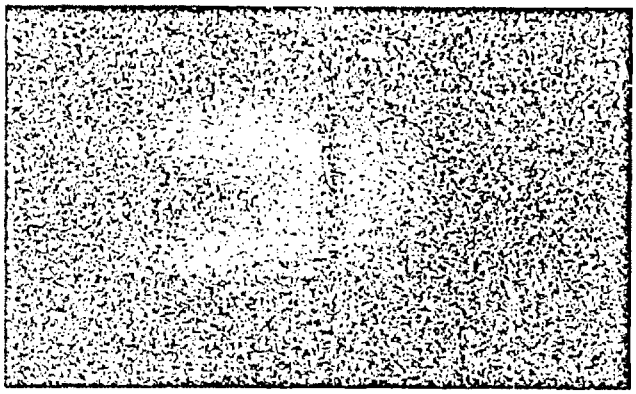

(b)

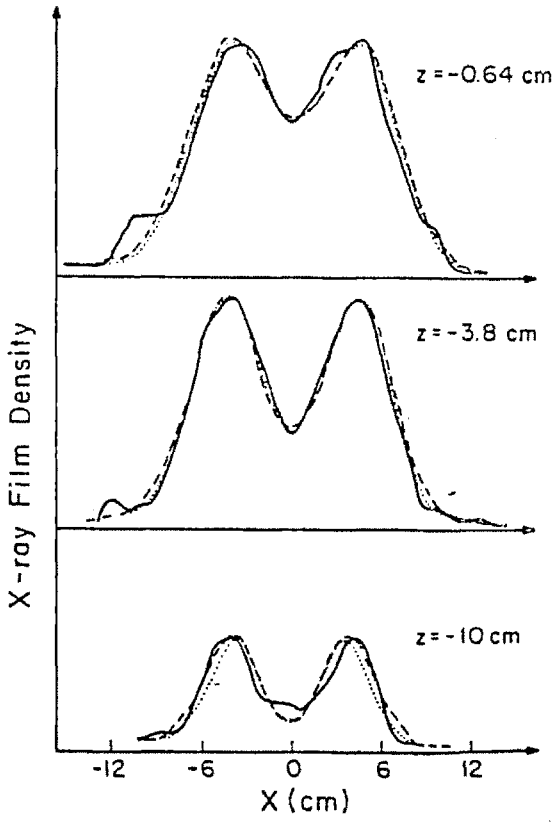

Figure 4.4: (a) An x-ray image of the plasma measured with the direct exposure method. (b) Comparison between the measured and the calculated x-ray intensity traces. The solid lines are the density traces measured from the x-ray film. The dashed and the dotted lines are from the best fit profiles for the n_{eh}^2 and the $n_{eh}^{3/2}$ models.

than 10 percent, with is in very good agreement considering the uncertainties in the x-ray imaging analysis, such as impurity profile and hot electron temperature profile effects.

4.3 Magnetic Measurements

Extensive magnetic measurements have been done to determine the plasma pressure profile. The plasma magnetic field is measured with diamagnetic loops and magnetic probes. Ratios between these magnetic signals are used in the equilibrium determination since they are independent of the total stored energy.

4.3.1 Plasma Diamagnetism Calculation

The plasma magnetic field is determined by the equilibrium relations Eq. (3.4–3.6). Because of the nonlinear nature of the equations and the complicated magnetic geometry involved, two approximations are used in the analysis:

(1) In a mirror confined plasma, the perpendicular (relative to $\vec{b}$) electric current density can be calculated from the force balance equation

$$\vec{J_\perp} = \frac{\vec{B} \times [\nabla_\perp P_\perp + (P_\parallel - P_\perp)\vec{\kappa}]}{B^2}. \tag{4.6}$$

If the system is non-axisymmetric, there is a current flow along magnetic field lines when $\nabla \cdot \vec{J} = 0$ cannot be satisfied by $\vec{J_\perp}$ alone. This condition can be expressed as

$$\vec{b} \cdot \nabla \left[\left(1 + \frac{\mu_0 (P_\perp - P_\parallel)}{B^2} \right) \frac{J_\parallel}{B} \right] + \frac{\vec{b} \times \vec{\kappa}}{B^2} \cdot \nabla (P_\perp + P_\parallel) = 0. \tag{4.7}$$

The equation shows that parallel currents exist whenever there is a non-zero pressure gradient along the $\vec{b} \times \vec{\kappa}$ direction. This current does not play a role in balancing the equilibrium forces but it simply flows along field lines to avoid charge accumulation. At the mirror throats this current has to be close to zero for a confined plasma. In a long device the parallel current can produce a magnetic field perpendicular to the

vacuum field which may lead field lines to leave the confinement region. However, the parallel current is not important for the equilibrium of a short-fat mirror like Constance B, where components of the much larger perpendicular current spread in all directions because of the magnetic flux fanning and make the parallel current a minor effect. Therefore, we have neglected the parallel current in our analysis.

(2) Because the Constance magnetic geometry is not long-thin, the paraxial approximation cannot be applied to the equilibrium analysis. The plasmas in Constance are generated with microwaves and exist in regions defined by the resonant mod-B surfaces. The ratio between the radial and axial extent of these mod-B surfaces is about 1:1.6, and is roughly constant to the radius of these surfaces. Thus the long-thin approximation is not satisfied even at high field shots in which the plasma radial size is small. Without the long-thin approximation, our equilibrium analysis is forced to rely largely on computational studies. With the amount of data needed to be calculated for comparison with the experimental measurements and determining the equilibrium, the computational requirements are too large for a self-consistent solution. Therefore, we used the vacuum field in the calculation instead of a self-consistent equilibrium magnetic field.

Under the above two approximations, the magnetic field generated by the plasma current is calculated using

$$\tilde{B} = \frac{\mu_0}{4\pi} \int \frac{\vec{J}_\perp \times \vec{r}}{r^3} d^3x.$$

By letting $\vec{B} = B_0 \hat{B}(\vec{x})\, \vec{b}$, and $P_{\perp,\parallel} = P_{peak} \hat{P}_{\perp,\parallel}(\vec{x})$, with $(\hat{P}_\perp + \hat{P}_\parallel)$ normalized to one at the peak pressure location and $\hat{B}$ normalized to one at the bottom of the mirror well, the diamagnetic field can be expressed as

$$\tilde{B} = \beta_{peak} B_0 \left[\frac{1}{8\pi} \int \frac{\left\{ \vec{b} \times [\nabla_\perp \hat{P}_\perp + (\hat{P}_\parallel - \hat{P}_\perp)\vec{\kappa}] \right\} \times \vec{r}}{\hat{B} r^3} d^3x \right], \tag{4.8}$$

where the peak beta is defined by $\beta_{peak} \equiv 2\mu_0 P_{peak}/B_0^2$. The expression inside the bracket is a function of the normalized pressure and magnetic profiles. We numerically

calculate this profile factor for given plasma pressure models and compare the results with the measurements. The analytical magnetic field expression given in Appendix A is used in the calculation.

4.3.2 Experimental Arrangement

In order to determine the equilibrium pressure profile, one can divide any two magnetic signals to cancel the beta factor in Eq. (4.8). The ratio between the signals is then a function of the plasma pressure profile only and can be used for the equilibrium determination. Once the plasma profile is known, the total stored energy and the plasma beta can be easily calculated.

The plasma magnetic field is measured with diamagnetic loops and magnetic probes. The diamagnetic loops encircle the plasma at different axial locations and respond mainly to the total stored energy because of their large size. The magnetic probes, which are located outside the plasma, are more sensitive to the local plasma current. By comparing magnetic signals measured at different locations, we found that the ratios between the diamagnetic loop and the magnetic probe signals are most suitable for equilibrium determination. For example, the midplane diamagnetic loop signal is dominated by the plasma dipole field. However, the radial component of the dipole field at the magnetic midplane is zero. A B_x probe at the horizontal symmetry plane senses only the quadrupole field which is generated due to the magnetic field fanning and increases with radius. Thus, the ratio between the dipole and the quadrupole signals is a sensitive measure of the plasma current radial location.

The magnetic probe arrangement was shown in Fig. 2.1(b). The probes can be placed at five axial locations ($z = 0, \pm 10, \pm 20$ cm). The B_x probe at the midplane is most sensitive to the plasma radial profile, while the probes off the midplane are more sensitive to the axial plasma length. The baseball seam shaped diamagnetic loop is centered at the magnetic midplane while one circular and two elliptical loops

are located at $z = 2.5, 10$, and 22 cm, respectively. The response of the diamagnetic loops to the plasma current profile is mainly determined by the loop locations rather than their shape and size. Figure 4.5 shows an example of the measured diamagnetic loop, a B_x probe and a B_z probe signals and their ratios.

4.3.3 Experimental Results

The signal ratios between the midplane diamagnetic loop and magnetic probes measured at four axial locations are shown in Fig. 4.6. The plasma pressure profile is determined by comparing these measured signal ratios with the numerically calculations for given plasma models. There are eight independent parameters in the pressure profile model. To analyze the amount of data which comes from such a multi-dimensional parameter space, we use a graphical method to present the data.

Figure 4.7 shows the calculated ratios between the signals of the midplane diamagnetic loop and a B_x probe at r = 15.2 cm on the midplane for 81 model plasma profiles. The data is organized into 9 boxes. Inside each box, the horizontal axis is J_p (see Fig. 3.12), which represents the radius of the plasma pressure peak; the vertical variable is p_0, which reflects the hollowness on the magnetic axis. Between the boxes, the horizontal variable is c_1, which determines the sharpness of the plasma edge; in the vertical direction, three $P_1(B)$ profiles shown in Fig. 4.8 are represented. By presenting the data in this way, four dimensional variations of the pressure profile parameters can be analyzed simultaneously. The trend of the signal change with the plasma profiles and the sensitivity of the signal to various pressure models are also clearly seen.

The signal presented in Fig. 4.7 is the signal which is most sensitive to the radial pressure profile change. As a comparison, Fig. 4.9 shows the calculated signal ratios between the diamagnetic loop and a B_z probe at the midplane. We see that these ratios are essentially independent of the pressure profile change within the parameter

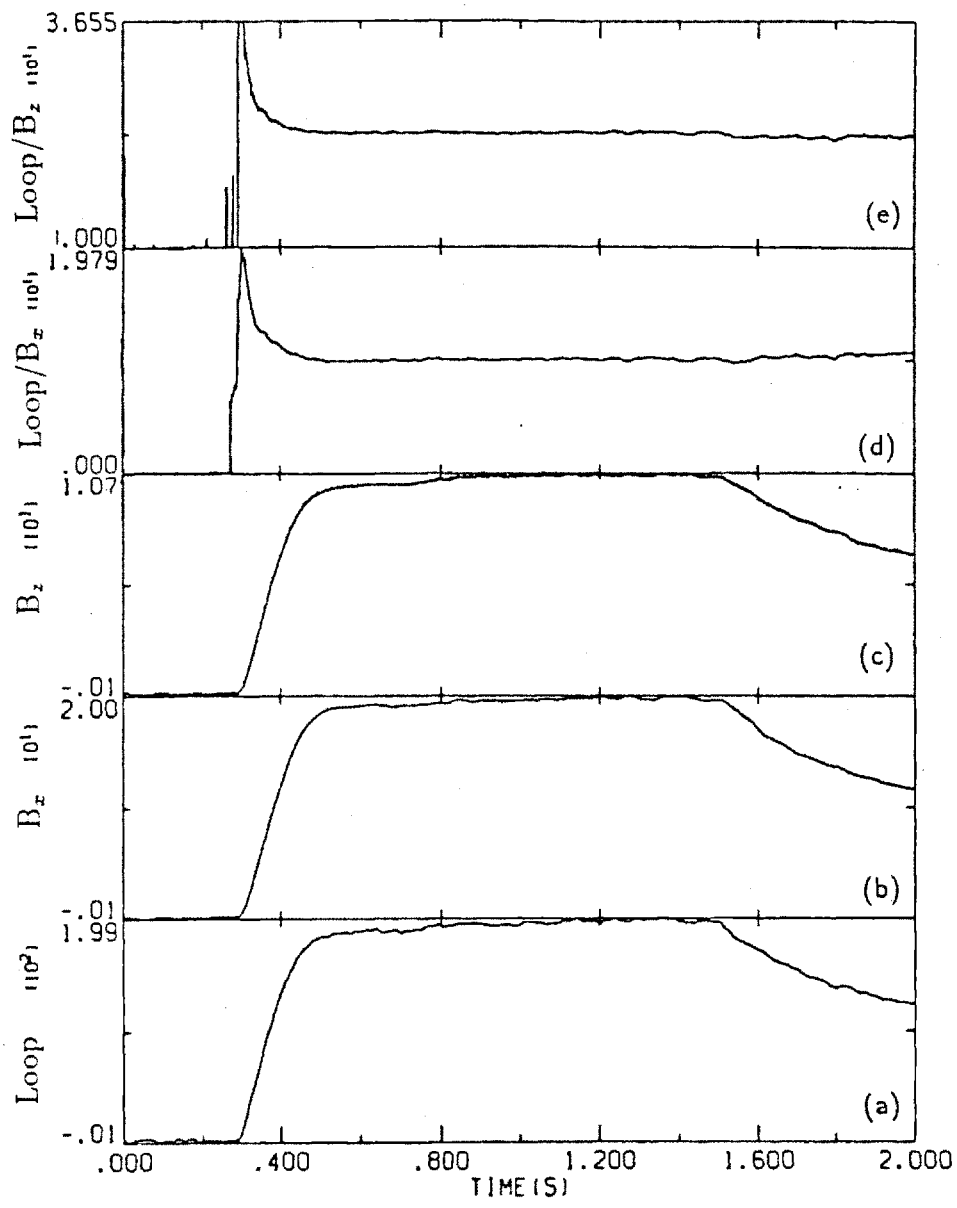

Figure 4.5: Plasma diamagnetic signals measured by (a) the midplane diamagnetic loop, (b) a B_x probe, and (c) a B_z probe. The top two curves are: (d) the ratios between the loop signal and the B_x probe signal, (e) the ratios between the loop signal and the B_z probe signal.

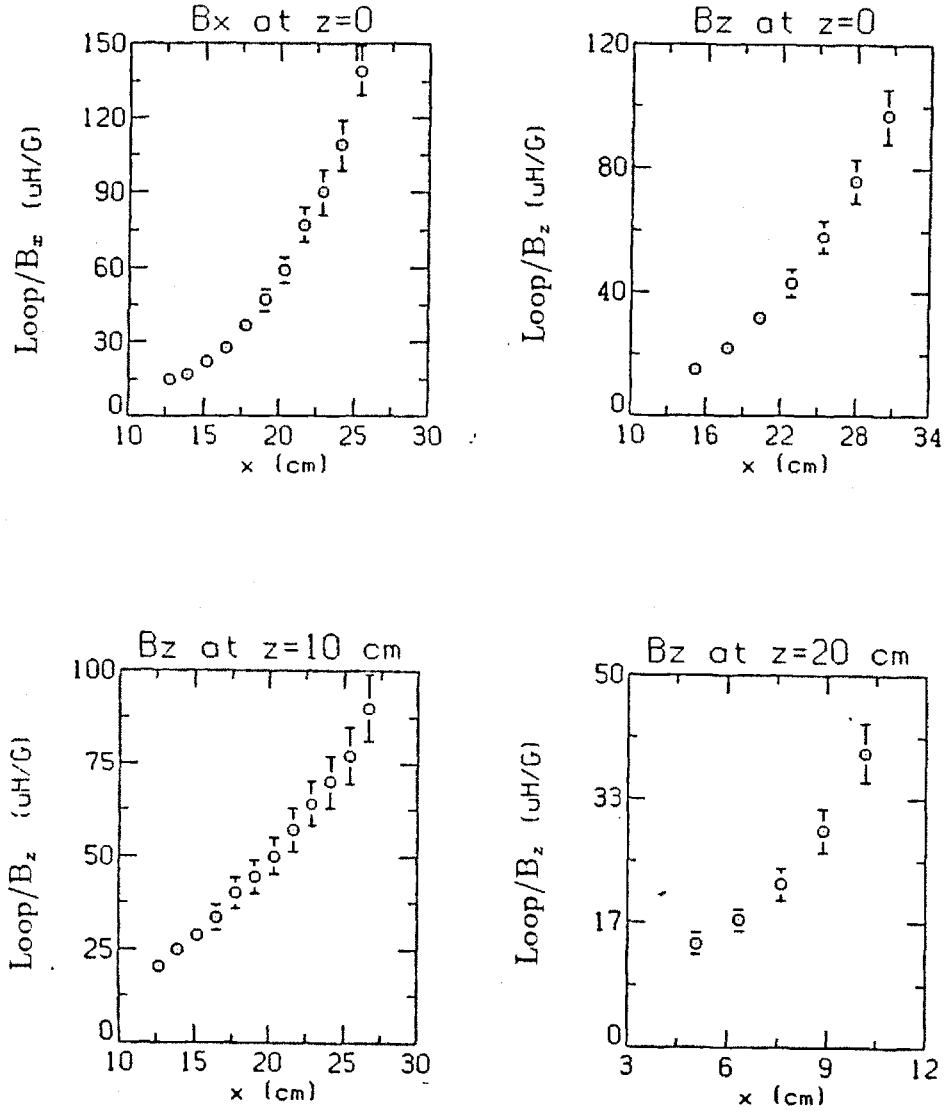

Figure 4.6: Measured signal ratios between the midplane diamagnetic loop and magnetic probes.

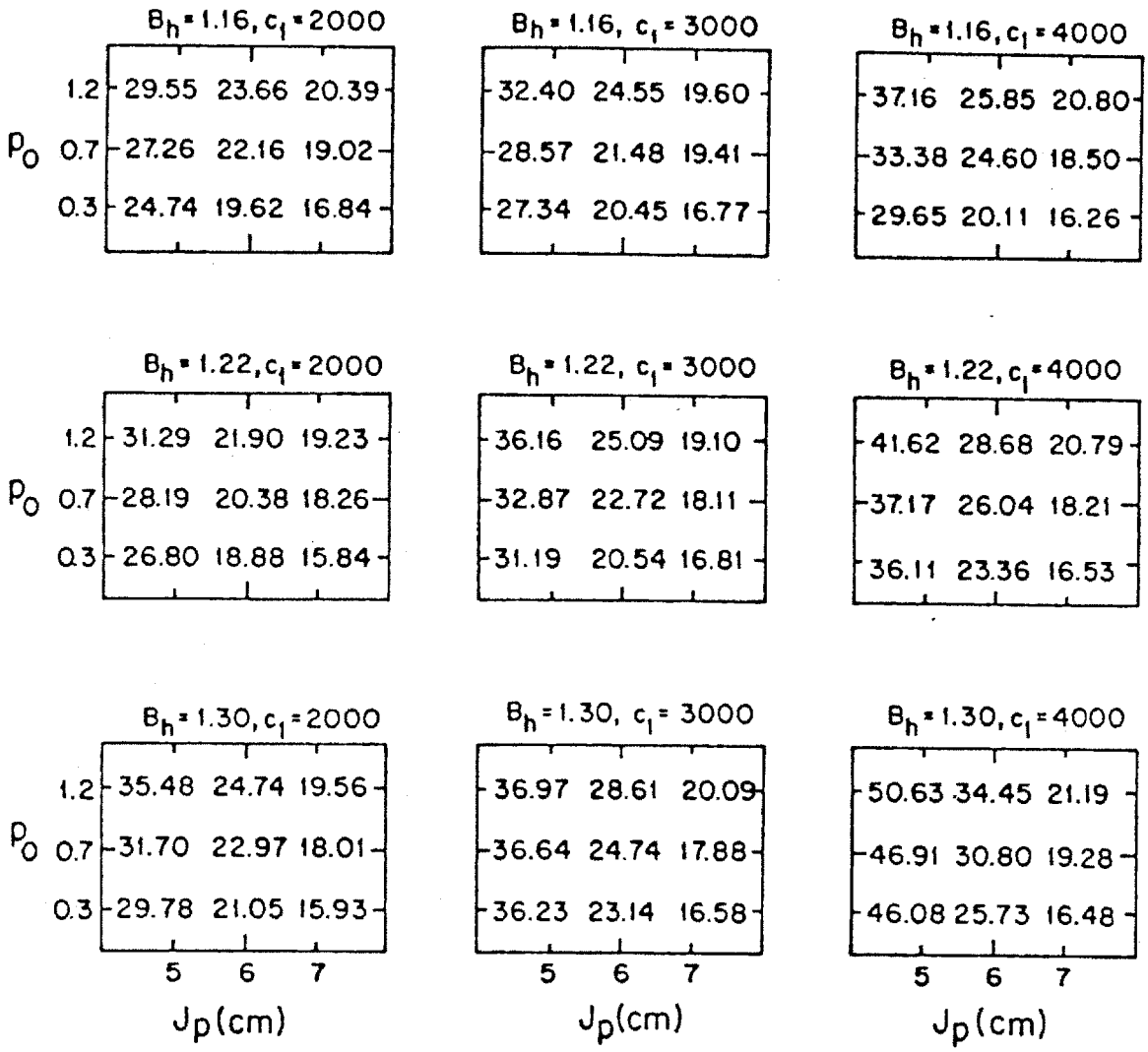

Figure 4.7: Calculated signal ratios between the midplane diamagnetic loop and a B_x probe at x=15.2 cm on the midplane. The measured signal ratio is 22.5 ± 1. The calculated results from 81 model pressure profiles are presented in the nine 3×3 matrices so that four dimensional profile parameter variations can be analyzed simultaneously. The three $P(B)$ profiles used in the calculation are shown in Fig. 4.8.

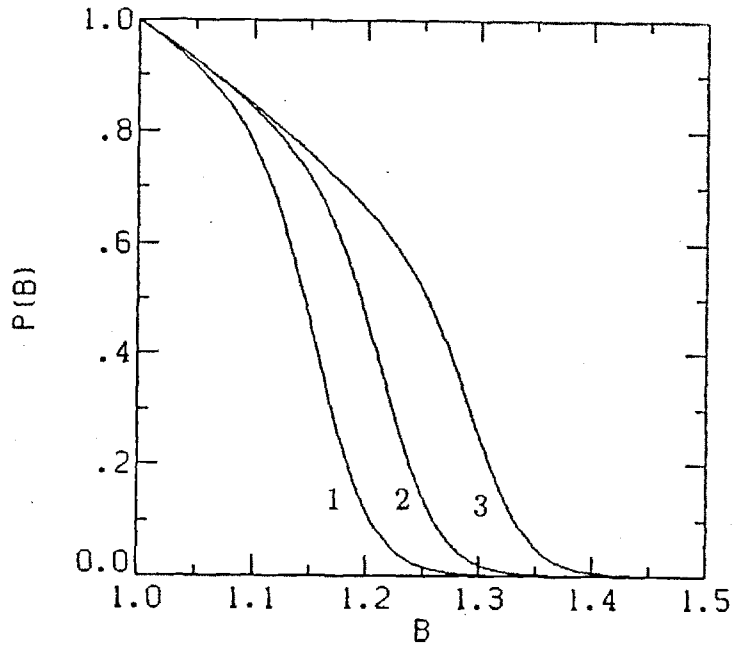

Figure 4.8: The three $P(B)$ profiles used for calculating the magnetic signal ratios. The profile labels correspond to the row number of the data blocks in Fig. 4.7.

range for the calculations.

From the B_r probe data, it is clear that the measurement is much more sensitive to the outer plasma profile than to the profile near the magnetic axis. With the value of J_p varying from 5 to 7 cm, the signal ratio varies by 30 to 50 percent. One can clearly distinguish that the best fit J_p is near 6 cm. Unfortunately, the pressure profile near the magnetic axis cannot be determined from this data. Despite variations in the hollowness from 70 % hollow to 20 % peaked, the difference in the magnetic signal is only about 10 – 20 %. One can imagine that if contours of constant loop-to-probe signal ratio are drawn inside each data box, these curves will be nearly vertical lines. When the measured signal ratio is compared with these predicted ratios, only the plasma outer radius can be determined. Other magnetic signals are all similar in this respect because the plasma volume near the axis is small and the coupling to

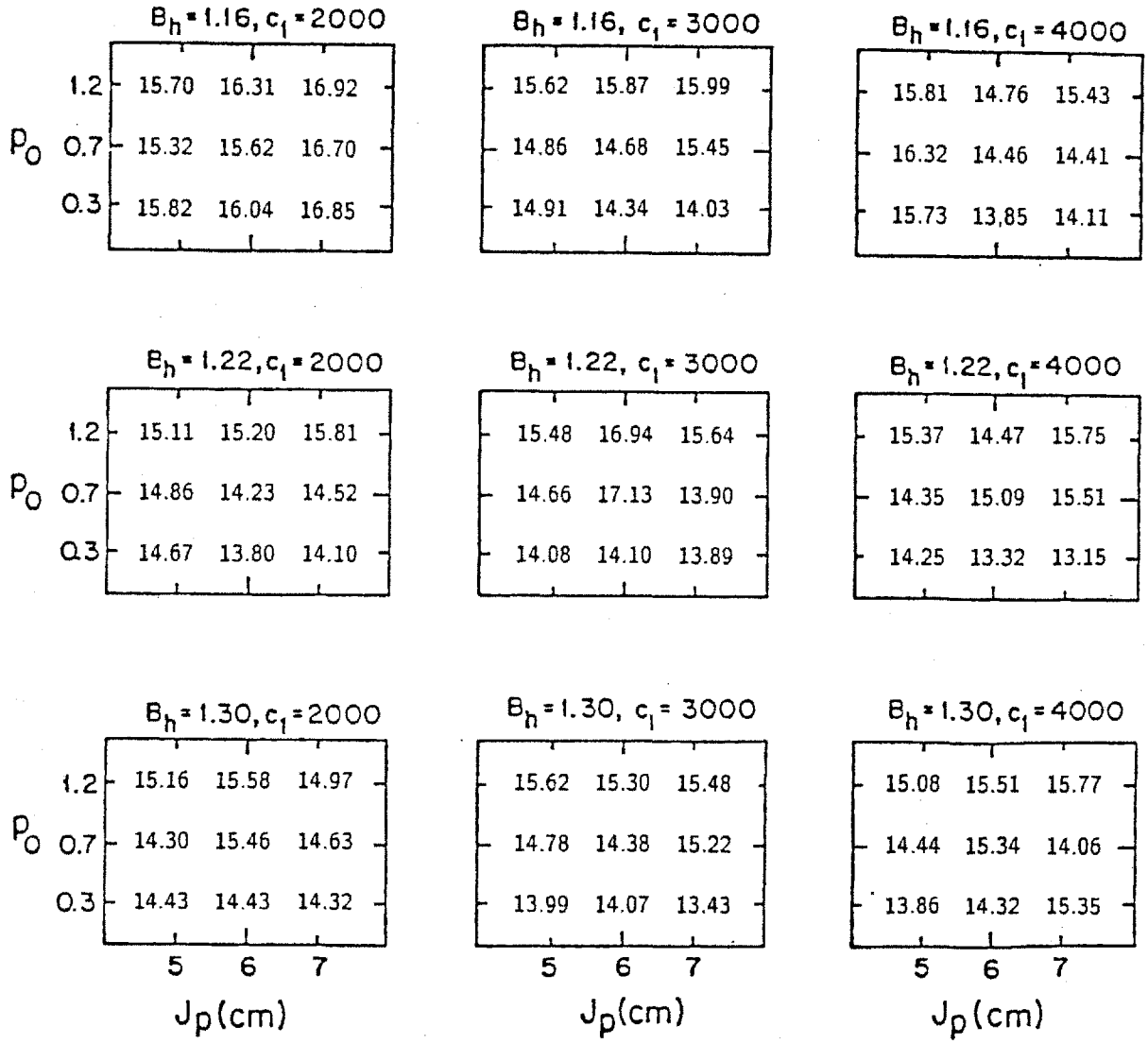

Figure 4.9: Calculated signal ratios between the midplane diamagnetic loop and a B_z probe at $x = 15.2$ cm at the midplane. The measured signal is 14.8 ± 0.7. The data shows that this signal is insensitive to the plasma profile change.

the probe is weak compared with that of the outer plasma. Considering that the measurement accuracy of the diamagnetic probes is about 5 percent, and that several approximations have been used in the numerical simulation, we estimate that the accuracy of the magnetic analysis is about 10 percent. We conclude that the magnetic measurements cannot be used to accurately determine the plasma hollowness.

An estimate of the hollowness of the plasma pressure profile can be obtained from the diamagnetism change in the skimmer probe radial scan. The data presented in Fig. 3.8 is the diamagnetic signal versus skimmer probe position inserted along the line at $z = -10$ cm in the horizontal symmetry plane. When the skimmer probe intersects a field line at an axial position inside the ECRH resonant surface, the probe blocks the access to the resonance zone for electrons on that field line. It also wipes out the plasma on that drift surface as the particles drift around the magnetic axis. As seen in Fig. 2.1, the ECRH resonant surface in Constance is egg-shaped, and the resonance for field lines near the axis extends to $z = 17$ cm. Thus one can affect the radial plasma pressure profile by inserting a radial skimmer probe off the midplane which reduces the pressure on field lines near the axis while barely affecting the outlying plasma. We model the effect of the skimmer probe by assuming that on field lines where the probe is outside the resonance zone the plasma pressure is not affected by the probe, and once the probe penetrates the resonance zone the pressure on the drift surfaces which contact the probe is reduced to zero. We then take the ratio between the diamagnetism predicted by this model as a function of the probe position with the diamagnetism predicted by the unperturbed pressure profiles with varying degrees of hollowness on the axis. This ratio gives an indication of the expected decrease of diamagnetism due to the insertion of the probe as function of the hollowness of the unperturbed plasma. The calculation shows that if the pressure profile is originally 80 percent hollow, the diamagnetism will drop by about 21 % after

the skimmer probe is inserted. If the original profile is 50 percent hollow, the drop of diamagnetism will be 29 %. The experimental data shows that as the probe is inserted the diamagnetism decreases by about 12 percent until the probe is 2 cm from the axis when it abruptly decreases to 50 percent of its original value. This final abrupt drop we interpret as due to the droop of the probe below the horizontal symmetry plane on the basis of other skimmer probe scans in which the probe is deliberately moved off the symmetry plane. Another explanation for the final drop would be the existence of a high pressure plasma column of radius 2 cm on the axis. However, given the fact that the peak plasma temperature is about 400 keV, one would expect the hot electron density there to be at least 10 times higher than the density at the outer peak pressure location (J_p = 6 cm). This prediction directly contradicts the x-ray and visible light image measurements. The thermocouple mounted on the tip of the skimmer probe also shows that the plasma energy on the axis is a minimum rather than a maximum. Therefore such a high density column does not exist. Based on the measured diamagnetism change, we can say that the pressure profile is at least as hollow as, if not more hollow than the hot electron density.

To determine the outer radial profile, we set the hollowness to be 50 percent according to the hot electron density, and then vary the other profile parameters. The exact value of the hollowness is not crucial in determining the outer profile since its effect is small. Because most of the magnetic signals are affected by the outer profile change, we started the calculation with a wide parameter regime to include all the possible profiles. The predictions from the model profiles are compared with the experimental data to determine the best fit parameter region. The next round of calculations is then conducted in this region with refined grids until the pressure profiles converge to the region corresponding to the 5 percent experimental accuracy. The best fit radial pressure profile is plotted as the solid line in Fig. 4.10(a) together

with the density profiles determined from the visible light and x-ray image measurements. Notice that the plasma radial pressure profile is smaller than the hot electron density profile. The peak pressure is at $J_* = 6$ cm and the peak hot electron density is at 6.4 cm, and the pressure drops more quickly outside the peak position. This difference between the hot electron density and pressure profiles indicates the plasma temperature is colder at the plasma edge, which agrees with the x-ray spectroscopic measurements.

The axial pressure profile is determined from the ratio between the midplane diamagnetic loop and other pickup loops and probes at different axial locations. The overall plasma length is monitored by an elliptical diamagnetic loop at z=22 cm. Figure 4.11 shows the calculated ratios between the midplane loop and the elliptical loop signals for 5 different P(B) profiles. It shows that the bulk of the plasma is within mirror ratio 1.2, which corresponds to an axial extent of z=14 cm. The plasma pressure drops to less than 5 percent outside the ECRH resonance mirror ratio 1.25. More detailed analysis is made with the magnetic probes at z=10 and 20 centimeters. When the probes are close to the plasma, they are mostly sensitive to the local pressure profile. Taking the ratio between the diamagnetic loop and the probe signals, the relative plasma pressure at the probe axial location can be determined. Figure 4.12 shows the calculated signal ratios between the midplane diamagnetic loop and B_z probes at z=20 cm. These signals are mainly determined by the axial plasma length and relatively insensitive to the radial pressure profile change. We see that the best fit $P(B)$ profile is somewhere between the first two curves in Fig. 4.8. After having analyzed all the magnetic measurements, we conclude that the best fit plasma pressure profile is the one defined by the parameters $n = 4.5, k = 40, B_h = 1.19; p_0 = 0.5, p_1 = 0.75, p_p = 1., j_1 = 0.035, j_p = 0.06, c_1 = 3000.$

An important feature of the plasma pressure is that the bulk of the plasma is

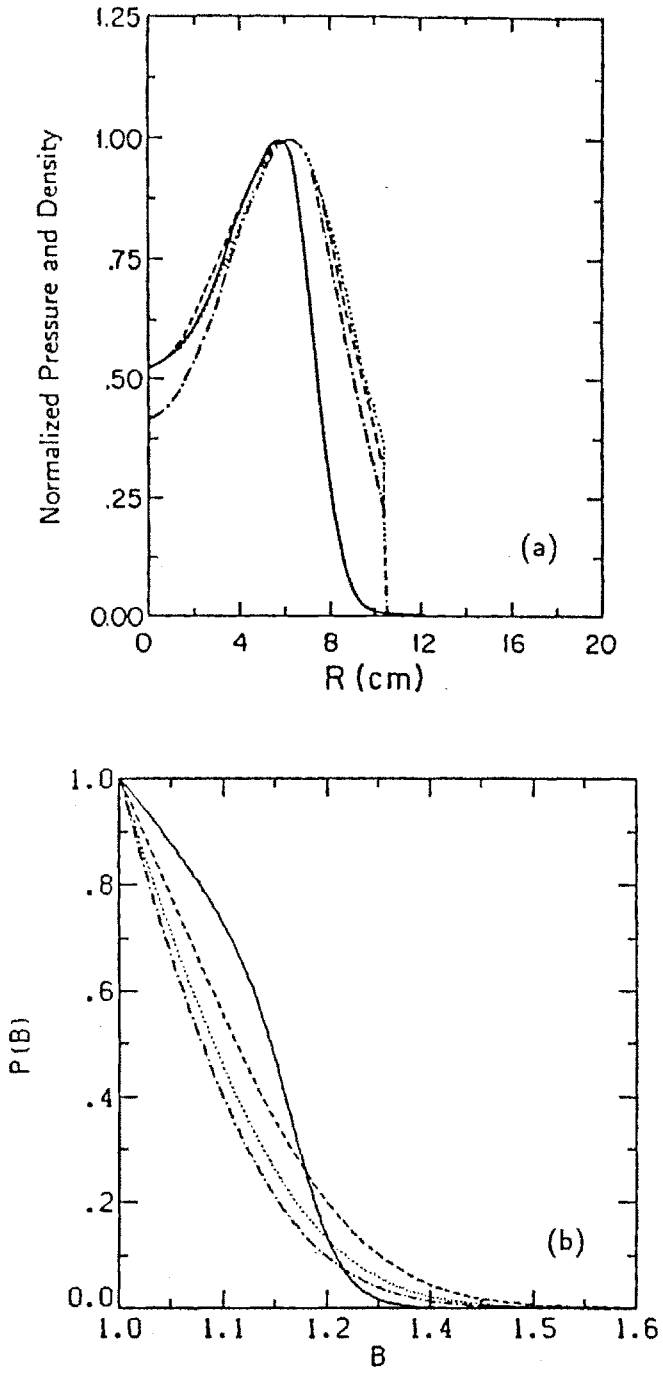

Figure 4.10: (a) The best fit radial plasma density and pressure profiles at 45 degrees at the midplane. (b) The best fit axial density and pressure profiles. The dotted, dashed and dash-dot lines are the hot electron density profiles determined from the visible light image, the x-ray image with the n_{eh}^2 model and the x-ray image with the $n_{eh}^{3/2}$ model, respectively. The solid line is the pressure profile determined from the magnetic measurement, with the hollowness set according to the hot electron density profile.

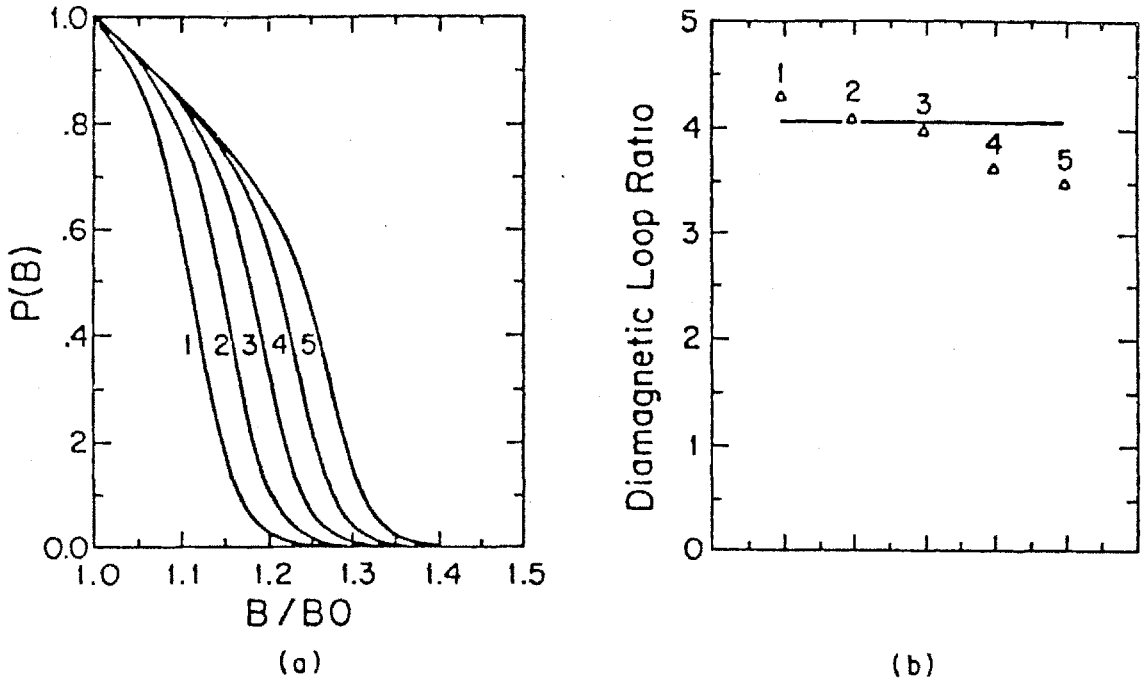

Figure 4.11: Calculated signal ratios between the midplane diamagnetic loop and an elliptical diamagnetic loop at z=22 cm from 5 model axial pressure profiles. (a) Pressure profiles. (b) Calculated signal ratios. The measured signal ratio is 4.05 ± 0.1, which is shown by the solid line.

confined inside the ECRH resonant surface. To relate this pressure profile to the underlying pitch angle distribution function, one can take an Abel inversion of the plasma pressure profile $P_\perp(B)$ [Grad, 1967; Hall, 1974]. However, it is more instructive to directly integrate some commonly used velocity distribution functions and compare them with the measurement. Figure 4.13 shows the experimentally determined $P_\perp(B)$ profiles and pressure profiles calculated from a bi-Maxwellian loss cone and an ECRH loss cone distribution [Garner, 1987]. With the bi-Maxwellian loss cone distribution, the pressure profile is always sharply peaked at the magnetic minimum. With a distribution function which is nearly flat inside the ECRH heating line, the corresponding pressure profile is much closer to the measured one.

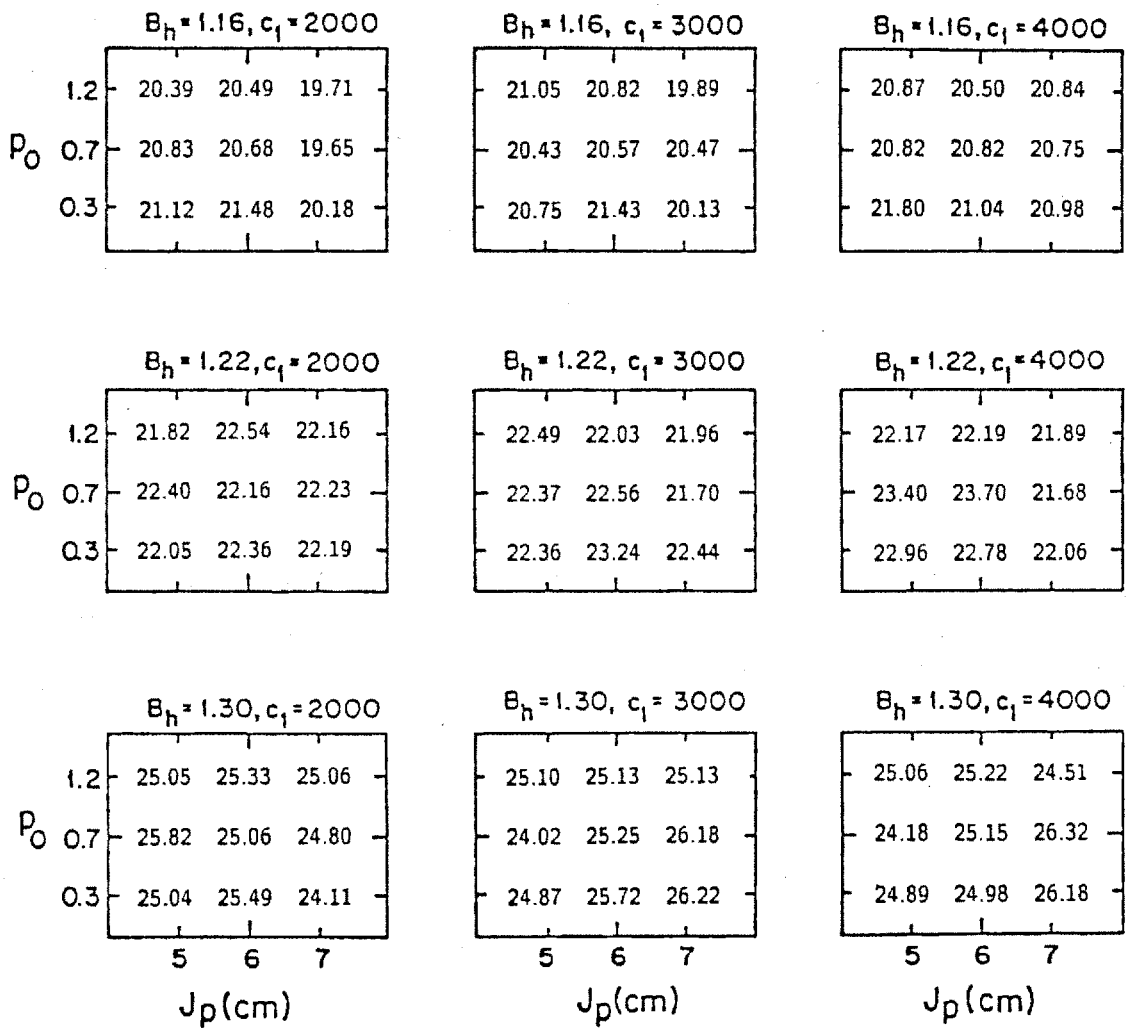

Figure 4.12: The calculated diamagnetic loop to a B_z probe signal ratio from 81 model pressure profiles. The measured ratio is 21. $\pm$ 1 with the B_z probe at $z = -20$ cm, $x = 7.6$ cm.

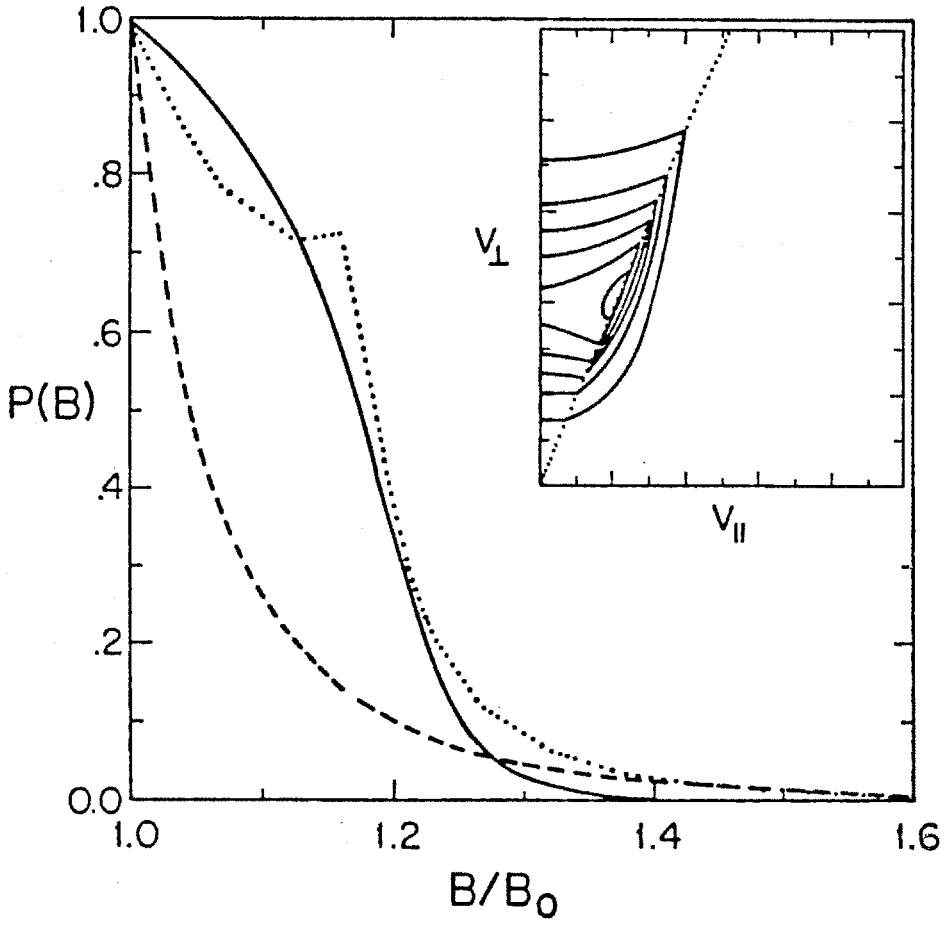

Figure 4.13: P(B) profile determined from the magnetic measurement compared with the pressures calculated from two velocity distribution functions. The dashed line is the pressure from a bi-Maxwellian loss cone distribution with $T_\perp/T_\parallel = 5$. The dotted line is the pressure from the ECRH loss cone distribution shown in the inset.

4.4 Thermocouple Probe and Skimmer Probe Measurements

The radial plasma boundary and the end loss profile are measured with thermocouple probes inserted into the plasma. During the ECRH pulse the probe draws a plasma current since its circuit is similar to a Langmuir probe. This current interferes with the temperature measurement. We therefore measure the probe temperature difference before and after the ECRH pulse to obtain the time averaged plasma energy profile. The time response of the probe is about 2 seconds, which makes such a measurement possible.

The thermocouple probe is the most sensitive diagnostic in determining the plasma boundaries. Figure 4.14 shows the thermocouple temperature profile measured at three axial locations (z=0, 10, 20 cm), which correspond to the on axis mirror ratios of 1, 1.098 and 1.36, respectively. All the data points are mapped back to the midplane along the magnetic flux lines so that measurements at different axial locations can be compared. It shows that the hot electron plasma exists only on the field lines on which the nonrelativistic electron cyclotron resonance occurs. It should be remembered that the data points do not correspond to the plasma pressure profile because the plasma is perturbed when the probe is pushed into the plasma.

At z=20 cm, the thermocouple probe can be used to scan across the entire magnetic flux tube. Since the probe acts as an axial plasma limiter, the hot electrons will hit the probe before they can reach the mirror peak as they drift around the magnetic axis. Thus the probe measures a particle energy profile which is equal to the ECRH power deposition profile, assuming that the radial energy transport is small compared with the axial loss. We see that a 90 % hollow ECRH energy absorption profile is measured. To determine the thickness of the layer where most of the ECRH power is absorbed, one can follow the field lines back to the hot electron confinement region.

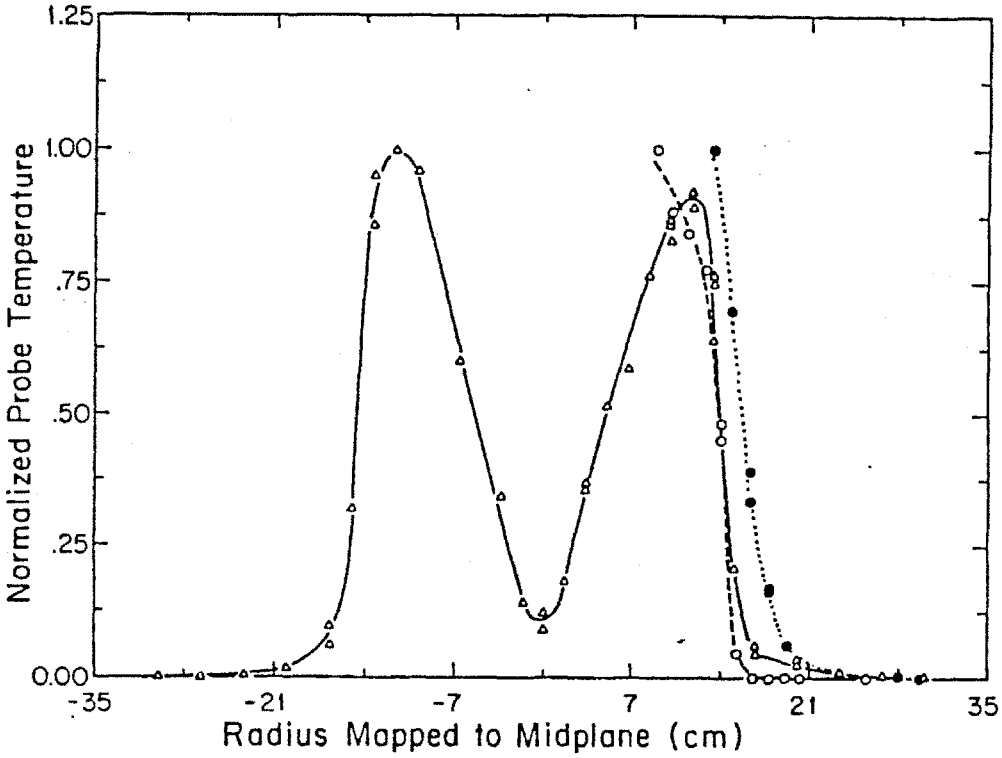

Figure 4.14: Thermocouple temperature profiles measured at three axial locations. The radial positions are mapped to the midplane. The dashed, dotted and solid lines connect the data points measured at z=0, 10, and 20 cm, respectively. The peak temperature at each location is normalized to 1. The midplane radius of the field line tangent to the ECRH resonant surface is 19 cm.

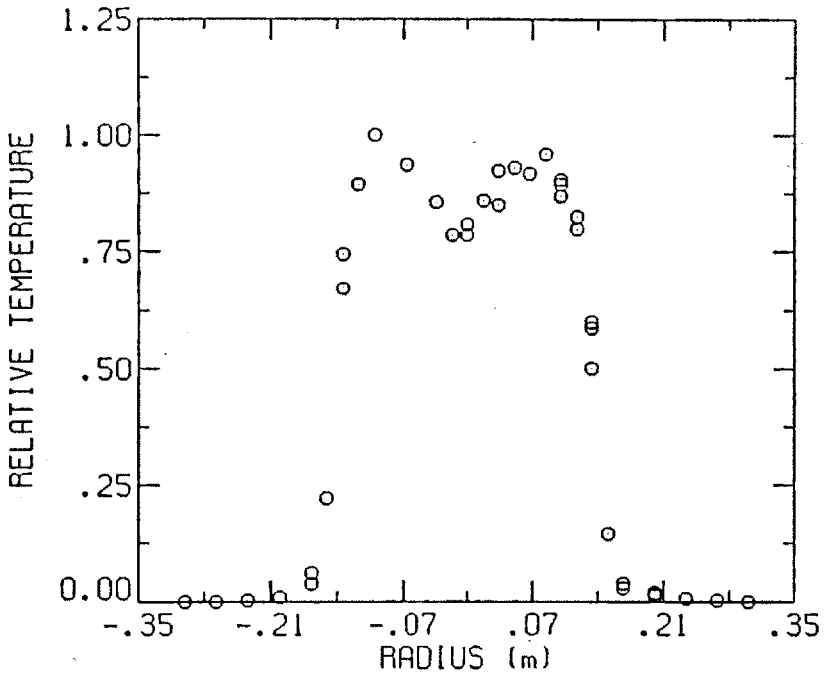

Figure 4.15: Normalized radial power absorption profile from the thermocouple probe measurement.

The data shows that 90 percent of the ECRH power is absorbed in the region where the hot electrons peak and the thickness of this layer is about 4–4.5 cm, which is about 6 to 7 hot electron gyroradii. The normalized radial power absorption profile is obtained by taking the probe width, the hot electron azimuthal drift and the finite Larmor radius (FLR) effect into account. We multiply the probe signal by the ratio between the effective probe area and the cross-section of the flux tube in which the hot electrons will hit the thermocouple joint. Figure 4.15 shows the resulted power absorption profile versus the horizontal axis at the midplane. The peak power absorption corresponds to the field line with a midplane radius of 10 cm at symmetry plane, which corresponds to $J_* = 7$ cm. This peak position is not on the field line tangent to the resonant surface but on a line which has a vacuum field ECRH resonant mirror ratio of 1:1.09.

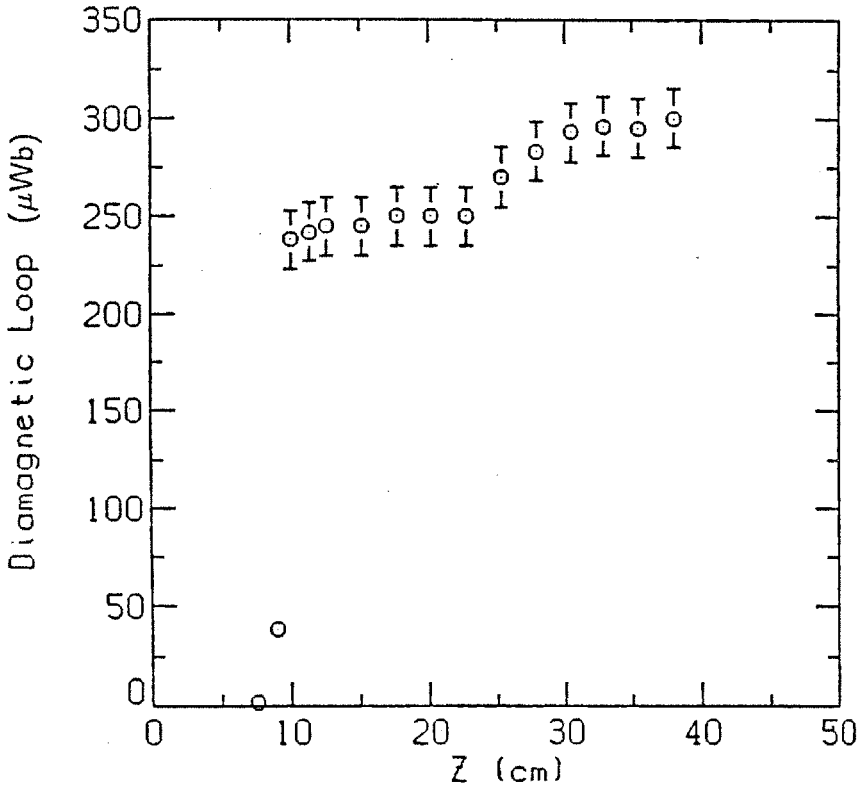

Figure 4.16: Plasma diamagnetism measured during a skimmer probe scan along the magnetic axis.

Skimmer probes are also inserted along the magnetic axis to determine the axial extent of the plasma and to test if it is possible to produce a hundred percent hollow plasma. Figure 4.16 shows the plasma diamagnetism change as a function of the probe position. Note that the probe started to perturb the plasma when it was still outside the ECRH resonant surface. But the perturbation is less than 20 percent even though the probe is inserted into one third of the resonance. Delay of plasma breakdown is observed when the probe is in the plasma, and it eventually makes the delay longer than the ECRH pulse. Increasing the gas pressure reduces this delay. At neutral pressures of 2×10^{-6} torr, the plasma can be generated with the probe at $z = 3$ cm. It is noticed that even though the plasma diamagnetism is strongly perturbed by the probe, the ratio between the midplane and the elliptical loop signals is not changed,

indicating that the plasma profile at larger radius is not affected much by the probe. A magnetic probe mounted on the skimmer probe measured a negative magnetic field when the probe was at positions with $z \leq 10$ cm. Numerical calculations showed that the plasma field could be barely negative only within a centimeter or so to the midplane for 100 percent hollow pressure models. Because of the large perturbation at the probe location, this signal does not give any information about the unperturbed plasma equilibrium. However, it shows that with the probe in the plasma a nearly 100 % hollow plasma profile can be generated.

4.5 Total Stored Energy

When the plasma pressure profile is known, the plasma beta and the total stored energy can be calculated. Experimentally, these parameters are determined using the plasma diamagnetic loop signals which are relatively insensitive to the details of the plasma profile. The diamagnetic loop signal is calculated using

$$\begin{aligned} \phi &= \int \tilde{B} \cdot d\vec{s} \\ &= \beta_{peak} B_0 \left[\frac{1}{8\pi} \oint d\vec{l} \cdot \int \frac{\vec{b} \times [\nabla_\perp \hat{P}_\perp + (\hat{P}_\parallel - \hat{P}_\perp)\vec{\kappa}]}{\hat{B}r} d^3x \right]. \end{aligned} \tag{4.9}$$

The expression in the bracket is a geometry factor depending upon the pressure and magnetic profiles and the loop geometry. It is numerically calculated for the pressure models which best fit the experimental observations. In the typical operating conditions, the integral in the bracket is 0.295 (microweber/G) for the midplane diamagnetic loop. Experimentally, the measured flux is between 290 – 300 microweber. The corresponding plasma beta is then

$$\beta_{peak} = \frac{290}{0.295 \times 3000} = 33\%.$$

The total stored energy is calculated from

$$W = \int \left(P_\perp + \frac{1}{2} P_\parallel \right) d^3x$$

$$= \beta_{peak}\left(\frac{B_0^2}{2\mu_0}\right)\left[\int\left(\hat{P}_\perp(\vec{x})+\frac{1}{2}\hat{P}_\parallel(\vec{x})\right)d^3x\right] \qquad (4.10)$$

The expression in the bracket is again a geometric factor which is the normalized plasma volume. For the standard operating conditions its value is 0.0039 m^3. Taking the peak beta to be 0.33, the total stored energy is 80 J. The accuracy of the measurement is about 10 - 20 percent.

4.6 Equilibrium under Other Conditions

Up to this point, we have concentrated on the analysis of the plasma equilibrium under a particular operating condition. We now look at the plasma equilibrium in other parameter regimes. Experimentally the characteristic baseball seam plasma equilibrium is observed under all the conditions in which the equilibrium has been measured, ranging from magnetic fields of 2.8–3.75 kG, ECRH microwave power from 10 W to 4 kW, and neutral gas pressure varying from 2×10^{-7} to 4×10^{-5} Torr.

4.6.1 High Field Experiments

The baseball seam plasma equilibrium is observed when the vacuum magnetic field is raised. In a magnetic field scan, the plasma size is observed to scale with the ECRH resonance surface size but the baseball seam equilibrium structure remains. An ECRH resonance inside the magnetic well is required for gas breakdown. With the vacuum magnetic field settings at $B_0 = 3.75$ kG, no plasma can be generated. When the field is lowered by only 5 Gauss, high beta, steady state plasmas ($\beta_{peak} \simeq 0.5$) can be produced. Figure 4.17 is an x-ray pinhole photograph taken in a $B_0 = 3.6$ kG shot. It shows that the plasma radius is reduced to about 4.5 cm, and the "C" structure can still be clearly seen. When the midplane magnetic field is larger than 3.5 kG, plasma expansion during the course of the ECRH pulse is observed with the visible light TV cameras. In the $B_0 = 3.6$ kG shot, the plasma radius is about 3.5 cm at

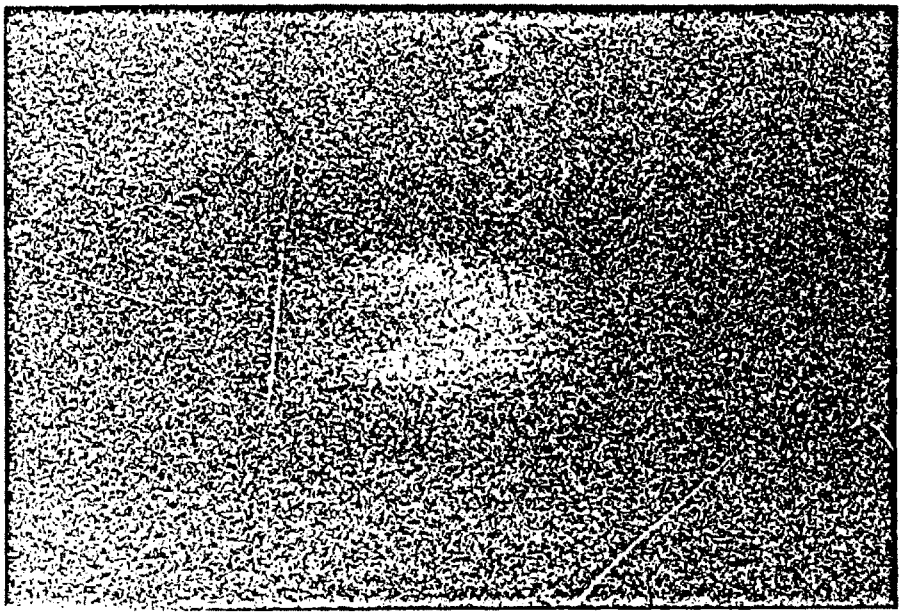

Figure 4.17: X-ray pinhole photograph taken during a $B_0 = 3.6$ kG shot. The structure of the plasma profile is the same as measured in $B_0 = 3$ kG shots. The plasma radius is nearly 1 cm (25 %) larger than the ECRH resonant surface and the expansion is associated with the increase of the total diamagnetism.

the beginning of the shot and it expands with the increase of the total stored energy. It takes about 1 second for the radius to expand to 4.5 cm and reach steady state. This expansion during the shot is believed to be due to diamagnetic depression. It is observed only when the resonance is near the bottom of the magnetic well where the gradient of the magnetic field is small. If it were due to the hot electron relativistic resonance shift, one would expect the expansion to be observed in all the cases when the hot electron temperature is at several hundred kilovolts.

4.6.2 Gas Pressure and ECRH Power Scans

In the neutral gas pressure and ECRH power scans, the plasma equilibrium is always contained in a baseball seam. The total plasma density is insensitive to the background gas density. It changes by about 50 % when the gas pressure is varied by one

to two orders of magnitude. This is markedly different from the usual charge state balance models in which the plasma density is proportional to the neutral density. The plasma density may be limited by the amount of the absorbed RF power because the reflection of the input RF wave will increase when the plasma density is increased. Also the plasma is not in an equilibrium state and the plasma confinement has a significant effect on the density.

Figure 4.18(a) shows the total stored energy as a function of the ECRH power. It shows that the plasma stored energy increases strongly at low power but starts to saturate at about 4 kW of RF power. This saturation is due to the enhanced RF diffusion of the hot electrons and has been analyzed by Hokin in his thesis. Figure 4.18(b) shows the total stored energy as a function of the background pressure. The stored energy peaks at a pressure of about 2×10^{-6} torr for the shots with 2 kW of RF power. The peak pressure increases as the power level is increased.

The most significant phenomenon observed is the plasma axial contraction during RF heating. The plasma starts with a shallowly trapped profile at the beginning of a shot and then becomes more and more deeply trapped before the profile reaches a steady state. The speed of the contraction and the final state are dependent on the neutral gas pressure and the applied ECRH power. In general, the speed of the contraction increases with increasing ECRH power or decreasing gas pressure, and the steady state plasma length decreases with increasing ECRH power and decreasing gas pressure. At low gas pressure (below 1×10^{-6} Torr) and moderate ECRH power (2 kW), the plasma length changes by 2 to 3 cm in about 0.1 seconds and the steady state plasma profile is reached before the plasma beta reaches its peak value. At high gas pressure, the contraction process is much slower. With gas pressures above 5×10^{-6} Torr, steady state pressure profiles are not reached in the 2 second long shots. Figure 4.19 shows the diamagnetic signals measured in a shot in which the gas

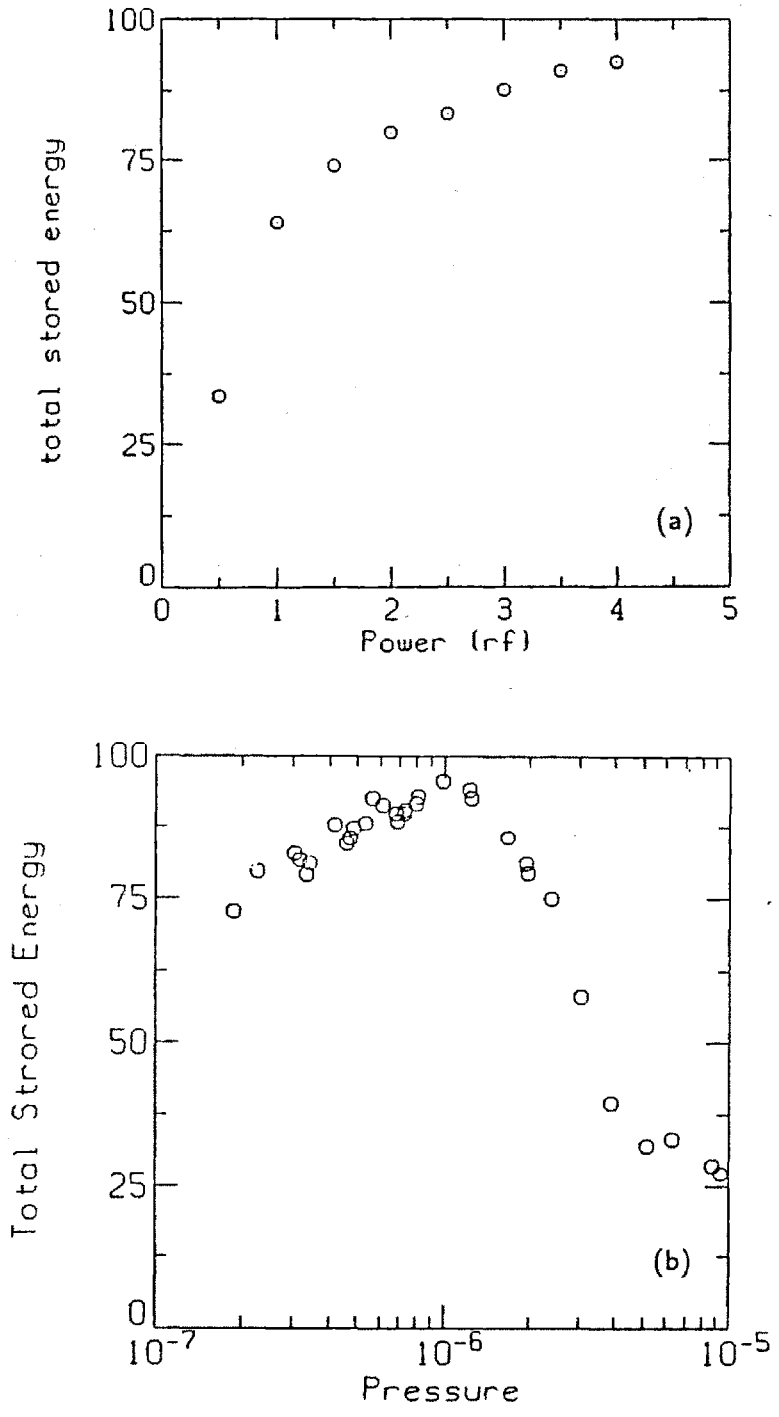

Figure 4.18: (a) Total plasma stored energy as a function of the ECRH power. The neutral gas pressure is at 7×10^{-7} torr during the scan. (b) Plasma stored energy as a function of the background gas pressure at an ECRH power of 2 kW.

puff is stopped before the RF turn-off to have the background pressure scan through a wide range. The increase of the signal ratio between the midplane diamagnetic loop and the B_z probe at z = 20 cm with the background gas pressure corresponds to contraction of the plasma length, as can be seen from the data in Fig. 4.12.

The plasma axial length is determined by the particle pitch angle distribution. For an ECRH generated plasma, electrons get perpendicular "kicks" from the resonance RF field and turn to become more deeply trapped. The effective heating rate increases at higher RF power or low background neutral density. However, the electrons also get parallel "kicks" from RF diffusion and microinstabilities, as well as Coulomb collisions. The balance between these two processes determines the equilibrium distribution function. The plasma length change shows that the plasma is more deeply trapped when the heating rate is increased.

Stable plasma can be generated at very low power levels. Figure 4.20 shows the plasma density and diamagnetism measured in a shot with 100 watts of ECRH power. Even at an RF power of 5 W, the plasma can still be generated and the visible light image shows the plasma profile is hollow, even though the plasma diamagnetism is too small to measure.

4.6.3 Equilibrium in Different Gases

The plasma equilibria in helium, oxygen, argon, and xenon gases have been observed. Stable baseball seam plasma equilibria are observed in all these plasmas. Figure 4.21 shows the plasma temperature, density and diamagnetism measured in an argon discharge. The visible light image and x-ray image show that the plasma profiles are hollow in all these plasmas. Figure 4.22 presents the plasma x-ray images measured in argon and xenon discharges. The images show that the plasmas are slightly less deeply trapped than the hydrogen plasmas in the standard experimental conditions, but they possess the essential baseball seam geometry. This plasma length change

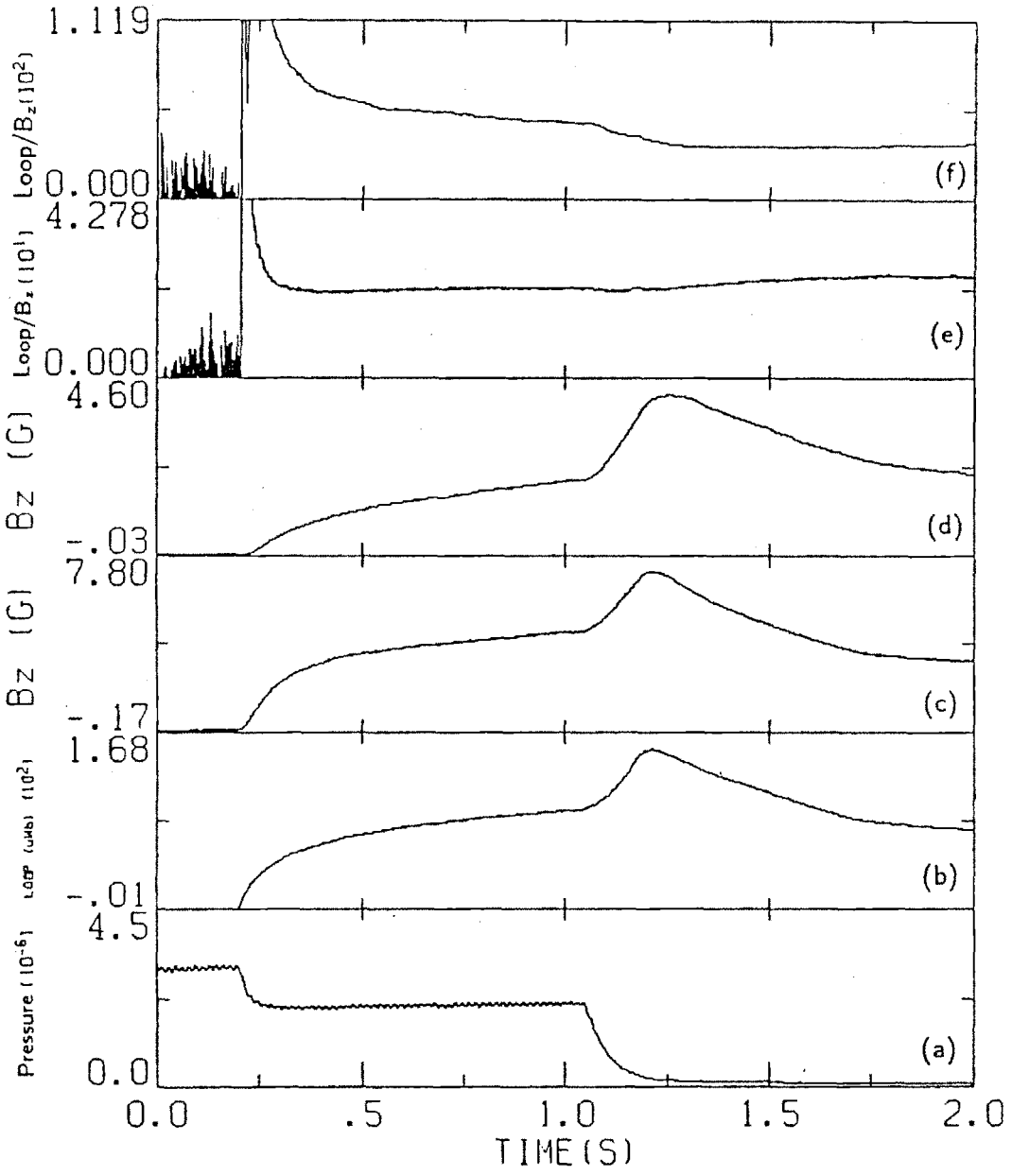

Figure 4.19: Diamagnetic signals measured in a shot in which the background pressure changes during the ECRH pulse. (a) Gas pressure. (b) Midplane diamagnetic loop. (c) Diamagnetic field at z=10 cm, x=17.2 cm. (d) Diamagnetic field at z=20 cm, x=6.8 cm. (e) Signal ratio between the loop and the magnetic probe at z=10 cm. (f) Signal ratio between the loop and the magnetic probe at z=20 cm. The decrease of the midplane diamagnetic loop signal relative to the B_z signal at z=20 cm indicates that the plasma length is contracting when the pressure is reduced. The ECRH is on from 0.2 to 1.7 sec.

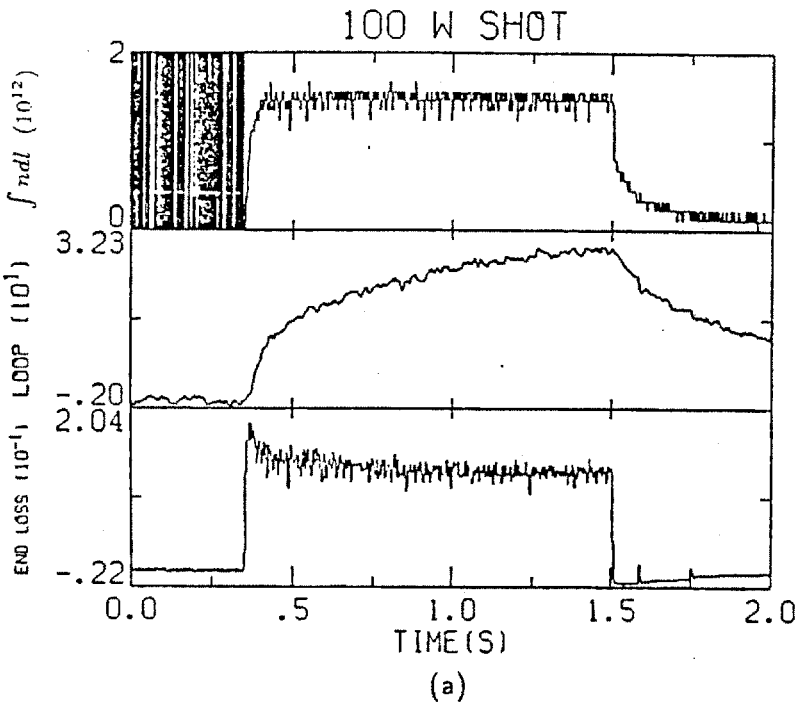

(a)

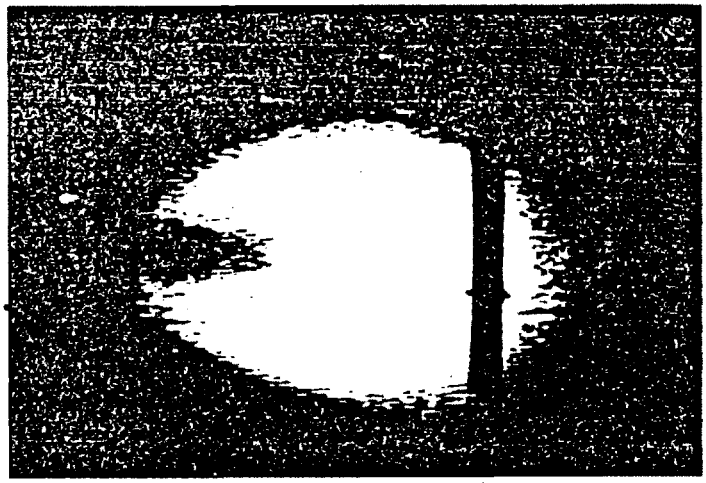

(b)

Figure 4.20: (a) Plasma density and diamagnetism measured in a 100 W shot. (b) Visible light image of the plasma in this low power shot.

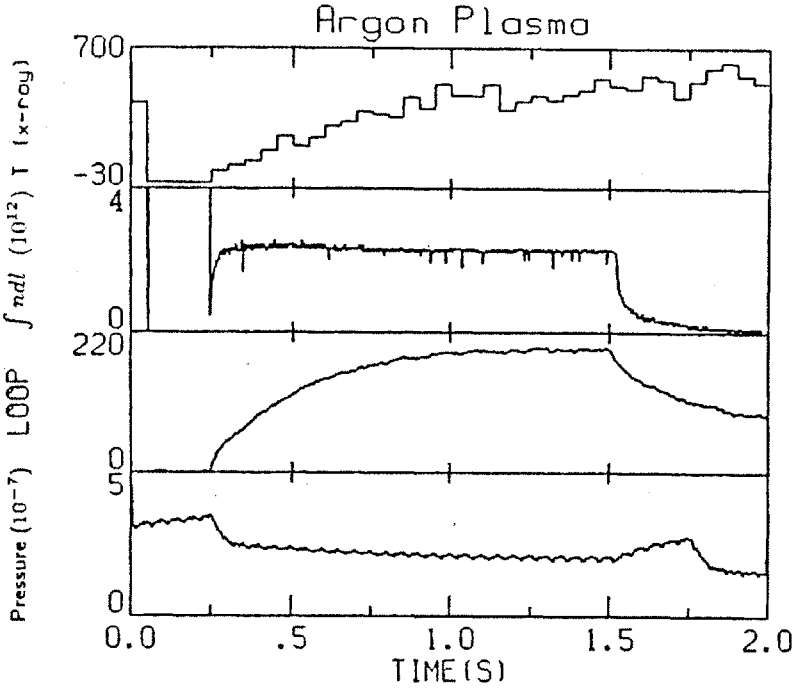

Figure 4.21: Plasma temperature, density and diamagnetism measured in an argon discharge.

may be due to the increased effective ion charge which enhances the interactions between the electrons and the ions. However, the comparison of the plasma lengths should be done between the shots with the same effective heating rate, which is not obvious when different ion species are involved. The hot electron drift frequency is comparable to the ion cyclotron frequency in a hydrogen plasma. In heavier ion plasmas, the hot electron drift frequencies are much higher than the ion cyclotron frequencies because the hot electron temperature variation is within a factor of two and the ion masses change by one or two orders of magnitude. Therefore these plasmas are in very different physics parameter region. We will discuss this in the stability analysis in the later chapters.

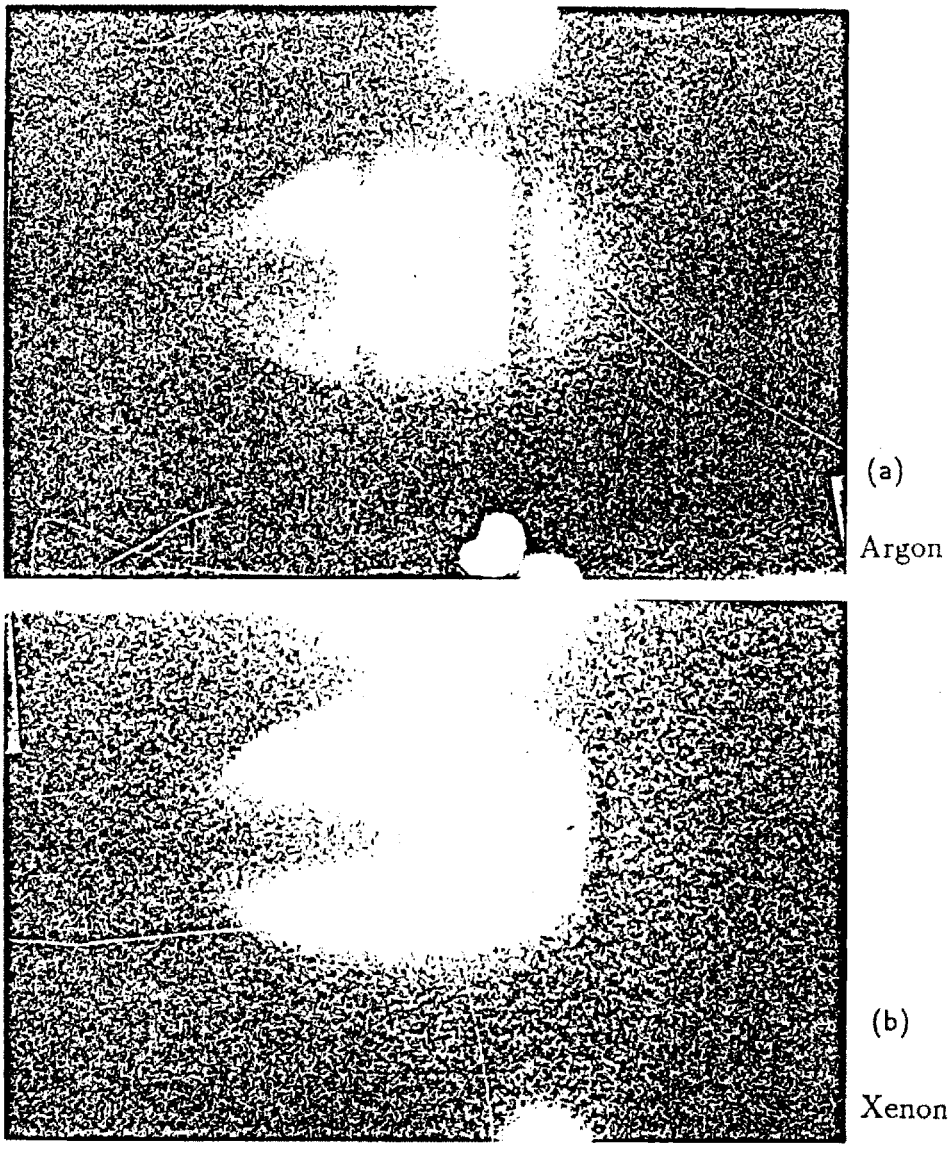

Figure 4.22: Plasma x-ray images measured in (a) an argon shot, (b) a xenon shot. The vertical bars on the argon and xenon plasma images are the ICRH antenna and a diamagnetic loop, respectively.

4.7 Is the Magnetic Field Gradient Reversed ?

With the plasma equilibrium determined, many of the plasma properties can be discussed. A primary motivation of the hot electron plasma study is that hot electrons may be used to provide a means to stabilize plasmas in otherwise unstable systems like simple mirrors, bumpy tori, and other toroidal machines. We calculated the equilibrium magnetic field gradient ∇B for the standard operating conditions, using the equilibrium relations which are expanded to the first order in beta and assuming that the magnetic field curvature change is small compared with the field gradient change

$$\nabla_\perp B = -\frac{\mu_0}{B}\nabla_\perp P_\perp + B\left[1 + \frac{2\mu_0(P_\perp - P_\parallel)}{B^2}\right]\vec{\kappa}.$$

The calculations show that for the most smooth radial functions the gradient reversal occurs at peak beta values of about 20, 23, and 27 percent for plasma pressures with hollowness 60, 50, and 40 percent. In the experiment, 30 % peak beta is regularly achieved with 2 kW of applied microwave power. In the 4 kW shots, about 40 % peak beta has been generated. Thus we conclude that magnetic field gradient reversal is achieved.

The particle drift in the equilibrium magnetic field is expected to be reversed when magnetic gradient reversal occurs. We calculated the bounce averaged hot electron drift frequency in the equilibrium magnetic field, using the guiding center drift velocity

$$\vec{v_d} = \frac{\vec{b}}{qB} \times (\mu\nabla B + m\gamma v_\parallel^2 \vec{\kappa}).$$

Figure 4.23 shows the drift frequency in the 30 percent beta equilibrium field. The distances between the turning points of the electron bounce motions are from 7 to 11 cm, which is about a quarter of the plasma axial length. It shows that for the particles on field lines inside the peak pressure position, the drift is reversed. One

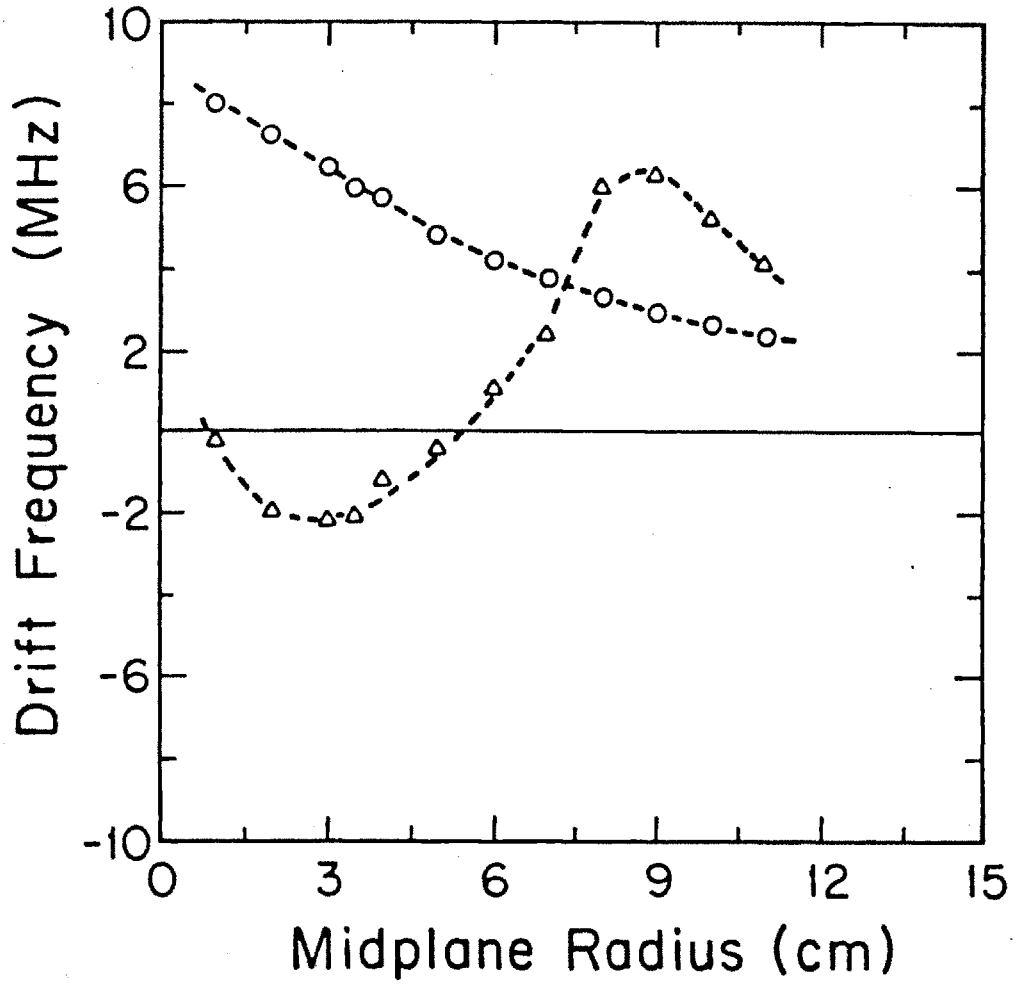

Figure 4.23: The calculated drift frequency of a 350 keV electron in the 30 percent beta equilibrium magnetic field. The circle points and the triangle points are calculated using the vacuum magnetic field and the finite beta modified field, respectively. The negative value indicates that the direction of the drift is reversed. The radius is along the x-axis in the horizontal symmetry midplane.

may expect some macroscopic plasma change associated with the transition when the particles change their drift from one direction to the other. However, this is not observed in the experiment. One should notice that the stability of the plasma is not dependent on the gradient reversal since the plasma is observed to be stable at all beta values.

4.8 Summary

We have quantitatively determined the equilibrium plasma profile of an ECRH generated hot electron plasma in a minimum-B baseball magnetic mirror using four complementary measurements, including x-ray imaging, visible light imaging, magnetic and thermocouple measurements. The primary results are:

(1) An ECRH generated hot electron plasma in a minimum-B quadrupole magnetic mirror is hollow. The plasma is confined along a baseball seam curve inside the non-relativistic ECRH resonant surface. This baseball seam equilibrium profile coincides with the drift orbit of deeply trapped electrons in the quadrupole magnetic field.

(2) Under the typical operating conditions of Constance (B_0=3 kG, ECRH power=2 kW, gas pressure=5 $\times$ 10^{-7} Torr, and plasma beta=0.3), the hollowness of the hot electron plasma density profile is 50 $\pm$ 10 percent, and the plasma pressure is at least as hollow as the hot electron density. The thickness of the hot electron layer is about 4 – 4.5 cm, or 6 – 7 hot electron Larmor radii.

(3) Hollow plasma equilibria are generated in all the experimental conditions in which equilibria have been measured, ranging from B_0 = 2.8 – 3.74 kG, ECRH power=10 – 4000 W, and neutral gas pressure= 2 $\times$ 10^{-7} – 5 $\times$ 10^{-5} Torr. The equilibrium is macroscopically stable. It exists in steady state during the several seconds long ECRH pulse and decays on a time scale of two seconds, which is many orders of magnitude longer than the characteristic MHD times.

(4) According to the pressure model which best fits the experimental observations, particle drift reversal is achieved in the experiment under the standard operating conditions. There has been no evidence that the plasma becomes unstable when the drift reversal occurs.

Chapter 5

Observations of Plasma Fluctuations

A hollow plasma equilibrium in a minimum-B magnetic mirror is expected to be subject to ideal MHD instabilities. However, the Constance plasma is in a physics parameter regime beyond the ideal MHD theory because of the existence of the hot electrons. Experimentally the plasma equilibrium is observed to be macroscopically stable, as demonstrated by the fact that the equilibrium exists on a time scale 5 – 6 orders of magnitude longer than the characteristic MHD growth time. Residual low level fluctuations, however, are observed on a variety of diagnostics. This raises the question whether the hollowness of the plasma pressure is determined by the marginal stability conditions. If this is true, we would obtain the exact stability boundary from the determination of the plasma equilibrium. If it is not the case, we would also want to know what these fluctuations are and how they affect the plasma equilibrium and confinement. In this chapter, we present the experimental data on the plasma fluctuations seen in Constance. It shows that the fluctuations are mostly the whistler microinstabilities which are caused by the anisotropy of the particle velocity distribution. The hollowness of the equilibrium profile is not limited by the macroscopic stability condition because it is possible to create almost 100 percent hollow plasma either by inserting a skimmer probe along the axis or by dropping

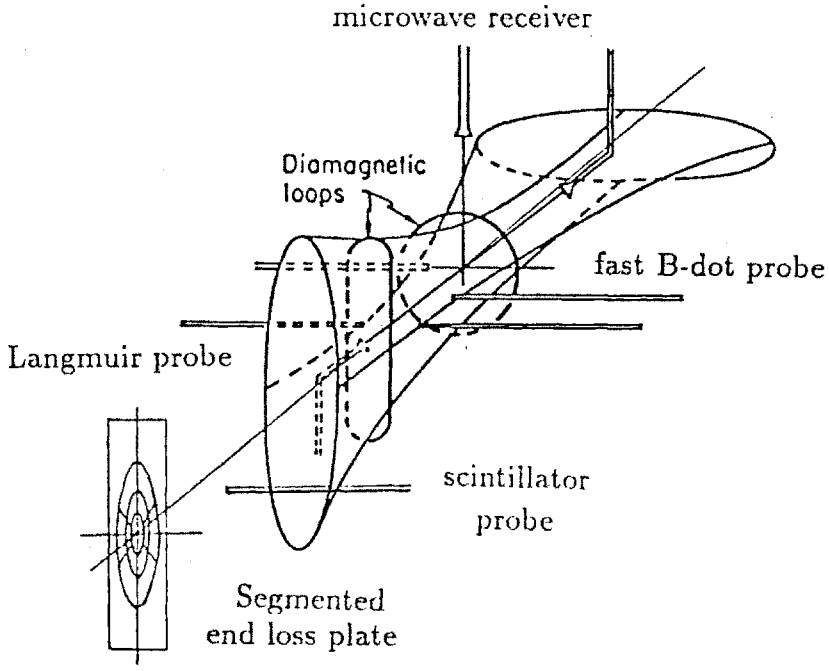

Figure 5.1: Experimental arrangement for the plasma fluctuation measurement.

small metal spheres into the plasma. Nevertheless, the measurement identified a macroscopic azimuthally propagating mode at frequencies above the hot electron drift frequency. The growth rate of this mode is small ($\omega_i/\omega_r \leq 10^{-2}$) and it saturates at very low levels ($\delta B/\bar{B} \simeq 10^{-3}$). In the next chapter, we will analyze the current MHD and hot electron stability theories and compare them with the observed plasma stability properties.

5.1 Experimental Arrangement

The plasma fluctuations are observed with several types of diagnostics: magnetic probes, an RF emission detector, end loss detectors, scintillator probes, and Langmuir probes. The experiment arrangement is shown in Fig. 5.1.

Magnetic probes are placed at $z = \pm 20$ cm near the plasma to measure the temporal and azimuthal mode structure of the instabilities. The probe frequency response is linear up to about 30 MHz. With the pickup coil looking at B_z, the probe sees mostly the diamagnetic current fluctuations and is relatively insensitive to the end loss current which flows along field lines. The spatial profile of the end loss fluctuations is measured by sets of end loss detectors at each end of the machine. The hot electron end loss is measured by the scintillator probe which is located in the fan tank. A Langmuir probe is located at the edge of the plasma at the magnetic midplane. It measures fluctuations of either the plasma potential or the density at the probe location. The total power of the plasma microwave emission in frequencies between 5–20 GHz is measured by an RF detector. The RF emission burst in this frequency range is a strong indication of the occurrence of microinstabilities.

The signals are recorded with fast digitizers at sampling rates of either 20 or 100 MHz. Because the plasma bursts usually cover only a few thousandths of the total discharge time, the digitizers are triggered by the plasma fluctuations to catch the instabilities. One of the fast signals, usually the end loss current, is used to trigger a pulse generator (Hewlett-Packard Model 8801A). The pulse generator then sends a 30 ns trigger pulse to all the digitizers simultaneously. The propagation time for the signal from the machine to the digitizer has to be taken into account. The distance from the machine to the CAMAC rack is about 10 meters and it takes about 50 ns for signals to travel down the cables. The cable lengths for all the signals are matched.

5.2 Characteristics of the Fluctuations

5.2.1 Experimental Observations

Low level plasma fluctuations have been observed in all the experimental conditions. At neutral gas pressures below 1×10^{-6} Torr, the instability normally appears in

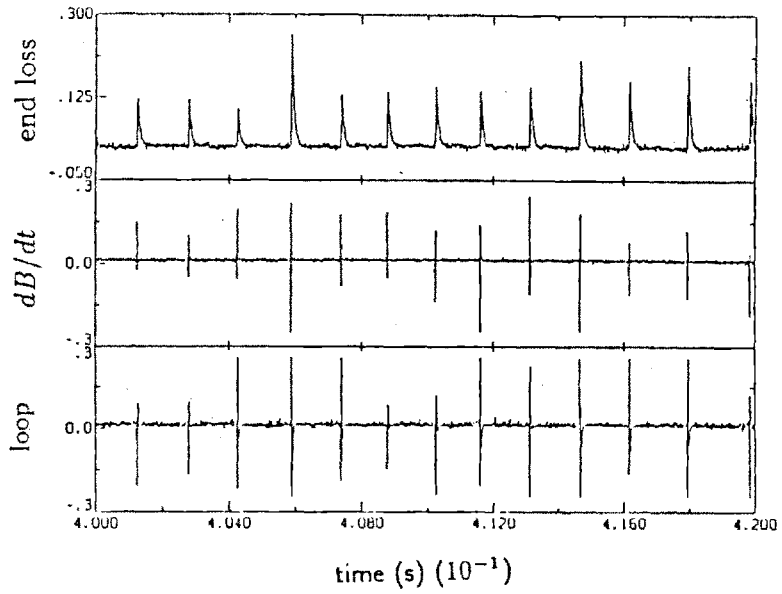

Figure 5.2: Typical bursting plasma fluctuations.

bursts, as shown in Fig. 5.2. Each burst lasts for a few microseconds and the burst rate is on the order of a few kilohertz. The rate of the bursts is dependent on the ECRH power and the neutral gas pressure. When the pressure is increased above 2×10^{-6} Torr, the burst rate is so high that the instabilities appear continuous. We will focus on the parameter ranges in which there are distinct individual bursts because the signals are clearer.

The fluctuations normally start a few milliseconds after the plasma breaks down. They persist for the entire ECRH pulse and stop after the cold electrons decay in the afterglow. There are two distinctly different types of bursts in the plasma. The first is the bursting modes which have growth rates of about 5 – 10 MHz and normally last for about 1 – 2 microseconds. The two short bursts on the right side of Fig. 5.3 are typical of such fluctuations. Expanding the signal on a faster time scale, we see a coherent oscillation at a frequency of about 6 MHz. This mode frequency can vary from 4 to 8 MHz but it is not affected by changes in the magnetic field,

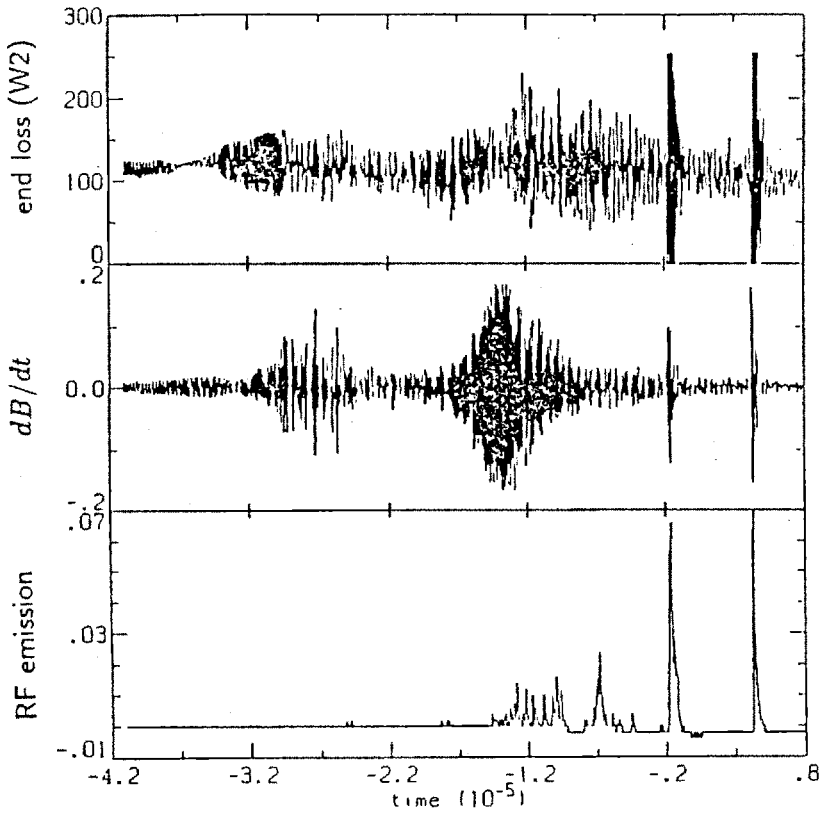

Figure 5.3: Two types of plasma fluctuations: short bursts with growth rate less than 0.1 μs, and long lasting oscillations with growth rate of a few microseconds. (a) End loss current fluctuation. (b) Magnetic fluctuation. (c) Microwave emission.

plasma density, hot electron temperature, or different ion species. Good temporal correlation for these bursts among end loss current, magnetic probes, electric probes, and the RF emission detector is always observed. The RF emission spectrum of these fluctuations has been analyzed extensively in the microinstability study by Garner [1986]. He concluded that they are whistler instabilities driven by the unstable warm electron loss cone distribution. Our analysis here will focus on studying the plasma equilibrium behavior when it is perturbed by the microinstabilities.

The second type of bursts has coherent oscillations at higher frequencies (10 – 27 MHz) but the amplitude of the oscillating magnetic field increases at a much lower rate, as the fluctuations appear on the left side of Fig. 5.3. Unlike the short microinstabilities which occurs at most of the time, this slowly growing mode is

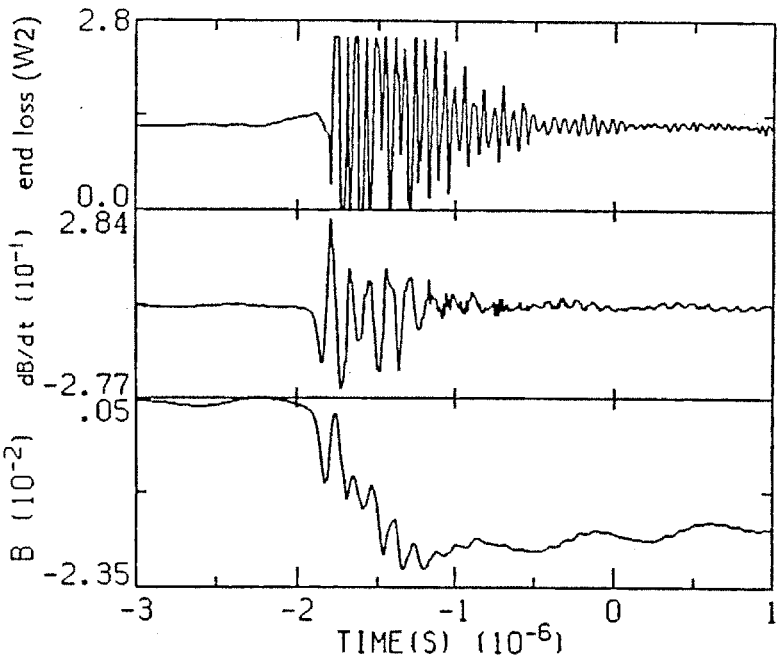

Figure 5.4: The plasma diamagnetism loss during a burst.

observed only occasionally, with an occurrence rate less than 5 percent. The signal is mostly detected on the magnetic probes. It sometimes correlates with the end loss bursts but has never correlated with the RF emission. The growth rate of this mode is on the order of a few hundred kilohertz, and the mode frequency increases with vacuum magnetic field. Because there is no RF emission associated with the magnetic fluctuations, the perturbations are most likely to be due to fluid instabilities.

The strength of the plasma fluctuations is estimated from the plasma magnetic field change during a burst. We numerically integrate the fast B-dot probe signal to obtain the field change. Figure 5.4 shows the diamagnetic field drop during a burst, which is normally on the order of a hundredth of a gauss. By comparing the field drop with the equilibrium diamagnetic field at the probe location, it is found that the largest fluctuation is on the order of $\delta B/\tilde{B} \leq 10^{-2}$ for the fast growing modes and $\delta B/\tilde{B} \leq 10^{-3}$ for the slowly growing mode. These instabilities are not disruptive but small perturbations to the plasma.

5.2.2 Plasma Parameter Regime

Before analyzing the data in detail, we now discuss some stability properties of the plasma in order to make the data easier to understand.

(1) It should be noticed that micro- and macro-instabilities co-exist in the experiment. Because of the non-Maxwellian velocity distribution, the plasma is unstable to microinstabilities. The existence of whistler instability has been confirmed by Garner from the frequency spectrum of the RF emission, which is in the frequency range near the electron cyclotron frequency. The macroscopic instabilities occur when unfavorable spatial gradients are too large. This instability mainly drives plasma to flow in configuration space through the perturbed electromagnetic fields. Even though the two types of instabilities have different origins, they can trigger each other when one of them goes unstable. We should distinguish the two processes and focus on determining the MHD stability properties of the plasma.

(2) The physics parameter regime of the plasma is characterized by several special frequencies. For the plasma in the standard operating conditions, we have

$$f_{ci} = \frac{\omega_{ci}}{2\pi} \simeq 5 \text{ MHz},$$

$$f_{de} = \frac{\omega_{de}}{2\pi} \simeq 5 - 7 \text{ MHz},$$

$$V_A/L \simeq 20 \text{ MHz},$$

$$\gamma_{MHD} \simeq 5\text{MHz}.$$

Here $\omega_{ci} = \frac{eB}{m_i}$ is the ion cyclotron frequency, $\omega_{de} = \frac{1}{\tau_l}\int \frac{dl}{|v_\parallel|}\nabla\theta \cdot \frac{\vec{b}}{qB} \times [\mu\nabla B + m\gamma v_\parallel^2 \vec{\kappa}]$ is the bounce averaged hot electron drift frequency with $\tau_l \equiv \int \frac{dl}{|v_\parallel|}$, $V_A = B/(\mu_0 n_i m_i)^{1/2}$ is the Alfven velocity, and $L \simeq 50$ cm is the scale length of the plasma. The MHD growth rate γ_{MHD} is given by

$$\gamma_{MHD}^2 = \frac{\int \frac{dl}{B}[\frac{\sigma}{\tau}\frac{\partial P_\perp}{\partial \psi} + \frac{\partial P_\parallel}{\partial \psi}]\kappa_\psi}{\int \frac{dl}{B}\frac{m_i}{B^2} \mid \nabla\theta \mid^2 n_i},$$

with κ_ψ defined by $\vec{\kappa} \equiv \kappa_\psi \nabla\psi + \kappa_\theta \nabla\theta$.

(3) On a time scale long compared with the particle drift time, the plasma on each drift surface has the same equilibrium distribution function. This results from the fact that the particles are drifting around the axis at speeds proportional to their energies. If the burst rate is lower than the hot electron drift frequency, the hot electron distribution function is uniform on a drift surface at the beginning of each burst. When the plasma becomes microunstable on one field line, the instability will occur simultaneously on all the field lines on that drift surface. Thus we expect the mode to have a drift layer structure.

(4) If curvature driven hot electron modes occur, the fluctuation frequency will be on the order of the hot electron drift frequency. In a long-thin system the functional dependence of the drift frequency can be roughly estimated to be:

$$\omega_{de} \sim \frac{\epsilon}{qrB} \vec{\kappa} \times \vec{b} \sim \frac{\epsilon}{B}.$$

The drift frequency changes mainly with the hot electron temperature. The variation of magnetic field B is not more than 20 – 30 percent since the plasma is generated by resonant heating at a fixed frequency, which occurs at a constant magnetic field.

(5) Experimentally the characteristic frequencies and the spatial correlation of the fluctuations are measured. The time history of the RF emission and the magnetic fluctuation is an indication of whether an instability is due to macro- or micro-instability. If the plasma is microunstable, the microinstabilities occur and drive the plasma out along magnetic field lines. One will first observe the RF emission from the plasma, followed by a burst of hot electrons streaming out to the end loss plates within 10 ns. The magnetic fluctuation at the MHD growth rate or at the hot electron drift frequency will develop following the microinstability when the plasma tries to adjust itself. If the plasma is MHD unstable it will first move spatially and result in diamagnetic fluctuations. As the plasma fluctuation reaches a certain level, microinstability

and plasma end loss are triggered. The initial instability growth rate, which is on the order of the MHD growth rate, will be about 5 MHz. The time resolution of the diagnostic system is sufficient for us to discriminate these time differences.

5.3 Experimental Results

5.3.1 Slowly Growing Mode

The slowly growing mode is characterized by magnetic fluctuations in the 10 - 20 MHz range. The signal sometimes correlates with the net current, but it has no correlation with the RF fluctuations. The mode is observed only when the neutral gas pressure is above $5 - 6 \times 10^{-7}$ Torr, and its occurrence rate increases with the gas pressure. A typical signal of this type of instability is shown in Fig. 5.5.

When the end loss fluctuation does coincide with the slowly growing instability, its frequency is the same as the magnetic fluctuation frequency. The end loss fluctuations measured at the horizontal and vertical symmetry planes are symmetric about the magnetic axis. The correlation between the detectors on the north end plate is shown in Fig. 5.6. We see that the signals at the same radius but opposite sides of the axis are precisely correlated in phase and frequency. But at different radii the correlation is poor. This indicates that if the mode is propagating, it must propagate mostly azimuthally along a drift surface with an even mode number. However, no clear evidence of the mode propagation has been obtained. Because the growth rate of the burst is slow compared with the mode frequency, it is unclear at which radius the bursts start.

An interesting property of the slowly growing mode is that the frequency of the mode is dependent on the magnetic field strength and the time during a burst. In each burst, the fluctuation starts at a high frequency which decreases as the instability develops. The frequency drops by about one fourth by the time the instability reaches

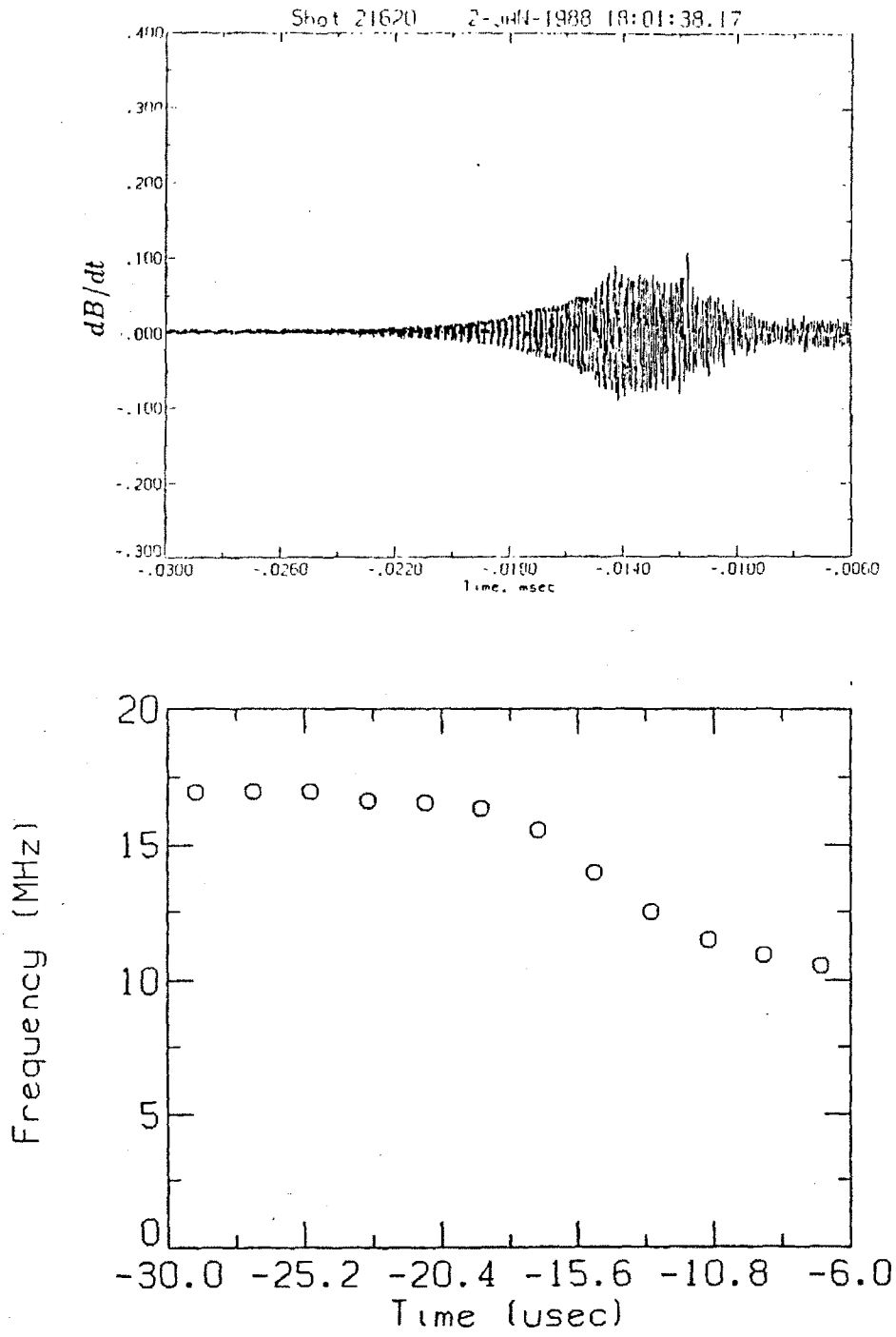

Figure 5.5: (a) A typical signal of the slowly growing mode. (b) The frequency of the coherent oscillation as a function of time during the burst.

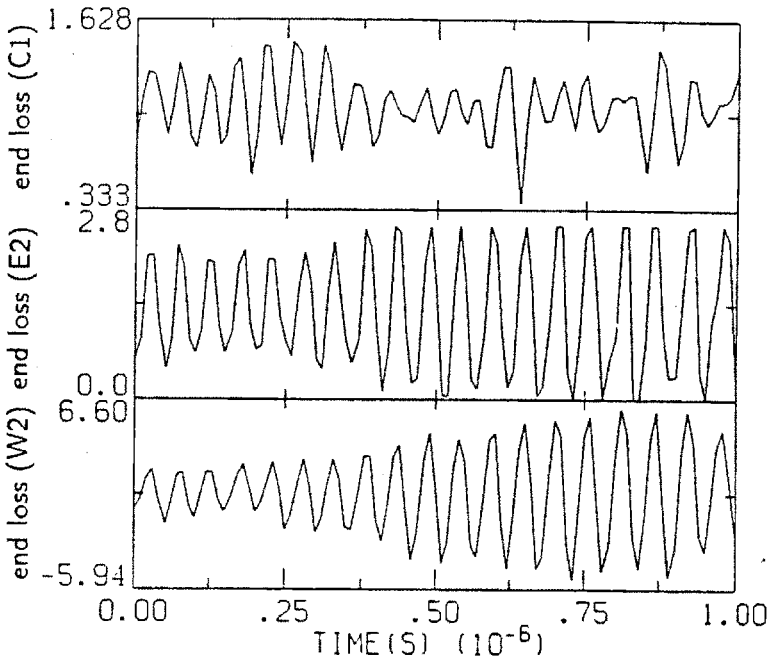

Figure 5.6: Correlation between the net current detectors during a slowly growing fluctuation. The net currents correlate well at symmetric positions but not at different radii.

its peak amplitude. When the instability almost goes away, the frequency is reduced by more than a half. For example, the instability in Fig. 5.5 starts from 17 MHz. It reduces to 13 MHz at the peak amplitude and keeps decreasing to about 10 MHz until the next short burst starts. The instability frequency also changes with the vacuum magnetic field strength. Figure 5.7 shows the oscillation frequencies measured at the beginning of the fluctuations in a magnetic field scan. It varies from 15 to 26 MHz when the magnetic field is changed from 2.6 to 3.4 kG. The scintillator probe which measures only the hot electron end losses shows that there is no hot electron end loss associated with the slowly growing mode. The magnetic probe data shows that the loss of the plasma diamagnetism is on the order of $\delta B/\tilde{B} \leq 10^{-3}$.

Because this instability always occurs in the absence of the RF emission, and it is not associated with hot electron end loss, the magnetic fluctuations must be due

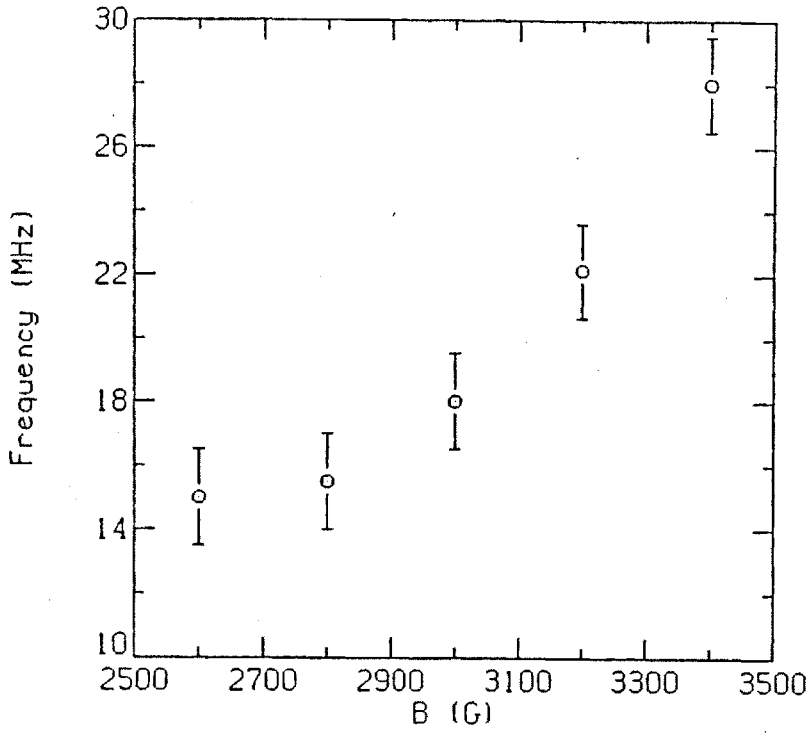

Figure 5.7: The frequency of the slowly growing mode as function of the magnetic field. The frequency is measured at the onset of the instability.

to changes in the plasma spatial profile and thus are macroscopic instabilities. The spatial correlation of the mode shows that the perturbation has a drift layer structure and an even mode number. The mode frequency is about four times higher than the hot electron drift frequency, which is expected for a wave with an azimuthal mode number $m = 4$. However, the decrease of the mode frequency as function of time cannot be explained by a hot electron curvature driven mode. The decrease in mode frequency suggests that either the mode frequency is proportional to the drive of the mode such as the plasma gradient, or that the wave is convectively propagating in the radial direction and the frequency changes as the result of the plasma temperature non-uniformity. We have no experimental data to determine which process is taking place at this time. The increase of mode frequency with the magnetic field is also inconsistent with the curvature driven mode. The hot electron temperature change is

within 20 percent during the magnetic field scan while the mode frequency is changed by nearly a factor of 2. Further experimental and theoretical analysis is needed in order to construct a physical explanation of the instability.

5.3.2 Fast Growing Mode

Two typical fast growing instabilities are shown in Fig. 5.8. Unlike the slowly growing mode there is always a large RF emission burst which correlates with the magnetic and the end loss fluctuations. The end loss current fluctuations measured at three radial locations indicate that the instability also has a radial layer structure. Near the magnetic axis, the end loss is characterized by a single burst of electrons at the onset of the instability. At larger radius, the signal oscillates for a much longer time and is symmetric about the magnetic axis on each symmetry plane. The scintillator probe measurement shows that the end loss current during these instabilities includes a large number of energetic electrons. Usually the end loss starts from the field lines at small radius ($r \leq 2$ cm at the midplane). The plasma diamagnetism drop during these instabilities is usually larger than the drop during the slowly growing mode. But it is still less than one percent of the total diamagnetism. The RF signal and the magnetic fluctuations normally appear within 200 ns, either one preceding the other. The magnetic signal is always in the frequency range between 4 and 8 MHz and does not change with the magnetic field, plasma density, hot electron temperature, or the different ion species. The end loss signals have a more complicated spectrum. The spectrum normally includes the fundamental and the second harmonic of the magnetic field fluctuation frequency, and sometimes includes the components in the 15 MHz regime similar to the slowly growing mode.

But all the other features such as mode frequency, fluctuation level, and the azimuthal correlations are the same.

The correlation between the RF emission and the hot electron end loss bursts

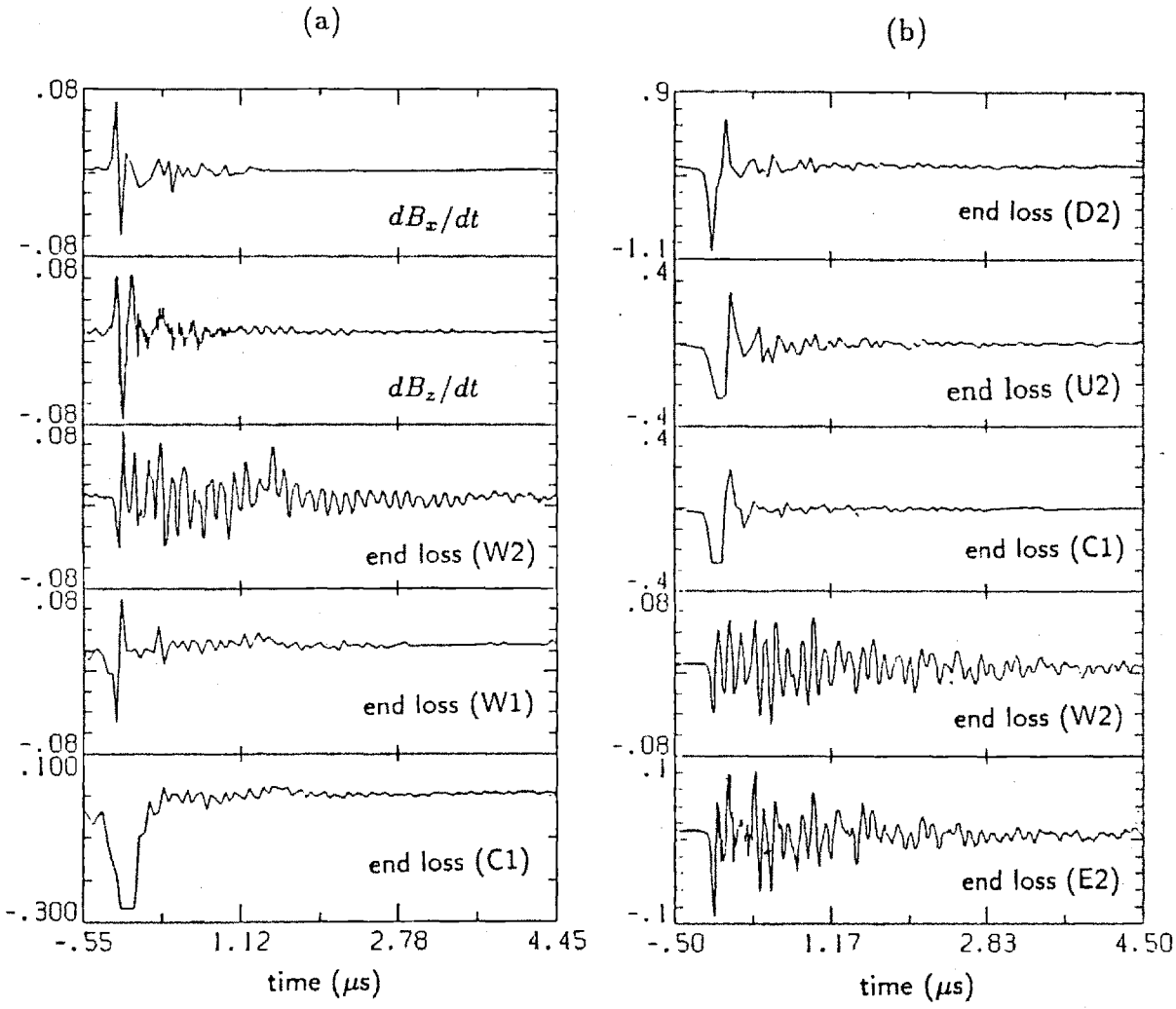

Figure 5.8: Typical fast growing fluctuations. (a) Correlation between magnetic fluctuation and end loss currents. (b) Correlation between end loss detectors. The data show that the the instability correlates well on the field lines symmetric about the magnetic axis but not at different radii.

shows that the instability is microscopic. However, the plasma fluctuation reveals many macrostability properties of the plasma. In the bursts where the RF emission occurs before the diamagnetic fluctuations, the instability is clearly triggered by the anisotropy of the electron distribution function. But when the magnetic fluctuation occurs before the RF emission and the end loss, the instability is more likely being triggered by a macroinstability. However, the subsequent mode behavior such as mode frequency, fluctuation level, and the azimuthal correlations are very similar in the two cases. This suggests that the instability is quickly taken over by the microinstability activities, indicating that the whistler instability in Constance is more violent than the fluid instability and that it can change the equilibrium quickly by driving hot electrons out of the machine. The short duration of the mode shows that the plasma can reach a new equilibrium within a couple of microseconds after the microinstability occurs, which is distinctly different from the slowly growing modes which last about ten times longer. The observation that the instability starts from the magnetic axis shows that the plasma is more unstable on the inner flux surfaces on which the resonance mirror ratios are larger.

We have also seen pure microinstabilities which are characterized by a large burst of hot electron end loss, as shown in Fig. 5.9. The hot electron end loss can persist for about 10 microseconds without triggering coherent magnetic fluctuations. It is likely that these hot electron end losses are triggered by microinstabilities while the plasma spatial profile is stable. The loss of the diamagnetism due to these microinstabilities is often even larger than the other instabilities. It confirms that the microinstability is more severe in Constance than the macroinstabilities.

5.3.3 Fluctuations throughout a Shot

Plasma parameters can vary dramatically during a shot. During the first few hundred milliseconds of the ECRH pulse, the plasma temperature scans from zero to several

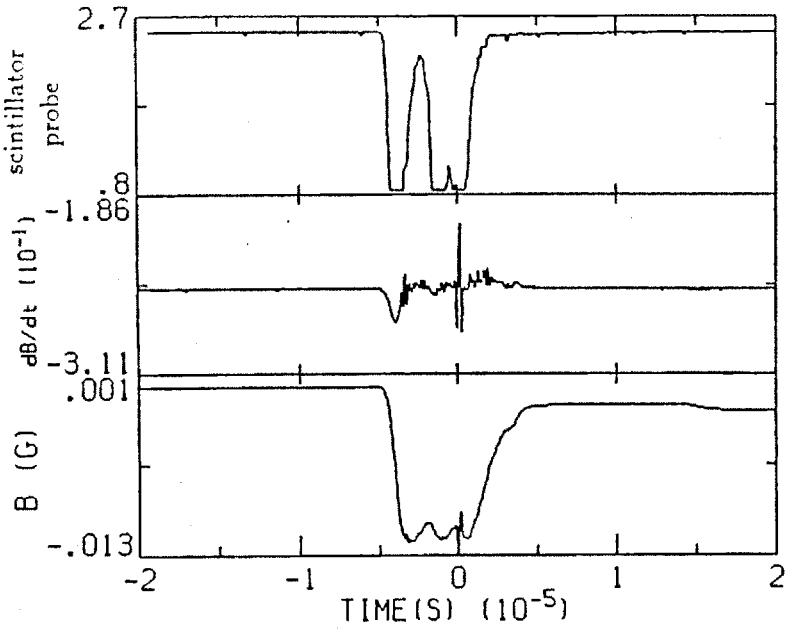

Figure 5.9: A large hot electron end loss burst driven by microinstability. The corresponding diamagnetism drop is about an order of magnitude larger than that due to the slowly growing mode, even though the coherent magnetic fluctuation is small.

hundred keV. At the ECRH turn-off, the ratio between the cold and hot electron populations changes from about 1 to about 10^{-3}. The plasma behaviors at these different parameter regimes are important for understanding the plasma stability.

Figure 5.10 shows the plasma end loss fluctuation measured at several time intervals during a shot. The bursting type instabilities start at about 2 ms after the plasma breakdown. It persists during the entire shot from the plasma build-up to the steady state. After the ECRH power is turned off, the bursts stop in about 2 ms when the cold and warm electrons are scattered into the loss cone. A number of hot electron stability theories have been developed based on the fact that the cold and hot electron populations have different responses to a given perturbation. When the two populations co-exist, the perturbed field will be dissipated by one or the other, resulting in a stable plasma when the dissipation is strong enough. As will be discussed in the next chapter, these theories normally require the cold and hot electron densities

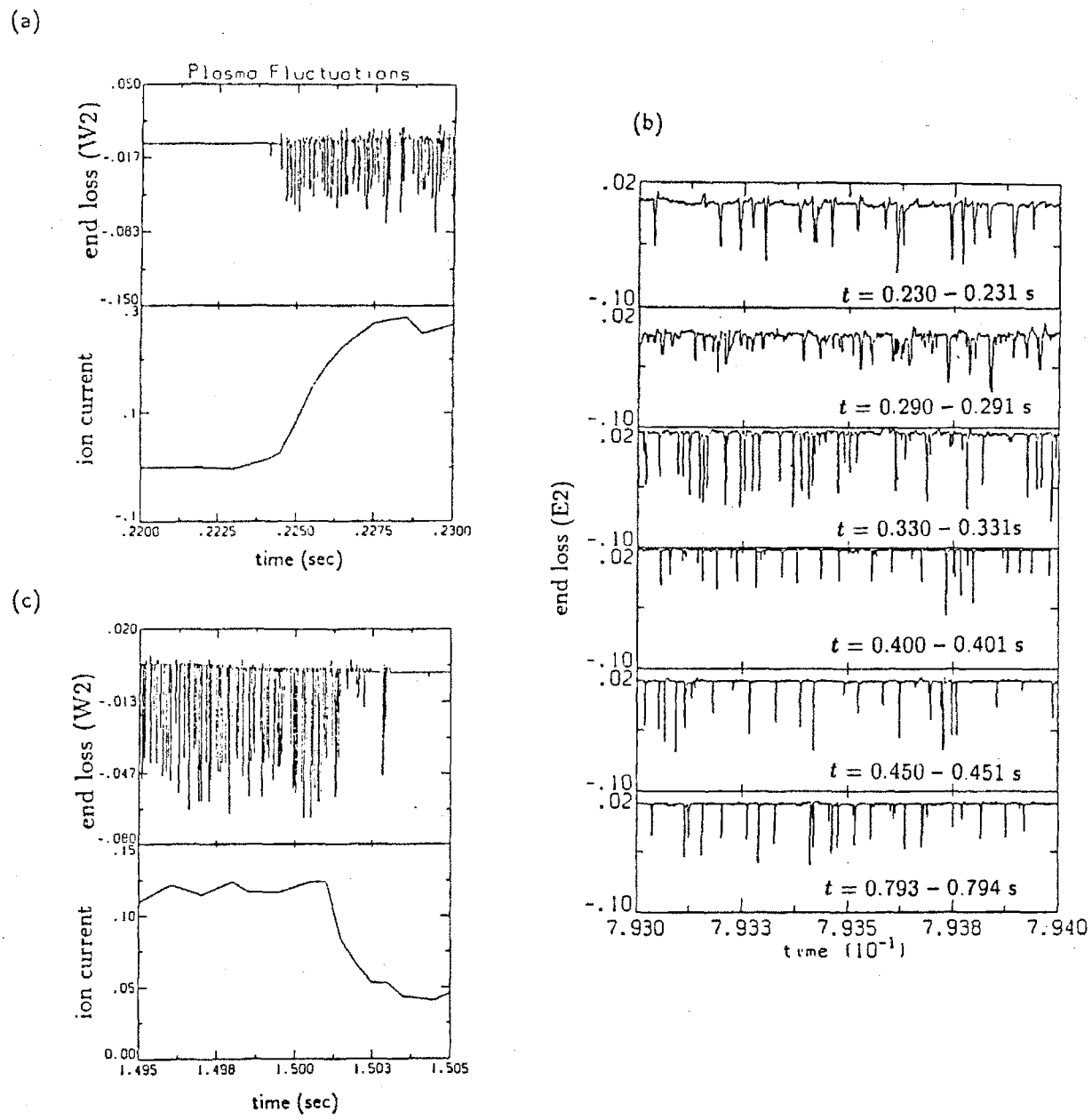

Figure 5.10: Plasma end loss fluctuations measured at several time intervals during a shot. (a) Plasma breakdown. (b) Fluctuations at six time intervals during ECRH heating. (c) After the ECRH pulse is off. The total end loss current is presented to show the timing of the plasma breakdown and the RF turn-off.

to be comparable, or at least within the same order of magnitude for stability. Such requirements have been confirmed in the previous hot electron plasma experiments in maximum-B magnetic configurations such as ELMO [Dandl, 1964] and EBT [Dandl, 1971; Hiroe, 1983]. From Fig. 2.3, however, we see that the hot electron plasma in Constance decays quietly with a time constant of order 2 seconds, in comparison with the MHD growth time of about 0.2 microseconds. During the decay, the density ratio of cold electron to hot electron populations scans from about 1:1 to 10^{-3}:1 without triggering any instability. Hot electron confinement on the order of pseudo-classical diffusion time scale was also observed in afterglow plasmas of other experiments such as ELMO which had a magnetic configuration very similar to Constance [Haste and Lazar, 1973], and in the FM-1 experiment when hot electrons were generated in the "good" curvature region of the spherator [Freeman, 1971]. This demonstrates that the stability of the hot electron plasma is not dependent on the cold electron population. It should be pointed out that the bursts are mostly whistler instabilities and may not related to the MHD type plasma fluctuations. But the fact that the plasma is stable at low cold electron density shows the plasma is not stabilized by the cold electrons.

A theoretical analysis using a simplified geometry has predicted an instability associated with the reversal of the magnetic gradient [Berk and Zhang, 1987]. Based on the best fit model equilibrium pressure profile we have shown that the magnetic field gradient reversal is expected to occur at a plasma beta of about 25 percent in the standard operating conditions. Figure 5.10(b) showed the end loss current fluctuations measured when the plasma beta increases from a few to 30 percent. The amplitude and the rate of the bursts do not change much during this time. No particularly strong instability is observed when the plasma beta scans across this regime.

Stable plasmas are also observed when the cold electron population is reduced during the ECRH pulse. Figure 5.11 shows a shot in which the gas puff is stopped before the RF turn-off. Cold electron density is reduced because its source is cut off. The end loss fluctuation level shows that the fluctuation reduces as the cold electron density decreases and the plasma bursts stops within 100 ms after the gas is off.

5.3.4 Is the Plasma Hollowness Limited by Stability Conditions ?

In the previous sections, we have shown that the Constance plasma equilibrium is hollow and essentially macroscopically stable. However, there remain questions such as whether the hollowness of the plasma pressure profile is determined by the marginal stability conditions, or it is just because of the given plasma heating profile and transport. Experimentally this question can be answered by measuring if more hollow plasma profiles may be produced.

The hollowness of the plasma profile can be perturbed by inserting a skimmer probe along the axis or by dropping small metal spheres into the plasma. It was shown in Chapter 4.4 that nearly 100 percent hollow plasmas can be generated by using axial skimmer probes. However, enhanced plasma density fluctuations have been observed when the probe was placed close to the midplane. The existence of the metal probe also makes the explanation of the plasma stability more difficult. A more decisive measurement is from the experiment in which stainless steel spheres (diameter $\simeq$ 2 mm) are dropped from the top of the machine. When a metal ball is dropped into the opening of the "C" shaped plasma, it eliminates the hot particles on the inner field lines. Particles at larger radii are drifting along the baseball seam orbits and will not be hit directly by the ball. The visible light images of the plasma show clearly that the plasma becomes much more hollow after the stainless ball went through. This plasma stays quiescently and can be observed for more than a hundred

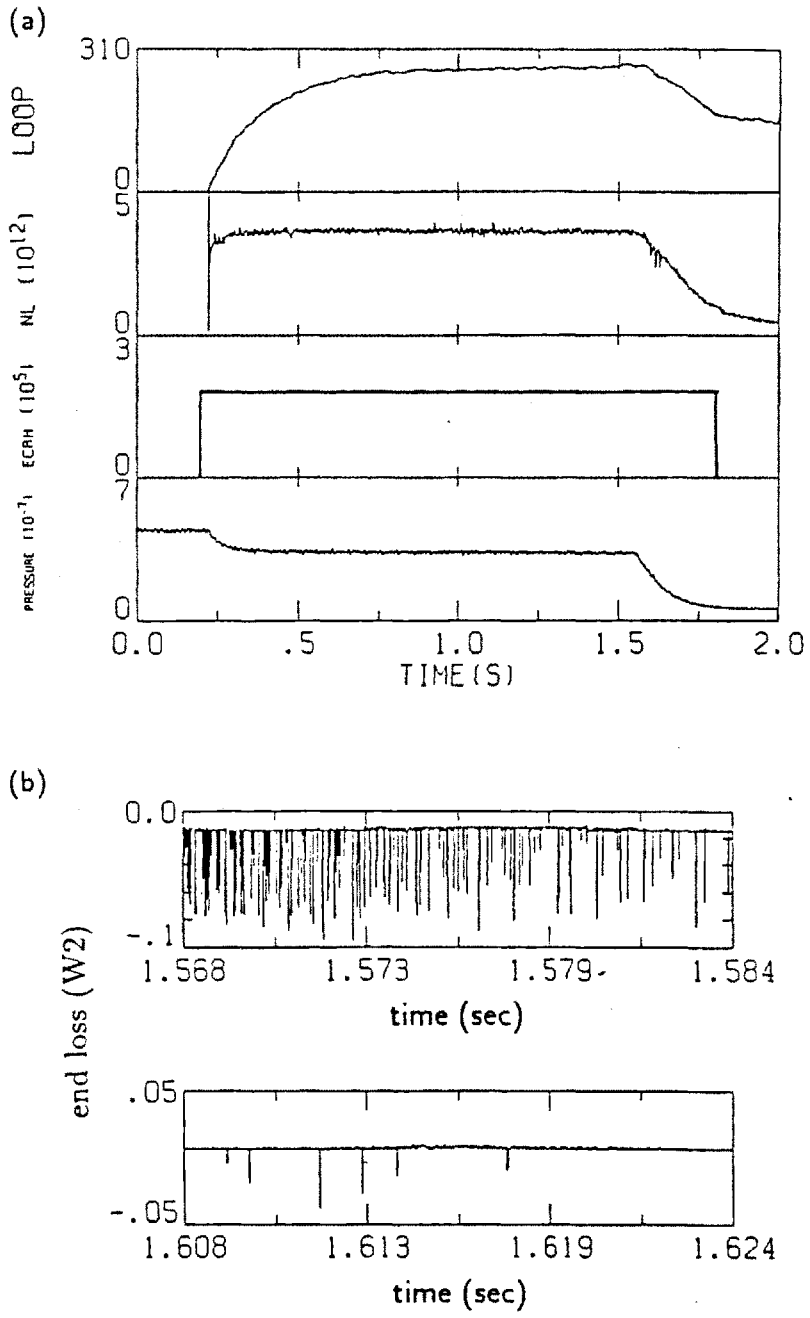

Figure 5.11: Plasma fluctuation decreases when the background gas pressure is reduced during the ECRH pulse. (a) Equilibrium signals. (b) End loss fluctuation after the gas-feed is turned off. The fluctuations stop within 100 ms after the gas cutoff (at $t = 1.5$ sec) when the cold electrons are gone.

milliseconds. Other diagnostics also show that there are no strong fluctuations once the ball has passed through. Therefore the hollowness of the plasma equilibrium profile is not limited by the stability conditions.

5.4 Summary

The experiment shows that low level micro- and macro-instabilities co-exist in the Constance B mirror. The frequency of the fluid type instability is above the ion cyclotron frequency, and it decreases as a function of time during a burst. The instabilities correlate well around each drift layer but not at different radii. The microinstabilities are more severe than the fluid instabilities in expelling hot electrons and reducing the total plasma diamagnetism. The plasma relaxation time after the microinstabilities is on the order of a few microseconds. The plasma fluctuations disappear when both the cold and warm electrons are lost from the system.

Overall, the hollow plasma equilibrium is macroscopically stable. The duration of the equilibrium is many orders of magnitude longer than the MHD growth time, even though low level fluid type instabilities do occasionally occur. The hollowness of the plasma equilibrium profile is not limited by the stability conditions.

Chapter 6

Stability Analysis of the Observed Equilibrium

This chapter presents an analysis of the stability properties of the hollow equilibrium profile identified in the experiment. In the previous chapters it has been shown that the hollow plasma equilibrium in Constance is essentially macroscopically stable. In this chapter, we will first summarize the stability properties of the plasma, and then compare them with the predictions of fluid theory and of hot electron stability theories. The emphasis is on understanding why the plasma is stable. We will point out the difference between the experiment and the theories, and discuss some special effects associated with the plasma stability in a minimum-B mirror.

6.1 MHD Stability Properties of the Plasma

The Constance B plasma is characterized by hot electrons confined in a hollow, baseball seam profile. Stable equilibria are observed for all the experimental conditions in which the equilibria have been measured, ranging from magnetic fields of $B_0 = 2.6 - 3.75$ kG, ECRH power = 5 W $-$ 4 kW, and neutral gas pressure = $2 \times 10^{-7} - 5 \times 10^{-5}$ Torr.

Many physics parameter regimes are covered by these experiments:

(1) The characteristic of MHD-like instabilities is considerably altered theoretically if

the hot electron curvature drift frequency is comparable to or larger than the MHD growth rate [Berk, 1975],

$$\omega_{de} \geq \gamma_{MHD}, \tag{6.1}$$

where ω_{de} is the bounce averaged hot electron drift frequency and γ_{MHD} is the MHD growth rate. In the Constance B magnetic field, the drift frequency is about 7 MHz for 400 keV electrons. The MHD growth rate is about 5 MHz for a plasma at this temperature. Because $\omega_{de} \propto T_{eh}$ and $\gamma_{MHD} \propto T_{eh}^{1/2}$, the hot electron drift frequency becomes lower than γ_{MHD} for T_{eh} below 200 keV. Stable plasmas are observed in conditions with ω_{de} both below and above γ_{MHD}.

(2) The Constance plasma is observed to be stable for conditions in which either $\omega_{de} \gg \omega_{ci}$ or $\omega_{de} \leq \omega_{ci}$, suggesting that the coupling of curvature driven instabilities to the ion cyclotron motion is not significant. The cyclotron frequency for hydrogen ions is about 5 MHz in the machine. The condition $\omega_{de} \gg \omega_{ci}$ is obtained in the shots with argon or xenon plasmas. Figure 4.21 showed some data from an argon discharge. During the ECRH pulse, the steady state hot electron temperature is about 450 keV, resulting in $\omega_{de} \sim 40\ \omega_{ci}$ for the singly charged argon ions. The other extreme, $\omega_{de} \ll \omega_{ci}$, is obtained in shots with low ECRH power. Figure 4.20 showed the data measured in a 100 W hydrogen shot together with a visible light photograph taken during this shot. The plasma diamagnetism is about 4 percent and the electron temperature is on the order of 30 - 50 keV. Thus the electron drift frequency is nearly an order of magnitude lower than the ion cyclotron frequency. The plasma is observed to be hollow and stable in both cases.

(3) The plasma is stable under conditions in which the hot electron fraction ($\alpha \equiv n_{eh}/(n_{eh} + n_{ec})$) ranges from 0.5 to 0.99. Theoretically, the stability of a hot electron plasma against curvature driven modes has often been attributed to the presence of a cold electron component. It has been shown that hot electron interchange modes can

be stabilized by cold electrons in frequency regimes where either $\omega_{de} << \omega_{ci}$ [Krall, 1966] or $\omega_{de} \geq \omega_{ci}$ [Berk, 1975]. However, the MHD stability properties of the hot electron plasma in Constance are observed to be essentially independent of the cold electron population.

(4) The use of high beta hot electron plasmas to modify otherwise unstable magnetic field geometries is a major motivation for the study of hot electron plasmas. It has been proposed that hot electrons be used to reverse the magnetic field gradient and to thereby change the stability properties of the core plasma (EBT) or of the plasma in adjacent cells (STM) [Lazar, 1980]. Theoretical work [Berk and Zhang, 1987] has predicted a stability threshold upon drift reversal. These theoretical predictions suggested that the plasma stability properties should change upon drift reversal. The experimental data shows no significant changes when we raise the plasma beta sufficiently to reverse the particle drift as interpreted through the modelling discussed in chapters 3 and 4.

(5) Finite Larmor radius effects do not play a significant role in the stability of the plasma because the plasma is stable at low power discharges and early in shots when the plasma temperature is low. For relativistic electrons

$$a_L = \frac{\gamma m_0 v}{eB} = \frac{m_0 c}{eB}\sqrt{\gamma^2 - 1}.$$

The Larmor radius for a 400 keV electron is 0.72 cm. In the high field shots where the plasma scale length is 3 – 4 cm, this Larmor radius is significant. In the shots with a midplane magnetic field of 2.6 or 2.8 kG, the plasma radial scale length is 10 cm or more. But the plasma equilibrium is still hollow while the FLR effect does not have a significant role. Also, the FLR effect is small when the electron temperature is low. The Larmor radius is 0.15 cm for a 50 keV electron. Thus early in the shot when the electron temperature is below 50 keV, the plasma stability cannot be argued to be due to the electron FLR effect. The ion FLR effect is also insignificant. The Larmor

radius for a hydrogen ion of 60 eV is only about 0.2 cm.

(6) The line tying effect is not important for the stability in Constance. Because of the use of the large fan tanks, the plasma is separated from the end wall by about 1.5 m. By shutting off the gas puff during the plasma decay, the plasma density outside the mirror peak can be reduced to several order of magnitudes below the confined hot electron density, and the stability of the plasma has never been observed to be affected.

(7) The mirror mode stability condition is given by [Thompson, 1962]

$$\tau \equiv 1 + \frac{\mu_0}{B}\frac{\partial P_\perp}{\partial B} > 0.$$

Beyond this limit, MHD equilibrium becomes an ill-imposed problem [Grad, 1967]. The most anisotropic plasma profiles in Constance are obtained in the high magnetic field shots. When the midplane magnetic field is 3.6 kG, the vacuum field ECRH resonant surface extends only to z=6.5 cm and the resonance mirror ratio is 1:1.04. Without the plasma diamagnetic depression, the mirror mode limit is about $\beta_{peak} = 0.08$. However, the peak plasma beta is measured to be about 50 percent in the experiment. In such a high beta plasma, the magnetic field geometry is strongly modified by the plasma currents and the diamagnetic depression must be taken into account. To the first order approximation in beta, numerical calculations show that a 600 Gauss diamagnetic field is generated at the peak pressure position. This pushes the beta limit to about 40 percent, which is very close to the required diamagnetic depression to have the mirror mode limit satisfied. Thus a nonlinear analysis is needed to determine if the stability condition is violated. When the mirror mode beta limit is so closely approached, one may expect particle adiabaticity loss or some turbulence to occur. The only experimental evidence related to this is the plasma radial expansion observed under such conditions. However, it is more reasonable to believe that the expansion is due to plasma diamagnetism rather than the loss of adiabaticity because

the expansion starts early in a shot before the mirror mode beta limit is reached. It is not clear at this point if the plasma beta is limited by this stability condition.

6.2 Theoretical Limitations for Plasma Stability

We consider now in some detail the theoretical analysis of the stability of the Constance plasma.

6.2.1 MHD Interchange Mode

MHD theory predicts curvature driven interchange instabilities will occur when the plasma pressure gradient is in the same direction as the vacuum magnetic field gradient. Even through the MHD theory does not apply to the Constance B plasma in all parameter regimes since it assumes $\omega_{de} \ll \gamma_{MHD}$, we will first analyze the plasma stability to fluid theory to show that the compressibility effect is a significant stabilizing term within the context of MHD theory for a hollow plasma in a minimum-B mirror.

In the hydromagnetic fluid model, the energy variation resulting from changing two adjacent flux lines is [Rosenbluth and Longmire, 1957]

$$\delta W = \gamma \delta P \delta V - P(\delta V)^2. \tag{6.2}$$

Here $\gamma \equiv \partial \ln P / \partial \ln \rho$ is the first adiabatic exponent, P the plasma pressure, and V the volume of the magnetic flux tubes in discussion. In a quadrupole magnetic mirror, this relation can be expressed in the limit of high mode numbers as [Berk and Lane, 1983]

$$\begin{aligned} \Delta W \;=\; & \int \frac{dl}{B}\phi^2 \left[-\left(\kappa_\psi - \frac{\lambda}{l}\kappa_\theta\right) \frac{D}{D\psi}(P_\perp + P_\parallel) \right. \\ & \left. + \frac{B^2}{\mu_0}\left(\kappa_\psi - \frac{\lambda}{l}\kappa_\theta\right)^2 \left(\sigma + \frac{3}{2}\beta_\parallel - \frac{(1-\beta_\parallel/2)^2}{(1+\beta_\perp)}\right)\right], \end{aligned} \tag{6.3}$$

where $\beta_{\perp,\parallel} \equiv 2\mu_0 P_{\perp,\parallel}/B^2$, λ and l are defined by $\vec{k} = (\partial S/\partial\psi)\nabla\psi + (\partial S/\partial\theta)\nabla\theta \equiv \lambda\nabla\psi + l\nabla\theta$, with $S(\psi,\theta) \equiv$ eikonal. The first right hand term in Eq. (6.3) is negative when the pressure gradient and the field line curvature are in the same direction, which is the drive for interchange instability. The second term, which represents the compressibility effect, is proportional to κ^2 and is always positive when the plasma pressure is non-zero. In a simple mirror where the plasma is unstable at the plasma edge, the compressibility term is not important because the plasma pressure is near zero there. However, the situation is different for a hollow plasma profile in a minimum-B mirror since the unfavorable pressure gradient is near the axis where the pressure is finite. The contribution of the compressibility term allows the plasma to be still stable even when the plasma is slightly hollow. We have calculated the energy variation, δW, given by Eq. (6.3) to determine the marginal stability condition. Figure 6.1 shows the energy variation as a function of plasma hollowness calculated on a field line with midplane radius of 4 cm at the horizontal symmetry plane. The accuracy of the calculated results is mainly limited by the omission of the finite beta effect which changes the magnetic curvature. The induced error is on the order of 10 percent for a plasma with a beta of 30 percent. The result shows that ΔW changes sign at a hollowness of about 20 – 30 percent. Thus the compressibility can stabilize a plasma with a hollowness of about 20 percent. The effect of the compressibility term is reduced when the ratio of R_c/R_p is increased, which occurs if the plasma is decreased in size by increasing the magnetic field. When the midplane magnetic field is 3.6 kG, the marginally stable hollowness becomes 6 percent. Experimentally the plasma pressure hollowness is measured to be 50 % or more in the 3 kG shots, and it is about the same when the magnetic field is increased up to 3.6 kG. We conclude that the compressibility is an important stabilizing effect in the context of MHD theory but it cannot account for the plasma stability even if MHD theory were applicable to

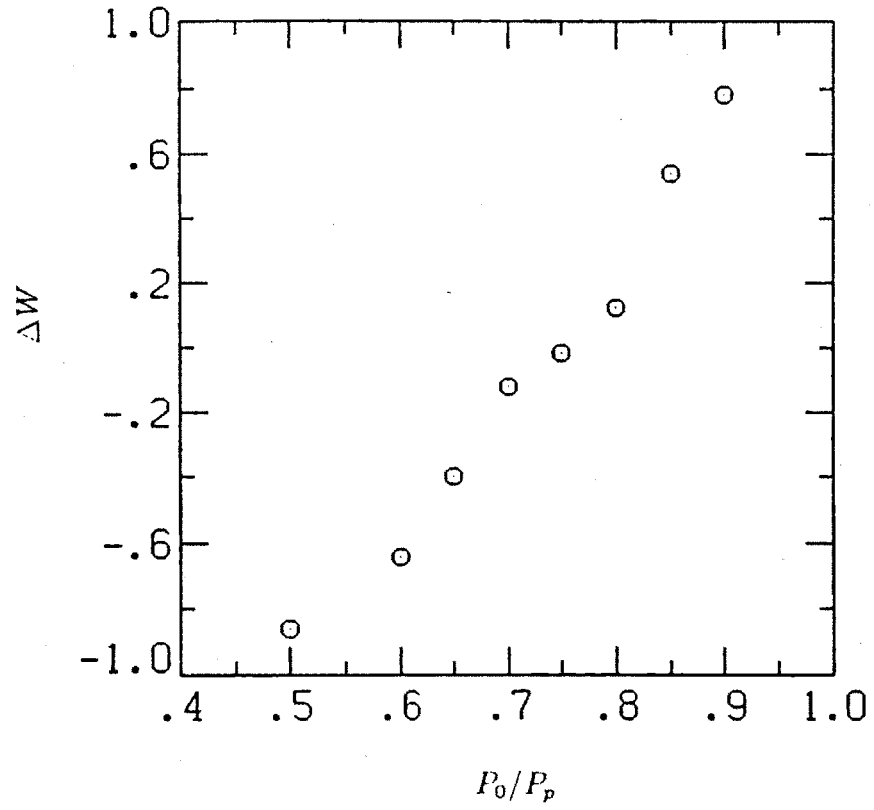

Figure 6.1: Energy variation as a function of the plasma hollowness at z=4 cm at the horizontal symmetry plane.

the plasma.

6.2.2 Hot Electron Interchange Instability

The fluid analysis above assumed that $\gamma_{MHD} \gg \omega_{de}$. Since this is only for a part of the Constance parameter regime, we consider now a kinetic theory in which $\omega_{de} \sim \gamma_{MHD}$ appropriate for an ECRH generated plasma which contains a magnetically confined hot electron population and an electrostatically confined background plasma.

The theoretical analysis has been done in several parameter regimes.

(1) Hot electron plasma stability in the presence of a cold plasma was first analyzed in the limit of frequencies much less than the ion cyclotron frequency. Under the conditions $T_e \gg T_i$ and $T_{||} = T_{\perp}$, the eigenvalue equation for the interchange mode

in a slab geometry is given by [Krall, 1965, 1966]:

$$\omega = \frac{-kv^2}{4Q\Omega_i} \cdot \left\{ \frac{1}{R_p} + 2\frac{T_e}{T_i}\frac{Q}{R_c} \pm \sqrt{\left(\frac{1}{R_p} + 2\frac{T_e}{T_i}\frac{Q}{R_c}\right)^2 - \frac{16}{R_c}\left(\frac{1}{R_p}\right)\frac{T_e}{T_i}\frac{Q}{k^2 v_i^2/\Omega_i^2}} \right\}, \quad (6.4)$$

where $Q = 1 + n_{ec}/n_{eh} + B^2/\mu_0 n_{eh} m_i c^2$, R_c is the radius of curvature, $R_p = (dn_{eh}/n_{eh}dr)^{-1}$, and $k = \mid \vec{k} \mid$ is the magnitude of the wave vector. In the limit

$$\frac{T_e}{T_i} \gg \frac{R_c}{R_p},$$

the stability condition becomes

$$[1 + (n_{ec}/n_{eh}) + (B^2/\mu_0 n_{eh} m_i c^2)]\frac{T_e}{T_i} > 4\left(\frac{R_c}{R_p}\right)\frac{\Omega^2}{k^2 v_i^2}. \quad (6.5)$$

For the Constance B plasma parameters, $B^2/\mu_0 n_{eh} m_i c^2 \sim 0.003$ and can be neglected. We can rewrite the stability condition as

$$\alpha \equiv \frac{n_{eh}}{n_{ec} + n_{eh}} < \frac{m_i}{4m_e}\frac{R_p}{R_c} a_{eh}^2 k^2 \quad (6.6)$$

where a_{eh} is the hot electron Larmor radius. For $R_p/R_c = 0.2$, the condition can be written as $\alpha < (9.6 a_{eh} k)^2$. This relation shows that the plasma is more stable against short wavelength modes. If $a_{eh}k > 0.105$, the mode will be stable independent of the cold electron fraction. The longest wavelength modes in Constance can have $k \simeq (6\ \text{cm})^{-1}$ in the standard shots. For a hot electron temperature of 400 keV, the stability condition is always satisfied. However, at shots with lower magnetic field or lower hot electron temperature, the stability limit can be violated. In the 2.6 kG shots, the maximum allowed modes may have $k \simeq (10\ \text{cm})^{-1}$. The corresponding stability condition becomes $\alpha \leq 0.5$. This is satisfied during the steady state of the ECRH pulse but not in the afterglow. At lower hot electron temperature with smaller a_{eh}, shorter wavelength modes can go unstable. For a hot electron temperature of 50 keV in a 3 kG magnetic field ($a_e = 0.152$ cm), the hot electron fraction is limited to $\alpha \leq 0.1$ for modes with $k = (5\ \text{cm})^{-1}$. The data shown in Fig. 4.20 indicates that

the hot electron fraction in such a shot is at least 20 - 30 percent before the RF is off, and it is about 1 in the afterglow. We conclude that the stability condition (6.5) can be violated in some experimental conditions. However, we must mention that the plasma fluctuations in these experiments are observed to be mainly in the frequency regime near and above the ion cyclotron frequency, not in the regime $\omega \ll \omega_{ci}$. We thus now consider the effect of coupling to the ion cyclotron motion.

(2) Radially localized curvature-driven hot electron instabilities for frequencies comparable to or larger than the ion cyclotron frequency have been analyzed in a slab model. The dispersion relation for electrostatic modes is [Berk, 1975]

$$1 - \frac{\omega_{pi}^2}{\omega^2 - \omega_{ci}^2}\left(1 + \frac{\omega_{ci}\delta}{\omega}\right) - \frac{(1-\alpha)\omega_{pi}^2\delta}{\omega\omega_{ci}} - \frac{\alpha\omega_{pi}^2}{k_y^2 v_h^2}\frac{m_i}{m_e} I_h(\omega) = 0, \tag{6.7}$$

where

$$I_h = -\frac{v_h^2}{n_e(x)}\int d^3v \left(k_y v_D \frac{\partial F_h}{\partial \epsilon} - \frac{k_y}{\omega_{ce}}\frac{\partial F_h}{\partial x}\right) J_0^2\left(\frac{k_y\sqrt{\mu B}}{\omega_{ce}}\right)(\omega - k_y v_D)^{-1},$$

and $\delta = (k_y R_p)^{-1}$, $\vec{v}_D = (v_\parallel^2 + v_\perp^2/2)/(\omega_{ce}R_c)\hat{e}_y$, and α is still the hot electron fraction. Under the condition $R_p/R_c \ll 1$, the dispersion relation becomes

$$\frac{\omega_{ci}^2}{\omega_{pi}^2} - \frac{(1+\delta/x)}{x^2-1} - \frac{\delta(1-\alpha)}{x} - \frac{\delta\alpha}{x+q} = 0, \tag{6.8}$$

with $x = \omega/\omega_{ci}$ the normalized frequency and $q \equiv -k_y v_D/\omega_{ci}$.

For $\frac{\omega_{ci}^2}{\omega_{pi}^2} \ll 1$, the dispersion relation becomes quadratic for the mode with $\delta = (k_y R_p)^{-1} = 1$. The stability condition is then

$$\frac{n_{ec}}{n_{eh}} \geq \frac{2}{q}\left(1 + \sqrt{1+q}\right),$$

For the Constance B parameters with T_{eh} a few hundred keV, the value of q is between 5 and 10. Taking the optimistic limit with $q = 10$, the stability condition requires

$$\alpha \leq 0.54. \tag{6.9}$$

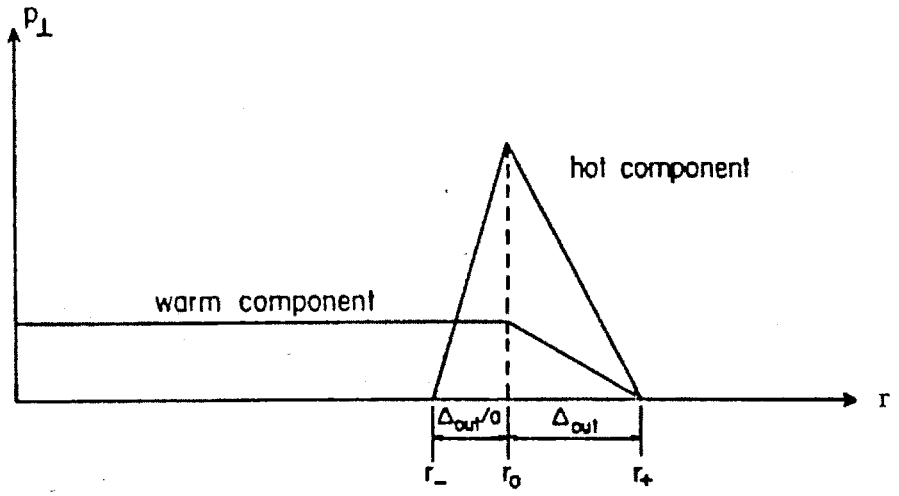

Figure 6.2: A radial pressure model used by Berk and Zhang (1987) for calculating the marginal stability condition.

This requirement is marginally satisfied in the steady state phase of the ECRH pulse but apparently not in the afterglow.

Compared with the stability criterion by Krall in the frequency range $\omega \leq \omega_{ci}$, the required cold electron fraction is larger for stability in the range of $\omega \geq \omega_{ci}$. However, Berk's theory considered only the electrostatic perturbations. The effects such as compressibility were not included. The kinetic effect from the $(\omega - \omega_{de})$ resonance term was also eliminated to simplify the analysis.

(3) Curvature driven instabilities with long radial wavelengths in the frequency regime comparable to and above ω_{ci} have been studied by Berk and Zhang (1987), with a cylindrical model in which the magnetic field lines are straight and there is a rigid embedded current to simulate the effect of curvature. This model is ideal for EBT where the magnetic field lines are mainly in the toroidal direction and the hot electrons form an annulus with the current in the azimuthal direction. It can only be qualitatively applied to Constance where the plasma profile cannot be simply modelled by a cylinder. For the plasma radial pressure profile shown in Fig. 6.2.2, the dispersion relation

for modes with radial wave length comparable to the plasma radius is expressed as

$$\frac{1+a\xi}{a\xi}\left[\frac{(1+a\xi)^2}{Q_{in}}-1\right]+\frac{1-\xi}{\xi}\left[\frac{(1+\xi)^2}{Q_{out}}-1\right]=N^2\left(\Omega_A^2(1+\Lambda_1)-\frac{\hat{\omega}^2}{1+\hat{\omega}/\hat{\omega}_{ci}}\right), \quad (6.10)$$

where

$$\begin{aligned} Q_{in} &= (1+a\xi)^2-\hat{\omega}a\xi\,[1+a\xi-\hat{\omega}\,\Gamma(\frac{\hat{\omega}}{1+a\xi})], \\ Q_{out} &= (1-\xi)^2+\hat{\omega}\xi\,[1-\xi-\hat{\omega}\,\Gamma(\frac{\hat{\omega}}{1-\xi})], \\ \Gamma_\omega &= \int_0^\infty dx\,\frac{e^{-x}}{\omega-x/[\psi(b)(1+bx)^{1/2}]}, \end{aligned}$$

and

$$\hat{\omega}=\frac{\omega}{\tilde{\omega}_\kappa}, \qquad \hat{\omega_{ci}}=\frac{\omega_{ci}}{\tilde{\omega}_\kappa}, \qquad \Omega_A=k_n v_A/\tilde{\omega}_\kappa$$

$$\xi=-\frac{P_h}{\Delta_{out}B^2\kappa_{eff}}, \qquad a=\Delta_{out}/\Delta_{in},$$

$$N^2=\frac{\tilde{\omega}_\kappa^{\,2}}{\gamma_{MHD}^2}, \qquad \gamma_{MHD}^2=-\beta_{\perp h}\left(\frac{|l|}{2r_pB}\right)v_A^2\frac{dB_{ext}}{dr},$$

$$\tilde{\omega}_\kappa=\frac{P_h cl}{n_{eh}qB^2r}\frac{dB_{ext}}{dr}, \qquad \kappa_{eff}=\frac{1}{B}\frac{dB_{ext}}{dr}.$$

Here ξ is the drift reversal parameter which exceeds unity when the magnetic field gradient is reversed. In this model the plasma is not stabilized by the cold electron component but by balancing the positive and negative dissipation from the drift resonances. It is predicted that there is an unstable "precessional layer" mode (a negative energy wave) which arises at $\xi \geq 1$ when the pressure gradient is large enough to reverse the gradient of the magnetic field. In this situation only resonances leading to the positive dissipation occur and the plasma is unstable.

The stability condition for the ξ limit is slightly relaxed when the axial plasma pressure profile variation is taken into account. The requirement becomes that the line averaged ξ should be less than unity in the particle bounce region, resulting in an increase of the maximum allowed local value of ξ from 1 to about 1.5 [Zhang, 1988].

It is shown in Chapter 4.7 that the magnetic field gradient in the hot plasma region in Constance is reversed for the model equilibrium which best fits the experimental observations. We can calculate the gradient reversal parameter using

$$\xi = |\frac{R_c}{B_v^2}\frac{\partial P_{\perp h}}{\partial r}|$$

for the measured plasma equilibrium. In the standard shot, the averaged ξ value is slightly smaller than 1 and thus satisfies the stability condition. However, in the high field shots with magnetic field above 3.5 kG, the plasma gradient is increased by about a factor of 3/2. The plasma is also confined in a region near the magnetic axis where R_c is large. The averaged ξ value is increased to above 1.5 which is beyond the stability limit. We have observed enhanced fluctuations in these high field shots. The plasma radial size is also observed to expand with the increase of the total diamagnetism. However, it is unclear if these activities are related to the "precessional mode" at this point.

6.2.3 Stabilization due to Line-tying

The stability of interchange modes has been attributed line-tying in many early mirror experiments. The line-tying effect on the hot electron interchange mode was analyzed by Gerver and Lane [1986] in the low frequency regime ($\omega \ll \omega_{ci}$). They found that the hot electron interchange modes are more effectively stabilized in the presence of line-tying than the MHD interchange modes because of the higher mode frequencies and the spreading of the hot electron curvature drift frequency.

In the limit $\omega \gg \nu_e$ (ν_e is the cold electron Coulomb collision rate), $\omega \gg \omega_{di}$ (ω_{di} the ion curvature drift frequency), and $kv_{\perp i}/\omega_{ci} \ll 1$, the dispersion relation for low frequency electrostatic flute modes in a square mirror well is expressed as

$$\omega^2 + \omega|\omega_{*i}| + \gamma_{MHD,i}^2 - \frac{\alpha\omega_{ci}\omega}{kR_p}\left\{1 - \frac{\omega}{\bar{\omega}_{deh}}Z'\left[\left(\frac{\omega}{\bar{\omega}_{deh}}\right)^{1/2}\right]\right\} + \frac{e^{\pi i/4}\omega^{3/2}\bar{\nu}_{loss}\omega_{ce}\omega_{ci}}{\sqrt{2}k^2v_{ec}^2\nu_e^{1/2}}\left(\frac{e\Phi}{T_{ec}}\right)^{1/4}\left[1 + \left(\frac{RT_{ec}}{e\Phi}\right)^{1/2}\right]^{-1} = 0. \quad (6.11)$$

Where

$$\bar{\nu}_{loss} \equiv (1-\alpha)\frac{1}{e < n_{ec} l >}\left(\frac{T_{ec}}{e}\frac{\partial J_{loss}}{\partial \Phi}\right),$$

$\omega_{*i} = -kv_{i\perp}^2/R_p\omega_{ci}$, and $\gamma_{MHD,i} \equiv -(v_{i\perp}^2 + v_{i\parallel}^2)/2R_pR_c$. The drift resonance term is contained in the Z' function. The stabilization effect is provided by the positive dissipation due to line-tying balanced against the negative dissipation which comes from the resonant denominator $(\omega - \omega_{de})$. The most unstable mode has

$$k_{crit} \simeq 0.77\left\{\frac{\bar{\nu}_{loss}^2\omega_{ci}^5 R_c}{v_{eh}^2 v_{ec}^4 \nu_e}\left(\frac{m_i}{m_e}\right)^3\left(\frac{e\Phi}{T_{ec}}\right)^{1/2}\left[1+\left(\frac{RT_{ec}}{e\Phi}\right)^{1/2}\right]^{-2}\right\}^{1/5}. \qquad (6.12)$$

Taking $\nu_e = 10^5 s^{-1}$, $\bar{\nu}_{loss} = 10^3 s^{-1}$, $T_{eh} = 350$ keV, $T_{eh} = 50$ eV, and $\frac{e\Phi}{T_{ec}} = 1$, we obtain $k_{crit} = (31\text{ cm})^{-1}$. This wavelength is too long to fit in Constance. At larger values of k, the marginal stability condition is

$$\alpha \simeq 0.62\left\{\frac{\bar{\nu}_{loss}^2 k^3 v_{eh}^6 R_p^4}{v_{ec}^4 \nu_e \omega_{ci}^2 \omega_{ce} R_c^3}\left(\frac{e\Phi}{T_{ec}}\right)^{1/2}\left[1+\left(\frac{RT_{ec}}{e\Phi}\right)^{1/2}\right]^{-2}\right\}^{1/4}. \qquad (6.13)$$

Taking $k = (6\text{ cm})^{-1}$, the hot electron fraction for the stability condition is $\alpha \leq 0.384$. This stability condition is barely satisfied during the ECRH pulse but not in the afterglow.

6.3 Some Stabilizing Effects for Minimum-B Mirrors

From the analysis of the last two sections we have seen that the stability of the Constance equilibrium cannot be fully explained by the current stability theories. There are other theories which have not been analyzed here which consider the stabilizing effects such as the FLR effect and the self-dug magnetic well by plasma current. But they can be eliminated because their conditions are not always satisfied. However, all these theories depend on simplified models which may not be satisfied in real experiment. In this section we will discuss some physical processes in a minimum-B mirror

which have favorable stabilizing effect to the plasma. The mathematical analysis of these effects will not be discussed here.

The plasma stability in Constance must be intrinsically related to the magnetic field geometry because the hollow plasma equilibria are produced in all the experimental conditions. The first effect we will discuss is the stabilization due to the radial drift of particle orbital motion in non-axisymmetric mirrors. The electron guiding center drift orbit in the Constance magnetic field has been presented in Fig. 3.11, which shows that particles drift in and out on a drift surface due to the geodesic curvature, and the width of the radial drift is on the order of one centimeter. On average, the radial drift cancels out after a bounce motion. However, the drift makes a particle no longer fixed on a single flux surface on the time scale of the bounce time, which is normally much shorter than the MHD growth rate. Therefore the adjacent flux surfaces are electrically connected in the direction of the pressure gradient. A perturbed electric field can no longer develop on one field line or one particular drift surface, and will be smeared over the radial width of the drift. The effect prevents the localized layer modes from developing. This effect is similar to the FLR effect in some respects. When the electrons and the ions are at different temperatures, their drift width will be different, resulting in the electrons seeing a different electric field than the ions. But unlike the FLR effect, this effect can reduce the radial electric field. The stabilizing effect is enhanced by the spreading of the particle energies when the flux surfaces are interconnected.

The second possible stabilizing effect in a minimum-B mirror is also related to the geodesic curvature. Figure 6.3 shows magnetic flux surfaces at two axial locations. It shows that the relative position of two field lines, indicated by the triangle points, changes because the field line fanning increases with the axial distance from the midplane. Therefore the direction of the plasma pressure gradient will change relative

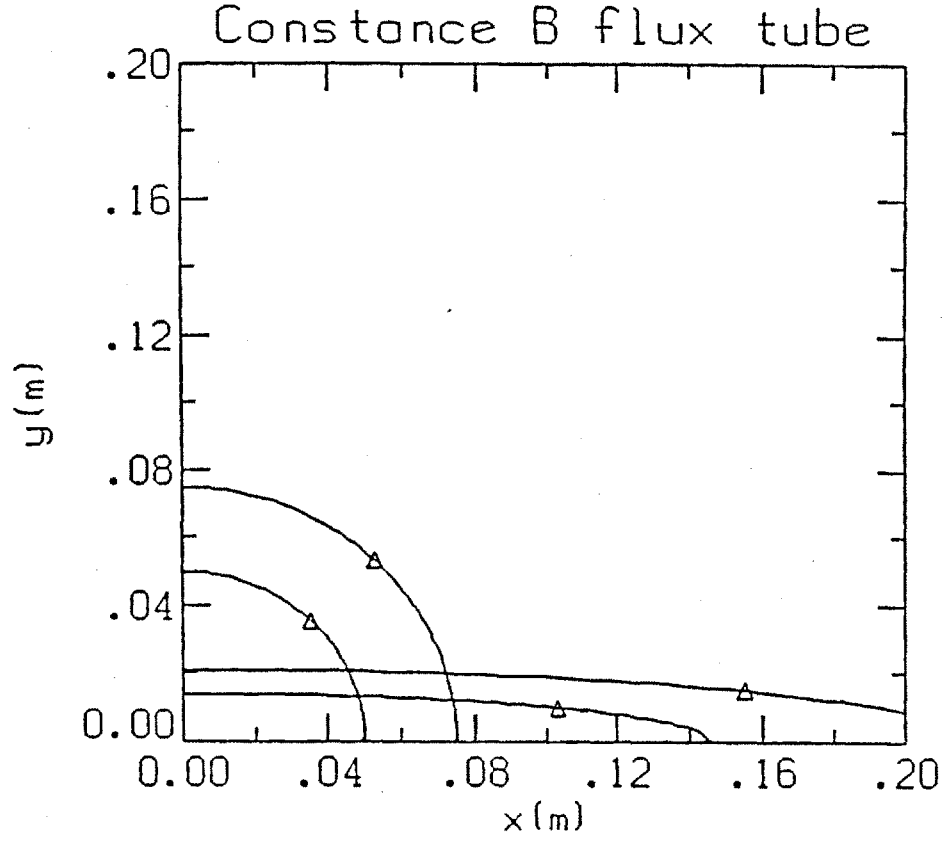

Figure 6.3: Magnetic flux surfaces at two axial locations. The triangle points indicate the intersection of field lines on the flux surfaces. The field lines change their relative positions with respect to the flux surface gradient at different axial locations because of the non-zero geodesic curvature.

to the field line curvature along a field line. Intuitively, this shift of direction will make curvature driven modes more likely to be localized in a limited axial extent. The corresponding growth rate of the instability will be lower than the interchange mode when the field line bending is involved. To confirm these geodesic curvature stabilization effects, a detailed comparison of the plasma equilibria in minimum-B machines with different field line fanning is needed. Unfortunately, data from the previous experiments are not accurate enough for such a comparison. Among the existing machines, the MHD anchor of the Tara tandem mirror is in a good position to conduct the study, where the field line fanning is smaller than Constance and the initial measurement has indicated that the plasma is likely peaked on the axis [Post, 1984; Brau, 1988].

6.4 Summary

It is clear that the hot electron plasma is more stable than the theoretical predictions from most of the theories. Cold plasma stabilization has been used to explain the plasma stability in EBT [Hiroe, 1983], Tara [Mauel, 1988], and other hot electron mirror experiments because instabilities occur after the ECRH is turned off and when the cold plasma density is reduced to certain value. However, in the Constance B minimum-B mirror, plasmas are stable in the afterglow independent of the cold electron density. This indicates that the cold electron stabilization does not play an important role in providing the plasma stability in a minimum-B field. Another commonly considered stabilizing mechanism, line-tying, also cannot explain the plasma stability in Constance.

Compressibility is an important stabilizing mechanism for the hollow plasma in minimum-B mirrors. As long as the plasma pressure is not zero near the axis, the drive for the plasma to go unstable can be reduced. Although the Constance plasma typically does not satisfy the conditions for the validity of MHD theory, the large size of this stabilizing term suggests that this effect should be included in future theories for explaining the Constance results. It also shows the importance of the three dimensional magnetic geometry to the plasma stability. This result has an effect on the current tandem mirror designs in which the line averaged curvature is calculated without the consideration of the compressibility.

There is no strong instability observed at the plasma beta at which the drift reversal is predicted to occur. At high magnetic field shots ($B_0 \geq 3.5$ kG), the mirror mode beta limit is closely approached. Further analysis is needed to determine if the plasma beta is limited by this stability condition.

There are some specific effects associated with the minimum-B magnetic field geometry. The plasma radial drift resulting from the non-zero geodesic curvature can

make different drift surfaces interconnected, thus preventing localized layer modes. The fanning of the magnetic field lines also makes instability more likely to be a ballooning mode which has a lower growth rate compared with the interchange modes.

Chapter 7

Conclusions

In this thesis, we have studied the equilibrium and stability properties of the Constance B hot electron plasma in detail. The primary results are:

(1) The ECRH generated hot electron plasma in the Constance B quadrupole minimum-B magnetic mirror is hollow. The plasma equilibrium profile is essentially determined by the plasma heating profile and the single particle drift orbit. The plasma is confined along a baseball seam curve inside the non-relativistic ECRH resonant surface and the equilibrium profile coincides with the drift orbit of deeply trapped electrons.

(2) The hollow plasma equilibrium has been observed for all the experimental conditions for which the equilibrium has been measured, ranging from $B_0 = 2.8 - 3.74$ kG, ECRH power=10 - 4000 W, and neutral gas pressure= $2 \times 10^{-7} - 5 \times 10^{-5}$ Torr. For the standard operating conditions (B_0=3 kG, ECRH power=2 kW, gas pressure=5×10^{-7} Torr, and plasma beta=0.3), the hollowness of the hot electron plasma density profile is 50 ± 10 percent, and the plasma pressure is at least as hollow as the hot electron density. The thickness of the hot electron layer is about 4 - 4.5 cm, or 6 - 7 hot electron Larmor radii.

(3) The hollow plasma equilibrium is macroscopically stable. The equilibrium exists for a time which is 5 to 6 orders of magnitude longer than the MHD growth time. Stable plasma is observed in a large physics parameter regime, ranging from T_{eh} equal

to a few keV up to 500 keV, hot electron fraction from less than 0.1 to almost 1, and plasma hollowness from 50 % to nearly 100 % (when on-axis plasmas are reduced by limiters). Low level macroscopic fluctuations do exist in the plasma. The fluctuations which are not associated with large RF emission and hot electron end loss bursts have coherent oscillation frequencies at about 3 – 4 times higher than the hot electron curvature drift frequency which is comparable to the hydrogen ion cyclotron frequency in the standard operating conditions. The fluctuation frequency increases with the vacuum magnetic field. The frequency also decreases as a function of time during the instability burst, indicating that it is either dependent on the drive of the instability or the mode is convective in radius. However, these instabilities saturate at a very low level and only cause diamagnetism fluctuations of $\delta B/\bar{B} \leq 10^{-3}$.

(4) Microinstability in the Constance B mirror is stronger than the fluid type instabilities. The diamagnetism loss during a microinstability is normally one order of magnitude higher than that during a macroinstability. The plasma profile and the beta value are more likely to be limited by the microstabilities and the RF induced diffusion.

(5) Analysis of the model equilibrium which most closely matches the experimental observation shows that magnetic gradient reversal and particle drift reversal are achieved in the experiment. There has been no evidence that the plasma becomes unstable when the plasma parameters reach the drift reversal regime. In the discharges with a vacuum magnetic field higher than 3.5 kG, the mirror mode beta limit is closely approached.

(6) Compressibility is an important effect for the stabilization of plasmas in minimum-B magnetic mirrors. In the Constance B magnetic geometry, it can stabilize a plasma of 30 percent beta with about 20 percent hollowness. This effect should be considered in the tandem mirror analysis where the plasma stability is dependent on the MHD

anchors.

(8) The combination of a set of experiments (x-ray imaging, visible light imaging, magnetic measurements and thermocouple probe measurements) has been proven useful for quantitative equilibrium determination. Plasma imaging is especially helpful because of the large amount of data contained in the 2-D images. Magnetic measurements provide crucial information about the plasma parameters such as the plasma beta and total stored energy. However, the magnetic probe measurements can only be used to determine the edge pressure profile but not the pressure at the center of the plasma. A good plasma model is also important for the equilibrium analysis. It should be constructed when the characteristics of the plasma equilibrium such as the plasma fluid and particle motion and the magnetic geometry are all taken into account.

There are a number of issues relating to the plasma equilibrium and stability in the Constance B mirror remaining to be solved. A major problem in the equilibrium analysis is that it is essentially a low beta analysis. In order to determine the equilibrium in a finite beta plasma, the self-consistent magnetic field must be used. However, the usefulness of the existing three dimensional equilibrium codes is limited by the built-in stability criteria as well as the large computational requirements for the analysis. For a hollow plasma pressure profile in a minimum-B mirror, the equilibrium codes which are based on the energy principle of the MHD equations will not converge. Thus a better understanding of the physics of plasma stability is needed. There are also remaining uncertainties in the experimental plasma equilibrium determination. One is the plasma pressure profile near the magnetic axis. In the future this can be done by conducting a detailed spatially resolved x-ray temperature measurement. Together with the measured density profile, the plasma pressure can be

obtained by taking the product of the density and the temperature profiles. Another area needed to be studied is the evolution of the plasma equilibrium at the early stages of the plasma breakdown, which has not been dealt with in this thesis.

There are more uncertainties in the plasma stability analysis. In the future stability study, several issues need to be addressed. The first is how the observed plasma stability can be theoretically understood. This has been a long-standing problem for mirror plasmas which are always more stable than the predictions from the fluid theory. The second issue is the identification of the instabilities. Experiments have to be conducted to determine the direction of the wave propagation, the wave vector and the mode structure. The background gas pressure has been observed to be an important parameter affecting the plasma stability behavior. A detailed analysis of the plasma density and temperature as functions of the gas pressure is needed to determine how the plasma stability is affected. Also, the fluctuation frequency is changing with the magnetic field and with time. Thus experiments are needed to determine if the instability is convective or if the instability frequency is related to the drive of the mode. Because the microinstabilities normally start near the magnetic axis, a detailed determination of the plasma velocity distribution as a function of radius needs to be done and the stability boundary in relation to the plasma pressure and the magnetic field gradient should be thoroughly analyzed.

Appendix A

An Analytic Approximation of the Constance B Magnetic Field

An analytical approximation of the Constance B magnetic field is derived for the equilibrium analysis. In deriving this expression, we first solve the Maxwell equations for a vacuum magnetic field and obtain the general solution in terms of multipole expansions. We then apply the solution to Constance B where the magnetic field is dominated by dipole and quadrupole fields. By matching the undetermined functions in the general solution to the fields calculated with the EFFI code and keeping the radial function to the order of r^4, we obtained an expression which is accurate to within 5 percent in the entire plasma confinement region ($\frac{B}{B_0} \leq 1.8$).

A.1 General Structure of Multipole Magnetic Field

A vacuum magnetic field can be solved in terms of an expansion series in cylindrical coordinates. We start from the Maxwell equations for a current-free magnetic field and let $\vec{B} = \nabla\chi$. Then χ satisfies the Laplace equation $\nabla^2\chi = 0$. Expanding χ into multipole components in cylindrical coordinates

$$\chi = \sum \chi_k(z,r)\cos(k\phi) \qquad\qquad k = 0, 2, 4, \ldots$$

the Laplace equation takes the form

$$(\frac{1}{r}\frac{\partial}{\partial r}r\frac{\partial}{\partial r} - \frac{k^2}{r^2} + \frac{\partial^2}{\partial z^2})\chi_k = 0. \tag{A.1}$$

Then expanding χ_k into a power series in r

$$\chi_k = \sum_{n=0}^{\infty} g_{k,n}(z)r^n,$$

Eq. (A.1) becomes

$$\sum_{n=0}^{\infty}[(n^2 - k^2)r^{n-2} + r^n\frac{\partial^2}{\partial z^2}]g_{k,n} = 0. \tag{A.2}$$

By matching the coefficients of each r^n, we have

$$g_{k,n+2} = -\frac{g''_{k,n}}{(n+2)^2 - k^2} \qquad n = k, k+2, \ldots \tag{A.3}$$

Where $g''_{k,n}$ denotes the derivative with respect to z. It is clear that there is only one free function for each multipole component, which is the first term in that series. All the later terms can be expressed in terms of the derivatives of the first term.

Now all multipole field components can be constructed. For a dipole field, the solution is

$$\chi_0 = (g_0 - \frac{1}{4}g_0''r^2) + \frac{1}{64}g_0^{(4)}r^4 - \cdots \tag{A.4}$$

For a quadrupole field, the solution is

$$\chi_2 = g_2r^2 - \frac{1}{12}g_2''r^4 + \cdots \tag{A.5}$$

Higher multipoles can be easily obtained in the same way. We have used $g_k(z)$ to denote $g_{k,k}(z)$, and $g_k^{(m)}$ to denote the m_{th} derivative of g_k.

In the so-called long-thin approximation, one keeps the first terms in each multipole component. The result is

$$\chi = g_0 - \frac{1}{4}g_0''r^2 + \sum g_k r^k \cos(k\phi) \qquad k = 2, 4, 6, \ldots \tag{A.6}$$

A.2 Constance B Magnetic Field

Constance B magnetic field is generated by a baseball magnet. It contains primarily dipole and quadrupole components. If one keeps the radial functions to the order of r^4, the magnetic field can be expressed as

$$\begin{aligned} B_x &= (-\frac{1}{2}g_0'' + 2g_2)x + \frac{1}{16}g_0^{(4)}(x^2+y^2)x - \frac{1}{3}g_2''x^3 \\ B_y &= (-\frac{1}{2}g_0'' - 2g_2)y + \frac{1}{16}g_0^{(4)}(x^2+y^2)y + \frac{1}{3}g_2''y^3 \\ B_z &= g_0' - \frac{1}{4}g_0^{(3)}r^2 + \frac{1}{64}g_0^{(5)}r^4 + g_2'(x^2-y^2) - \frac{1}{12}g_2^{(3)}(x^4-y^4). \end{aligned} \tag{A.7}$$

The mod-B surface is of the form

$$B^2 = f_0^2 + f_1(x^2+y^2) + f_2(x^2-y^2) + f_3(x^4+y^4) + f_4(x^4-y^4) + f_5x^2y^2. \tag{A.8}$$

Here, $f_0 = g_0'$ is the magnetic field on the z axis. All the f functions are functions of g's and their derivatives.

Analytical approximations of $g_0'(z)$ and $g_2(z)$ in Eq. (7) can be obtained when $\vec{B}$ has been numerically calculated. However, a large quantity of data is needed in order to accurately determine all the higher order derivatives of $g_0(z)$ and $g_2(z)$. Thus we use another approach to derive the expression. We first fit the f functions in Eq. (8) to the mod-B contours calculated with EFFI code, and then determine the direction of $\vec{B}$ from the field line trajectory. The resulting expression for the magnitude of the magnetic field can be simplified as

$$B^2 = f_0^2 + f_1[(x^2+y^2) - 2(x^4+y^4)] + f_2[(x^2-y^2) - 2(x^4-y^4)], \tag{A.9}$$

with

$$\begin{aligned} f_0 &= 1 + 0.8[1 - \cos(5z)] - 59.z^6 \\ f_1 &= 52(1+10z^2)\cos(2z) \\ f_2 &= -(120z + 1328z^3). \end{aligned}$$

Where B is normalized to be one at the center of the mirror well, and x, y, z are expressed in meters.

The trajectory of a magnetic field line satisfies

$$\frac{dx}{B_x} = \frac{dy}{B_y} = \frac{dz}{B_z}. \tag{A.10}$$

In the long-thin approximation, this equation can be easily solved if there are only dipole and quadrupole fields. The solution is

$$x = x_0 \frac{1}{\sqrt{f_0}} e^{\xi(z)} \qquad\qquad y = y_0 \frac{1}{\sqrt{f_0}} e^{-\xi(z)}, \tag{A.11}$$

where x_0 and y_0 are the field line positions on the magnetic midplane and $\xi = \int_0^z \frac{2g_2}{g_0'} dz$. The numerically generated Constance magnetic field shows that the flux lines can be very closely approximated by $x = x_0\sigma(z)$ and $y = y_0\tau(z)$, with σ and τ some functions of z. This suggests that despite the fact that r^4 terms are needed to describe the magnetic field magnitude, the long-thin approximation for the field line trajectories can still be used. By fitting the trajectory functions of Eq. (11) to the calculated trajectories, we obtain

$$x = r_0 \cos\phi \frac{1}{\sqrt{f_0}} e^{(8.15-15.6z^2)z}, \qquad y = r_0 \sin\phi \frac{1}{\sqrt{f_0}} e^{-(8.15-15.6z^2)z}, \tag{A.12}$$

where r_0 and ϕ denote the radius and the angular position of the field line at the midplane. The three components of the magnetic field can then be calculated from

$$\begin{aligned} B_x &= \frac{x'}{\sqrt{1+x'^2+y'^2}} B \\ B_y &= \frac{y'}{\sqrt{1+x'^2+y'^2}} B \\ B_z &= \frac{1}{\sqrt{1+x'^2+y'^2}} B. \end{aligned}$$

The goodness of the fitting can be evaluated by the accuracy of the fitted expression with respect to the calculated field, and the magnitude of its divergence and curl

relative to B/L, with L the scale length of the field. A numerical comparison shows that the expression is accurate to within 5 percent in the entire magnetic well, and that the divergence and the curl are typically a few percent of B/L, with $L = 40$ cm. Since there are only two independent functions g_0 and g_2 in the magnetic field expression, we can cross check the fitted expressions for f_1, f_2, f_3, f_4, f_5 and ξ by evaluating g_0 and g_2 from any two of them and then construct all the rest from g_0 and g_2. The cross check shows that the f and ξ functions are in good agreement with the reconstructed functions and the differences between them are typically below 5 percent.

Appendix B

Electronic Circuits for Magnetic Probes

In this appendix, we describe the electronic circuits for the diamagnetic loop, B-dot probe and the Hall probe system. Because the existence of the large vacuum field, the systems are required to measure signals which are 4 to 5 orders of magnitude lower than the total field. In order to achieve such accuracy, the large vacuum field needs to be accurately subtracted. In the Hall probe system, a novel digital sample-and-hold circuit is used to store the vacuum field information so that it can be subtracted during the shot. The diamagnetic loop and B-dot probe measurements are inductive measurements which have the advantage of not seeing the vacuum field when the field reaches steady state. Active electronic integrators are used to convert the pickup signals to magnetic flux.

B.1 Diamagnetic Loop and B-dot Probe

The diamagnetic loop and the B-dot probe systems consist of a pick up coil and a low drift electronic integrator, as shown in Fig. B.1. A low drift integrator is the key to an accurate inductive magnetic measurement. We modified Evans model 4130 gated electronic integrators for use in our system. The Evans 4130 integrator is a general purpose integrator containing three input channels, a gate and reset triggering circuit,

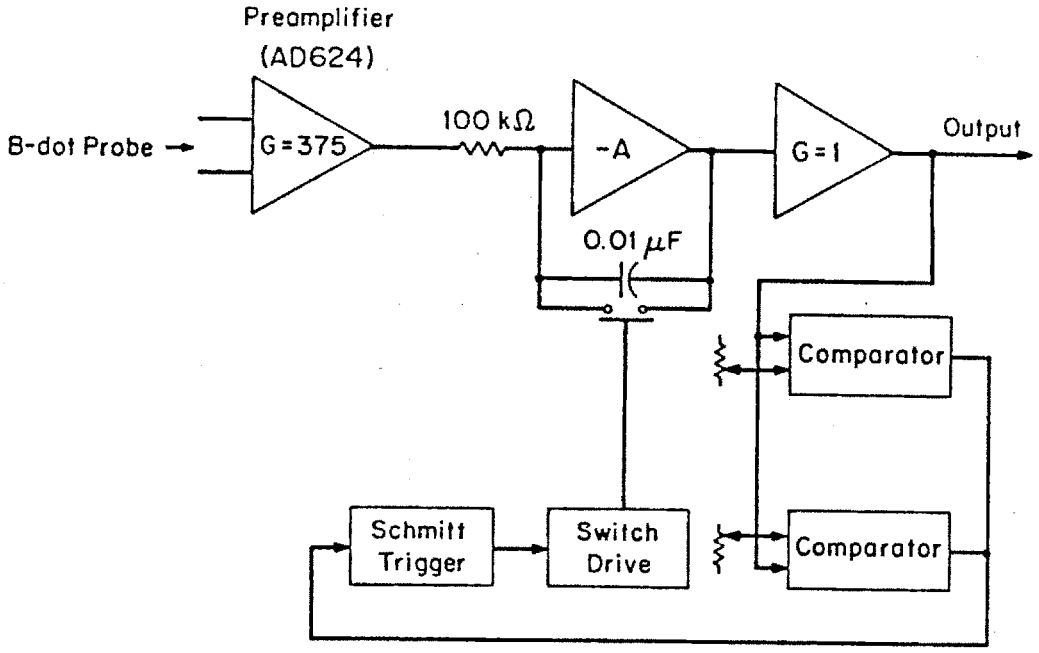

Figure B.1: Functional block diagram of the diamagnetic loop and the B-dot probe system. The integrator is modified from an Evans 4130 gated electronic integrator.

a pair of voltage comparators for automatic output reset and the main integrator. The automatic reset is controlled by the two voltage comparators which can be set between ± 6 volts, respectively. When the integrating capacitor is charged up to these limits, a triggering pulse is sent to the switch drive and discharges the capacitor within one microsecond. The integration continues after each reset and the piecewise integrated signal needs to be added together during data processing. Several modifications were made to reduce the integrator drift. We used one direct input and disconnected the other two inputs to reduce the leakage current, increased the feedback resistance R on the input channel from 10 $k\Omega$ to 100 $k\Omega$, and added a low noise preamplifier (Analog Device AD624) with gains of 375 for B-dot probes and 10 for diamagnetic loops to increase the input signal level. The values of the feedback resistor and the amplifier gain are selected to obtain the maximum signal-to-noise ratio for the system, when

the amplifier and the integrator drift noise level are taken into account. Grounding noise has been one of the main noise sources. No. 16 wires are used for preamplifier and integrator grounds which are soldered together at the power supply grounding point. The integrator drift is reduced to the order of 0.1 microvolt equivalent input noise level.

Because the pickup signal from the B-dot probe is small, shielded twisted pair cable is used to transmit the signal. The high frequency noise, which in our application occurs mainly at 360 and 60 Hz, is filtered out by a two stage low pass filter with a cut off frequency at 50 Hz at the integrator input. Since the large signal during the vacuum field ramp up charges the capacitors in the filter, this filter is kept open at the beginning of a shot. Fig. B.3 shows the B-dot probe response to a 0.1 Gauss field in a Helmholtz coil.

B.2 Hall Probe

The Hall probe system contains a Hall effect sensor and the electronic circuits for signal processing. Fig. B.2 shows a functional block diagram of the system.

A Sprague UGN-3501M Hall effect integrated circuit is used as the sensor. This monolithic sensor contains a Hall cell, differential amplifier, differential emitter output, and a voltage regulator. It can be installed inside half inch diameter tubing. The probe sensitivity is dependent on the power supply voltage and the value of an external current limiting resistor because the electric field across the Hall cell is determined by $\vec{E} = \eta \vec{J} \times \vec{B}$, with η a constant. The linearity of the sensor is primarily limited by its electronic amplifier, which has a dynamic range of approximately 3 volts. One can adjust the sensitivity according to the magnitude of the magnetic field to be measured so that maximum sensitivity is used. In our particular application where the required measurement range is 7 kG, 100 – 150 Ω current limiting resistors

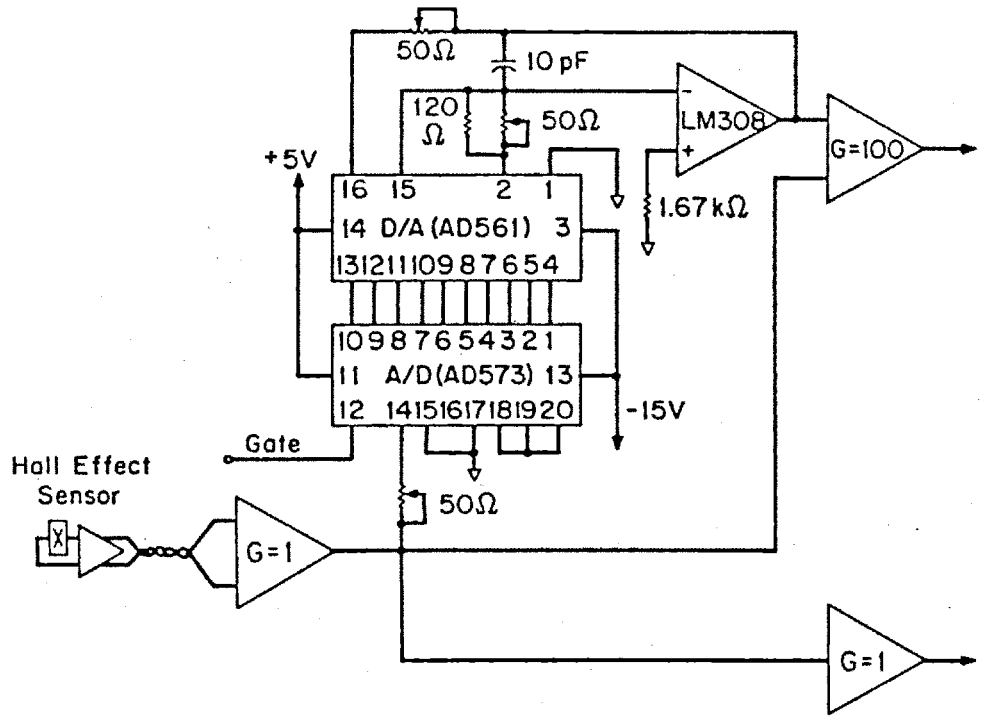

Figure B.2: Functional block diagram of the Hall probe system.

are used when the power supply voltage is 15 V. The response of each probe needs to be calibrated individually.

The heart of the signal processing electronics is a sample and hold circuit constructed with a pair of analog-to-digital and digital-to-analog convertors. It provides a stable vacuum field reference to be subtracted from the magnetic sensor during the shot so that small magnetic field changes due to plasma currents can be distinguished. This digital sample and hold is superior to an analog sample and hold in this application. In order to limit the drift rate to within 0.1 G/sec, the time constant of the sample and hold has to be at least 10^4 seconds for a circuit which holds a several kilogauss signal. Such a long RC time is very difficult to achieve with an analog circuit but poses no difficulty for a digital circuit. The A/D convertor (Analog Device AD573) and the D/A convertor (Analog Device AD561) are connected in a bipolar mode, which gives an input and output range of $\pm$ 5 Volts. The sample and hold is

controlled by an external gate on the A/D convertor. The A/D converts the input voltage to a 10 bit digital signal when triggered, and stores it until the next trigger pulse. This digital signal is read by the 10 bit D/A convertor and transformed back to an analog voltage equal to the input voltage with an accuracy of $\pm$ 10 mV. The accuracy can be improved by using 12, 14 or 16 bit convertors.

The calibration of the A/D and D/A convertors is done separately by adjusting three 50 ohm trim resistors. For the A/D calibration, the trimmer at pin 14 is set so that all the bits are turned on at input voltage of 4.985 V. For the D/A convertor, which utilizes an operational amplifier (LM308) to make current-to-voltage conversion and to provide a buffered output, the zero trimmer at pin 2 is set when the input bit is on only for pin 13, and the gain trimmer at pin 16 is set so that the output is at -5 V when all the bits are off. The noise level at the D/A convertor output is less than 0.2 millivolts, and it can be reduced to about 10 μV after filtering.

During probe operation, the magnetic field signal sensed by the Hall probe is carried differentially to the digital sample and hold input, with an offset voltage of about 4 volts. It is converted to a signal proportional to the total magnetic field by a low noise buffer amplifier. The output from this amplifier is split into three paths, one to the total field output, another to the input of the next stage differential amplifier, the third to the digital sample and hold circuit which will store the vacuum field signal. The sampling is controlled by a 1μs wide positive pulse from an external pulse generator. The conversion starts after the falling edge and takes approximately 20μs.. The differential amplifier subtracts the vacuum field from the subsequent Hall probe output and amplifies the difference by 100, providing a plasma field output with a sensitivity of about 50 mV/G.

Fig. B.3(b) shows a calibration curve for the Hall probe system in a Helmholtz coil. A 0.1 Gauss magnetic field change can be clearly distinguished by the probe.

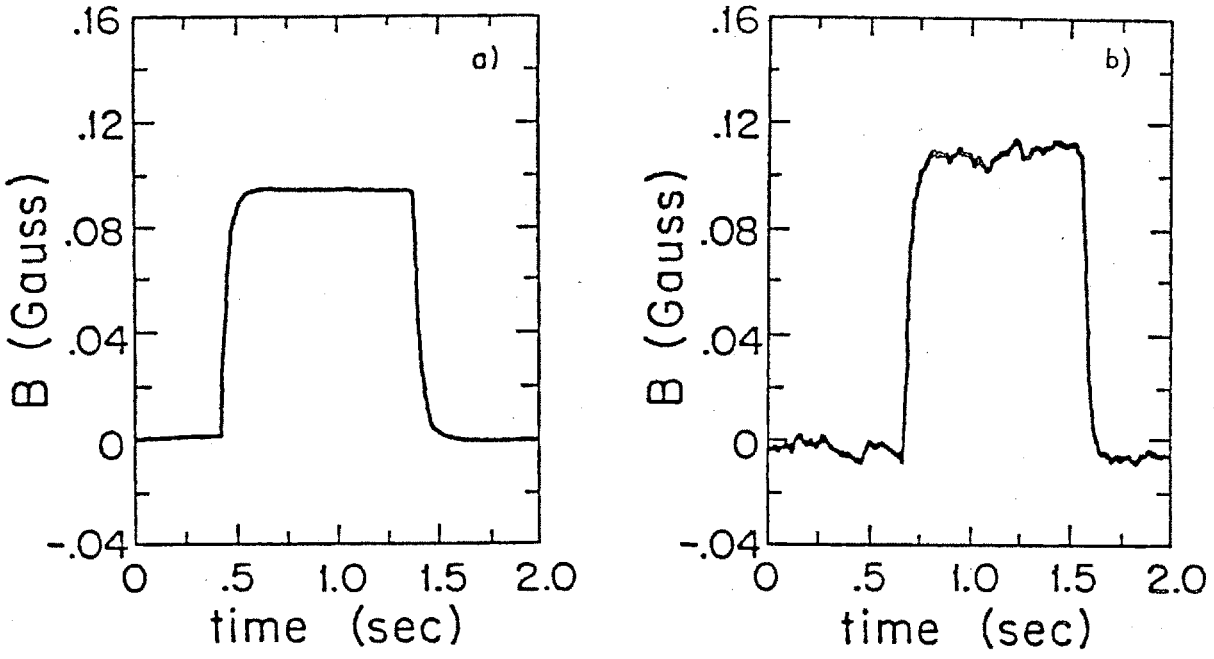

Figure B.3: Calibration of the magnetic probes in a Helmholtz coil. (a) B-dot probe. (b) Hall probe.

The noise is mostly from the Hall effect sensor used in the system.

Bibliography

[1] Anderson, D.A., (1985), Private communication.

[2] Barnett, C.F., J.A. Ray, E. Ricci, M.I. Wilker, E.W. MacDaniel, E.W. Thomas, and Gilbody, (1977), *Atomic Data for Controlled Fusion Research,* Oak Ridge National Laboratory, Oak Ridge, TN, ORNL-5207.

[3] Barr, W., and W. Perkins, (1965), *Bull. Am. Phus. Soc.* **2**, 203.

[4] Berk, H.L., (1975), *Phys. Fluids* **19**, 1255.

[5] Berk, H.L. and B.G. Lane, (1986), *Phys. Fluids* **29**, 1076.

[6] Berk, H.L., and Y.Z. Zhang, (1987), *Phys. Fluids* **30**, 1123.

[7] Biquet, A., P. Blanc, R. Gravier, P. Lecousty, H. Luc, C. Renaud, J. Tachon, D. Vern, B. Zanfagria, (1964), *CR Acad. Sci. Paris*, **259**, 1040.

[8] Bodin, H.A.B., A.A. Newton, and N.J. Peacock, (1961), *Nucl. Fusion* **1**, 139.

[9] Chen, X., (1987), M.I.T. Plasma Fusion Center Report PFC/JA-87-27, Massachusetts Institute of Technology, Cambridge, Massachusetts. Submitted to *Rev. Sci. Instrum.* .

[10] Coensgen, F.H., W.F. Cummins, W.E. Nexen, Jr., and A.E. Sherman, (1962), *Nucl. Fusion Suppl. Pt.* I, 125. et al., *Phys. Rev. Lett.* **44**,

[11] Cohen R. H., M.E. Resnick, T.A. Cutler, and A.A. Mirin, (1978), *Nuclear Fusion* **18**, 1229.

[12] Colchin, R.J., J.C. Dunlop, and H. Postma, (1970), *Phys. Fluids* **13**, 501.

[13] Dandl, R.A., A.C. England, W.B. Ard, H.O. Eason, M.C. Becker, and G.M. Hass, (1964), *Nucl. Fusion* **4**, 344.

[14] Dandl, R.A., H.O. Eason, P.H. EDMONDS, A.C. England, (1971), *Nucl. Fusion* **11**, 411.

[15] Damm, C.C., J.H. Foote, A.H. Futch, and R.F. Post, (1964), *Phys. Rev. Lett.* **13**, 469.

[16] Francis, G., J.W. Hill, D.W. Mason, 1965, *Proc. 2nd Conf. on Plasma Phys. and Contr. Nucl. Fusion Res.*, Culham Laboratory, UK, p.53.

[17] Fredian, T.W. and J.A. Stillerman, (1986), *Rev. Sci. Instrum.* **57**, 1907.

[18] Freeman, R., M. Okabayashi, G. Pacher, B. Ripin, J.A. Schmidt, J. Sinnis, S. Yoshikawa, (1971), *Plasma Physics and Controlled Fusion Research,* 1971, Madison, Wisconsin, (IAEA, Vienna, 1971), Vol. I, p.27.

[19] Garner, R.C., (1986), Ph. D. Thesis, Department of Physics, Massachusetts Institute of Technology, Cambridge, Massachusetts.

[20] Garner, R.C., M.E. Mauel, S.A. Hokin, R.S. Post, D.L. Smatlak, *Phys. Rev. Lett.* **59**, 1821 (1987).

[21] Gerver, M.J. and B.G. Lane, (1986), *Phys. Fluids* **29**, 2214.

[22] Goodman, D.L., (1988), Internal Laboratory Memorandum.

[23] Gott, Y.B., M.S. Ioffe, V.G. Telkovsky, (1961), in *Prec. Conf. on Plasma Phys. and Contr. Nucl. Fus.*, Salzburg, p. 1045.

[24] Grad, H., *Proc. Symposium in Applied Mathematics,* Vol. XVIII, Amer. Math. Soc. (1967), p. 162.

[25] Hall, L.S., and T.C. Simonen, (1974), *Phys. Fluids,* **17**, 1014.

[26] Haste, G.R. and N.H. Lazar, (1973), *Phys. Fluids* **16**, 683.

[27] Haug, E., (1975), *Z. Naturforsch.* **30 a**, 1099.

[28] Hedrick, C.L., L.W. Owen, B.H. Quon, and R.A. Dandl, (1987), *Phys. Fluids* **30**, 1860.

[29] Hiroe, S., J.B. Wilgen, F.W. Baity, L.A. Berry, R.J. Colchin, W.A. Davis, A.M. El Nadi, G.R. Haste, D.L. Hillis, D.A. Spong, T. Uckan, T.L. Owens, (1983) *Phys. Fluids* **27**, 1019.

[30] Hiroe, S., (1987), private communication.

[31] Hokin, S.A., (1987), Ph. D. Thesis, Department of Physics, Massachusetts Institute of Technology, Cambridge, Massachusetts.

[32] Ioffe, M.S., R.I. Sobolev, V.G. Tel'kovvskii and Yushmanov, (1960), *Zh. Eksperim. i Teor. Fiz.* **39**, 1602 [English transl.: *Soviet Phys.–JETP 12*, 1117 (1961)].

[33] Krall, N.A., (1965), *J. Nucl. Energy* **C7**, 283.

[34] Krall, N.A., (1966), *Phys. Fluids* **8**, 820.

[35] Kunkel, W.B., and J.U. Guillory, (1965), Lawrence Berkeley Laboratory in *Proc. 7th Int. Conf. on Phenomena in Ionized Gases*, Belgradia.

[36] Lazar, N.H., R.A. Dandl, W.F. Divergilio, B.H. Quon, and R.F. Wuerker, (1980), *Bull. Am. Phys. Soc.* **25**, 992.

[37] Lehnert, B., (1966), *Phys. Fluids* **9**, 1367.

[38] Little, E.M., W.E. Quinn, F.L. Ribe, and G.A. Sewyer, (1962), *Nucl. Fusion Suppl. Pt.* II, 497.

[39] Mauel M.E., (1985), Internal Laboratory Memorandum.

[40] Pastukhov, V.P., (1974), *Nuclear Fusion* **14**, 3.

[41] Perkins, W.A. and R.F. Post, (1963), *Phys. Fluids* **6**, 1537.

[42] Petty, C.C., (1988), Private Communication.

[43] Podgornyi, I.M., (1971), "Topics in Plasma Diagnostics", Plenum Press, New York.

[44] Post, R.F., R.E. Ellis, F.C. Ford, M.N. Rosenbluth, (1960), *Phys. Rev. Lett.* **11**, 166.

[45] Post, R.S., M. Gerver, J. Kesner, J.H. Irby, B.G. Lane, M.E. Mauel, B.D. McVey, A. Ram, E. Sevillano, D.L. Smatlak, D.K. Smith, J.D. Sullivan, J. Trulsen, A. Bers, J.W. Coleman, M.P.J. Gaudreau, R.E. Klinkowstein, R.P. Torti, X. Chen, R.C. Garner, D.L. Goodman, P. Goodrich, S.A. Hokin, *Plasma Physics and Controlled Fusion Research,* 1984, London, United Kingdom, (IAEA, Vienna, 1985), Vol. II, p.285.

[46] Quon, B.H., R.A. Dandl, W. DiVergilio, G.E. Guest, L.L. Lao, N.H. Lazar, T.K. Samec, and R.F. Wuerker, (1985), *Phys. Fluids* **28**, 1503.

[47] Rosenbluth, M.N., and C. Longmire, (1957), *Ann. Phys.* (New York), **1**, 120.

[48] Rosenbluth, M.N., N.A. Krall, N. Rostoker, (1962), *Nuc. Fus. Suppl. Part* 1, 143.

[49] Rostoker, N. and A.C. Kolb, (1961), *Phys. Rev.* **124**, 965.

[50] Sackett, S.J.,*Lawrence Livermore National Laboratory Report,* UCRL-52402 (1978).

[51] Scatt, R.F., T.H. Jensen and C.B. Wharton, (1965), *Proc. 2nd Conf. on Plasma Phys. and Contr. Nuc. Fus. Res.*, (IAEA, Vienna, Austria) Vol. I. p. 119.

[52] Smatlak, D.L., X. Chen, R.C. Garner, D.L. Goodman, and S.A. Hokin, (1986), Plasma Fusion Center Report PFC/RR-86-15, Massachusetts Institute of Technology, Cambridge, Massachusetts.

[53] Taylor, J.B., (1963) *Phys. Fluids* **6**, 215.

[54] Taylor, J.B., (1964) *Phys. Fluids* **7**, 767.

[55] Thompson, W.B., *An Introduction to Plasma Physics,* Pergamon, 1962.

[56] Turner, W. C., *et al.*, (1979) *Nulcear Fusion* **19**, 1011.

[57] Wenzel, K.W. and R.D. Petrasso, (1988) Submitted to *Rev. Sci. Instrum.*.

[58] Zhang, Y.Z., (1988) Privite communication.